An Exploration of Factors that Affect Earth's Climate in Time

Xiaojuan Liu

A dissertation
submitted in partial fulfillment of the
requirements for the degree of

Doctor of Philosophy

University of Washington

2018

Reading Committee:

David S. Battisti, Chair

Dennis L. Hartmann

Gerard H. Roe

Program Authorized to Offer Degree:
Atmospheric Sciences

University of Washington

Abstract

An Exploration of Factors that Affect Earth's Climate in Time

Xiaojuan Liu

Chair of the Supervisory Committee:
Professor David S. Battisti
Atmospheric Sciences

The Earth's climate is strongly influenced by both external and internal forcings. Several examples are the Earth's rotation rate (Ω_{E}), variations in the Earth's orbit, and the land-sea geometry. My PhD work specifically studies the impact of these three factors on the Earth's climate system.

We explore the question "what determines the meridional energy transport (MHT)?" by performing a series of rotation-rate experiments with an aquaplanet GCM coupled to a slab ocean. The change of MHT with rotation rate (Ω) falls into two regimes: in a "slow-rotating" regime ($\Omega < 1/2$ modern rotation), MHT decreases with increasing Ω; in a "fast-rotating" regime ($\Omega \geq 1/2$ modern rotation), MHT is nearly invariant. The two-regime feature of MHT is primarily related to the reduction in tropical clouds and increase in tropical temperature that are associated with the narrowing and weakening of the Hadley Cell with increasing Ω. In the slow-rotating regime, the Hadley Cell contracts and weakens as Ω is increased; the resulting warming causes a local increase in outgoing longwave radiation (OLR) which consequently decreases MHT. In the fast-rotating regime, the Hadley Cell continues to contract as Ω is increased, resulting in a decrease in tropical and subtropical clouds which increases the local absorbed shortwave radiation (ASR) by an amount that almost exactly compensates the local increases in OLR. In the fast-rotating regime, the model heat transport is approximately diffusive, with an effective eddy diffusivity that is

consistent with eddy mixing-length theory. The effective eddy diffusivity decreases with increasing Ω. However, this decrease is nearly offset by a strong increase in the meridional gradient of moist static energy and hence results in a near-constancy of MHT. Our results extend previous work on the MHT by highlighting that the spatial patterns of clouds and the factors that influence them are leading controls on MHT.

In Chapter 2, we examined two factors that contribute to the early Eocene climate of tropical South America: a narrower Atlantic ocean and enhanced CO_2. For this study, We used two atmospheric general circulation models (ECHAM 4.6 and CAM5) coupled to a slab ocean. Experiments show that, to first order, narrowing the Atlantic decreases the precipitation of tropical South America, whereas increasing atmospheric CO_2 tends to increase the precipitation. The early Eocene climate in our model is a near-linear contribution of change in atmospheric CO_2 concentration and change in Atlantic geometry, with a dominant contribution from the latter, resulting in a drier-than-today tropical South America during the early Eocene. Using water budget analysis, we find that the precipitation reduction induced by narrowing the Atlantic is mainly due to the reduction of water vapor flux entering South America across the northeast and east boundaries which, in turn, is due to a reduction in the amount of water evaporated from the ocean as air travels from Africa to the South American continent. It is not due to changes in atmospheric circulation. In fact, there is no dramatic atmospheric circulation change around South America even though the Atlantic Ocean is shrunk to less than half its modern width. Our study provides a step towards a dynamical understanding of how the Eocene climate of South America differs from today's.

Summertime insolation was more intense in the Northern Hemisphere during the mid-Holocene, resulting in enhanced monsoonal precipitation. In Chapter 3, we examine the changes in the annual mean tropical precipitation, as well as changes in atmospheric circulation and upper ocean circulation in the mid-Holocene compared to the pre-industrial climate, as simulated by 12 coupled climate models from PMIP3. In addition to the pre-

dominant zonally-asymmetric changes in tropical precipitation, there is a small northward shift in the location of intense zonal mean precipitation (mean ITCZ) in the mid-Holocene in the majority (9 out of 12) of the coupled climate models. In contrast, the shift is southward in simulations using an atmospheric model coupled to a slab ocean. The northward mean ITCZ shift in the coupled simulations is due to enhanced northward ocean heat transport across the equator (OHT(EQ)) which demands a compensating southward atmospheric energy transport across the equator, accomplished by shifting the Hadley cell and hence move the zonal mean ITCZ northward. The increased northward OHT(EQ) is primarily accomplished by changes in the gyre circulation in the upper-ocean in the tropical Pacific acting on the zonally asymmetric climatological temperature distribution. The gyre intensification results from the intensification of the monsoonal winds in the Northern Hemisphere and the weakening of the winds in the Southern Hemisphere, both of which are forced directly by the insolation changes.

TABLE OF CONTENTS

Page

List of Figures iii

List of Tables ix

Glossary xi

Chapter 1: Introduction 1

Chapter 2: The Effect of Cloud Cover on the Meridional Heat Transport: Lessons from Variable Rotation Experiments 3

2.1 Introduction 3

2.2 Experiments and Methods 5

2.3 Results 5

2.4 Understanding Changes in MHT in terms of Radiation 9

2.5 The Connection with Dynamics 20

2.6 Discussion 23

2.7 Summary 26

Chapter 3: South American climate during the early Eocene: impact of a narrower Atlantic and higher atmospheric CO_2 29

3.1 Introduction 29

3.2 Model and Experimental Design 31

3.3 Results 33

3.4 Discussion 48

3.5 Conclusion 50

Chapter 4: Tropical Precipitation and Cross-Equatorial Ocean Heat Transport during the Mid-Holocene 53

4.1 Introduction 53
4.2 Data and Methods 56
4.3 Results 59
4.4 A Mechanistic Model of the change in mean ITCZ and in the cross-equatorial ocean heat transport 70
4.5 Conclusion and Discussion 71

Chapter 5: Concluding Remarks 78

Appendix A: Appendix Figures for Chapter 4 80

Bibliography 87

LIST OF FIGURES

Figure Number Page

2.1 (a) Surface temperature, in degree Celcius, for various values of $\mathbf{\Omega}$. Note the displacement of latitude is area-weighted; hence, distance along the abscissa is linearly proportional to area covered. (b) same as (a), but for surface moist static energy (units: J kg^{-1}). 6

2.2 Cloud fraction (shading) overlayed with meridional streamfunction (contours) for each experiment; contours start from $\pm 20 \times 10^9 kg\ s^{-1}$, with intervals of $20 \times 10^9 kg\ s^{-1}$ for all experiments except for $\mathbf{\Omega} = 1/16$ (contours start from $\pm 40 \times 10^9 kg\ s^{-1}$ and with intervals $\pm 40 \times 10^9 kg\ s^{-1}$). Note the displacement of latitude is area-weighted. The latitude range in the right panels is 0 to 40° because in the fast-rotating regime ($\mathbf{\Omega} \geq 1/2$) clouds in the high latitudes are saturated and so changes do not affect the energy balance (see Figs. 8b,d). 7

2.3 The eddy momentum transport measured by the zonal and temporal mean of $u'v'$ at 300mb, where u' and v' are the deviation of the zonal wind and meridional wind from their time and zonal mean, respectively ($m^2\ s^{-2}$) for various values of $\mathbf{\Omega}$. The dot on each line that is of the same color as the line it resides on denotes the poleward edge of the Hadley Cell, i.e. the width of the Hadley Cell. Note the displacement of latitude is area-weighted. 9

2.4 (a) The total meridional energy transport, in PW, for various values of $\mathbf{\Omega}$. Note the displacement of latitude is area-weighted. (b) and (c) are the peak value of the meridional energy transport and the transport averaged between 20-60°, respectively. The uncertainty in $\mathrm{MHT_{max}}$ is typically +/- 0.2 PW. Blue stars are for the experiments without Q-flux. 11

2.5 Graphical illustration of the calculation of (a) the maximum meridional heat transport ($\mathrm{MHT_{max}}$), (b) $\mathrm{ASR^*}$ and (c) $\mathrm{OLR^*}$. For each variable, i.e. $\mathrm{MHT_{max}}$, $\mathrm{ASR^*}$ and $\mathrm{OLR^*}$, and for each hemisphere, the surplus in the tropics relative to the global mean is shaded orange, while the deficit in the extratropics relative to the global mean is shaded blue. Reproduced from Donohoe and Battisti (2012) with permission. 13

2.6 $\mathrm{ASR^*}$ (a; positive downward) and $\mathrm{OLR^*}$ (b; positive upward), in PW, for each experiment. (c) is the difference between (a) and (b). 15

2.7 Clear-sky ASR*, ASR$^*_{\rm clr}$ (a) and clear-sky OLR*, OLR$^*_{\rm clr}$ (b), in PW, for each experiment. (c) and (d) are the same as (a) and (b), but for ASR$^*_{\rm cld}$ and OLR$^*_{\rm cld}$, which are defined as $ASR^* - ASR^*_{clr}$ and $OLR^* - OLR^*_{clr}$, respectively. 16

2.8 The clear-sky ASR, ASR$_{\rm clr}$ (a) and impact of clouds on ASR, ASR$_{\rm cld}$ (b), in $W\ m^{-2}$, for experiments in the fast-rotating regime. Note the displacement of latitude is area-weighted. (c) and (d) are the same as (a) and (b), but for OLR. The gray dashed lines indicate location of the nodal point of $\mathbf{\Omega} = 1$. Note the different y-axes in each panel. The results illustrate that the biggest changes are equatorward of the nodal point. 18

2.9 Same as Fig. 2.8, but for experiments in the slow-rotating regime. 19

2.10 (a) Eddy length scale (L) and (b) Eddy velocity scale (V) area-averaged between 30° to 60° for various values of $\mathbf{\Omega}$. (c) scatter plot of effective eddy diffusivity D$_{\rm eff}$ (see Eqn. 2.10 for definition) versus VL averaged between 30° to 60° for the whole ensemble of experiments. 22

3.1 The seasonal and annual mean climatological precipitation (shading; mm/day) and 925-hPa winds (vectors; m/s) for (left) observation and (right) from the modern-day simulation using ECHAM4.6 coupled to a slab ocean. Observed precipitation data are from monthly Climate Prediction Center (CPC) Merged Analysis of Precipitation (CMAP; Xie and Arkin 1997) from January 1979 to December 2010, available online at `http://www.esrl.noaa.gov/psd/data/gridded/data.cmap.html`. Observed 850-mb winds are from NCEP2 covering the same period. 34

3.2 The difference in seasonal precipitation (units: mm day^{-1}) due to enhanced CO_2 and a narrower Atlantic (Narrow_1000CO2) compared to that with modern-day geometry and 353 ppm CO_2 (Wide_353CO2). The lower right panel shows the percent change of annual-mean precipitation ((Narrow_1000CO2/Wide_353CO2) - 1) *100). Red boxes represent the regions over which domain averages are examined in Fig. 3. 36

3.3 The difference in seasonal surface temperature (units: K) due to enhanced CO_2 and a narrower Atlantic (Narrow_1000CO2) compared to that with modern-day geometry and 353 ppm CO_2 (Wide_353CO2). 37

3.4 Seasonal cycle of precipitation (units: mm day^{-1}) area-averaged over the box regions indicated in Fig. 3.2: observations (black line), from the modern-day simulation today (Wide_353CO2, blue line), and from the early Eocene simulation (Narrow_1000CO2, red line). 39

3.5 Changes in precipitation (units: mm day^{-1}) during DJF. (a) early Eocene minus today (repeated from Fig. 3.2), (b) The impact of geometry at 1000 ppm CO_2 concentration (i.e. Narrow_1000CO2 minus Wide_1000CO2), (c) impact of geometry at 353 ppm (i.e. Narrow_353CO2 minus Wide_353CO2), (d) impact of CO_2 concentration at modern Atlantic geometry (i.e. Wide_1000CO2 minus Wide_353CO2), and (e) impact of CO_2 concentration at narrow Atlantic geometry (i.e. Narrow_1000CO2 minus Narrow_353CO2). 41

3.6 Water budget in the Wide_1000CO2 (gray) and the Narrow_1000CO2 (red) experiments. (a) Precipitation, evaporation, and precipitation minus evaporation, all area-averaged over the entire South American continent. All quantities are converted to be in the units of mm day^{-1}. Convergence of water flux is calculated as the sum of water flux into South America across all boundaries shown in panel (b). (b) Vertically integrated water vapor flux into South America across each boundary (units: kg m^{-2} s^{-1}) as a function of latitude (see text). (c) Total water flux into South America across each boundary, converted to be in the units of mm day^{-1} by dividing the sum by the area of South America. 43

3.7 Integral of evaporation (units: kg m^{-2}) along the trajectory of climatological DJF 925-hPa winds for (a) the Wide_1000CO2 experiment and (b) Narrow_1000CO2 experiment. Trajectories are terminated when they reach South America. 46

3.8 As in Fig. 3.5, but for SON. 47

3.9 Precipitation (shading; mm/day) during SON from (a) "Wide_1000CO2" experiment and (b) "Narrow_1000CO2" experiment. c and d are the same as a and b, respectively, but for vertical velocity at 500-hPa (shading; Pa/s). . . . 49

3.10 Differences of precipitation (units: mm day^{-1}) in the "early Eocene" due to draconian change in "ocean circulation"; that is, Narrow_1000CO2 minus Narrow_1000CO2 with Q-flux = 0. Changes over ocean are not shown. 51

4.1 (a) The multi-model mean of climatological annual-mean precipitation in the pre-industrial experiment (contours; mm day^{-1}), and of the change in precipitation (mid-Holocene minus pre-industrial) from the PMIP3 models (shaded; mm day^{-1}). All of the PMIP3 climate models include dynamic oceans. (b) Same as (a), except for ECHAM4.6-slab ocean model. (c) Zonal-mean annual-mean climatological precipitation (solid lines; mm day^{-1}) and change in precipitation (dashed lines; mm day^{-1}) from the PMIP3 models (red) and from the ECHAM4.6-slab ocean model (blue). 61

4.2 (a) Scatterplot of the change (mid-Holocene minus pre-industrial) in the latitude of the precipitation centroid versus the change in cross-equatorial atmospheric energy transport (ΔAHT(EQ); PW). The solid line is the least squares fit, 3° latitude/PW. (b) The change in the hemispheric difference in the net hemispherically integrated energy flux into the atmosphere (colored bars) at the top of the atmmosphere ($\frac{1}{2}[F_{TOA}]\Big|_{SH}^{NH}$, left) and at the surface ($\frac{1}{2}[F_{SFC}]\Big|_{SH}^{NH}$, right). For each model, the hatched bar represents the hemispheric difference in the net energy into the atmosphere; that is, the hatch bar is $-\Delta$AHT(EQ), which is the sum of the two colored bars for each model (see Eq. (4.5)). Note that at equilibrium, the change in the net surface flux in the ECHAM4.6-slab ocean model is zero. The coloring in (b) follows the key in panel (a). 63

4.3 Change in the cross-equatorial ocean heat transport (ΔOHT(EQ); PW) between the mid-Holocene and the pre-industrial for (a) the sum of the ocean basins, (b) the Atlantic basin only, and (c) the Indo-Pacific basins only. The green bars in panels (a - c) represent the results derived from the hemispheric asymmetry in the change in surface energy flux, $\Delta\mathrm{OHT(EQ)} = -\Delta\frac{1}{2}[\mathrm{F_{SFC}}]\Big|_{\mathrm{SH}}^{\mathrm{NH}}$, and blue bars denote results obtain directly from the ocean model output (Eq. (4.6)). Panels (e) and (f) are the changes in OHT(EQ) associated with changes in the ocean temperature only and changes in the ocean circulation only, respectively (see Eq. (4.7)); panels (e) and (f) sum to the results shown in panel (d). The dynamic contribution shown in (f) is further broken into contributions associated with (g) the change in overturning circulation and (h) the change in gyre circulation (see Eq. (4.8)). (i) shows the changes in the dynamic contributions that are due to the changes in the seasonal cycle. . . 66

4.4 Change in the annual-mean surface wind stress over the oceans (vectors; Pa) and its curl (shading; 10^{-8} N m^{-3}), mid-Holocene minus pre-industrial. Shown in (a), (b) and (c) are the June-July-August mean change, December-January-February mean change and annual mean change from the multi-model mean of the PMIP3 models, respectively. (d) Same as (c), except for from the ECHAM4.6-slab ocean model. Note the color bar of panel d is different from the others. 69

4.5 Processes controlling how insolation differences between the mid-Holocene and present day change ITCZ and AHT(EQ) differently in an atmosphere-dynamic ocean model (left) versus an atmosphere-slab ocean model (right). Insolation differences first drive zonally and seasonally asymmetric anomalies in atmospheric circulation and hence in the surface wind stress. In the slab ocean, the changes in wind stress don't impact the ocean circulation or the heat transport. In the dynamic ocean, however, the changes in wind stress over the Indo-Pacific oceans drive zonally asymmetric change in ocean circulation, which, acting on the zonally asymmetric climatological temperature, induces a zonally-averaged anomalous northward ocean heat transport across the equator and results in anomalous heating of the Northern Hemisphere (cooling of the Southern Hemisphere). To maintain equilibrium, the atmosphere moves anomalous heat from the Northern Hemisphere to the Southern Hemisphere by shifting the Hadley Cell and the attendant mean ITCZ northward. . . . 72

4.6 (a) Change (mid-Holocene minus pre-industrial) in the annual-mean surface wind stress over the oceans (vectors; Pa) and precipitation (shading; mm day^{-1}) after removal of the zonal mean value of each latitude. Shown in (a) is the multi-model mean from the PMIP3 models. Panel (b) shows the zonal mean change in surface zonal wind stress (blue) and in precipitation (red) which, when removed from Figs. 1a and 4c, create the figure shown in panel (a). Panels (c) and (d) are the same as panels (a) and (b), but for the ECHAM4.6-slab ocean model. The arrow in (b) and (d) is the reference wind stress vector used in (a) and (c). 74

4.7 Scatter plots of changes in precipitation centroid vs. ΔAHT(EQ). Averages are shown over (a) the Atlantic Basin, (b) the Pacific Basin, (c) the Indian Basin, and (d) all land. The color code in panels (a)-(d) is the same as the one used in Fig. 4.2. The results in panels (a)-(d) are re-plotted in panel (e) with the precipitation centroid scaled by the fraction of the latitude circle occupied by the respective basin. Black unfilled circles in each panel represent the changes in the zonal mean precipitation centroid vs. ΔAHT(EQ), i.e. the same as the colored dots in Fig. 4.2a. 77

A.1 OHT(EQ) of the pre-industrial simulation (upper) and the difference in OHT(EQ) between pre-industrial and mid-Holocene (ΔOHT(EQ); lower), calculated using three methods. In the figure, "exact" denotes OHT(EQ) calculated by the model and outputed during the simulation (the "exact" answer); and surface flux method refers to OHT(EQ) derived from the hemispheric asymmetry in the change in surface energy flux, $\Delta\text{OHT(EQ)}) = -\Delta\frac{1}{2}[\text{F}_{\text{SFC}}]\Big|_{\text{SH}}^{\text{NH}}$; and direct method refers to the calculation of OHT(EQ) from ocean current and temperature output from the model. 81

A.2 The climatological annual-mean precipitation in the pre-industrial experiment (solid line; units: mm/day) and the change in annual-mean precipitation (mid-Holocene minus pre-industrial; dashed line; units: mm/day) for each PMIP3 model. 82

A.3 Changes (mid-Holocene minus pre-industrial) in the annual mean surface wind stress (vectors; Pa) and wind stress curl (shading; 10^{-8} N m^{-3}) for each PMIP3 model. 83

A.4 Fig. A.3 continued. 84

A.5 Fig. A.3 continued. 85

A.6 (a) Change (mid-Holocene minus pre-industrial) in the annual-mean surface wind stress over the oceans (vectors; Pa) and precipitation (shading; mm day^{-1}) after removal of the zonal mean value of each latitude. Shown in (a) is the multi-model mean from the PMIP3 models. Panel (b) shows the zonal mean change in surface zonal wind stress (blue) and in precipitation (red) which, when removed from Figs. 1a and 4c, create the figure shown in panel (a). Panels (c) and (d) are the same as panels (a) and (b), but for the ECHAM4.6-slab ocean model. The arrow in (b) and (d) is the reference wind stress vector used in (a) and (c). 86

LIST OF TABLES

Table Number Page

2.1 The Hadley Cell strength versus the mean divergence of the eddy momentum flux. In the table below, width of the Hadley Cell (L_H) is determined as the first latitude poleward of the maximum absolute value of the Hadley Cell streamfunction at which the mass flux streamfunction at the sigma level of its extremum above sigma = 0.7 is 10% of its extremal value, following Walker and Schneider (2006). The Hadley Cell strength is defined as the maximum absolute value of the mass flux streamfunction. The mean divergence of the eddy momentum flux (column four) is the meridional average of the divergence of eddy momentum flux from the equator to L_H, that is, $\frac{\int_0^{L_H} \frac{d(\overline{u'v'})}{d\theta} cos\theta d\theta}{\int_0^{L_H} cos\theta d\theta}$, where $\overline{u'v'}$ is the eddy momentum flux and θ is latitude. Eddy efficiency is defined as the mean divergence of the eddy momentum flux divided by the strength of the Hadley Cell. 10

2.2 Decomposition of atmospheric heat transport (AHT) into the contribution by mean meridional circulation (MMC) and the contribution by eddies. The contribution by MMC is calculated as $\int_{-\pi/2}^{0} \int_0^{2\pi} (\int_{p_s}^{0} [v][h] dp) cos\theta d\lambda d\theta$, where v is the meridional wind, h is the moist static energy, p is pressure, p_s is surface pressure, θ is latitude, λ is longitude and $[\cdot]$ denotes zonal and temporal mean. The eddy energy transport is defined as the residual of the MMC transport from the total AHT estimated as $\int_{-\pi/2}^{0} \int_0^{2\pi} (\int_{p_s}^{0} (vhdp) cos\theta d\lambda d\theta$. In the calculation of total AHT, the vertical integral of vh is calculated at the model grid at each time step. In the table below, lat_{max} denotes the latitude where AHT calculated from the meridional integral of the net heat flux into the atmosphere reaches its maximum value. 12

3.1 Experiments performed in this study. 32

3.2 Precipitation or change in precipitation area-averaged over South American continent; units: mm day^{-1}. 38

3.3 Changes in DJF precipitation, evaporation, precipitation minus evaporation, and water vapor flux between Narrow_1000CO2 and Wide_1000CO2. All quantities are area-averaged over South America; units: mm day^{-1}. 42

4.1 List of the model names, resolutions and references for the PMIP3 models used in this study. Also shown is the length of the pre-industrial (PI) and the mid-Holocene (6ka) simulations. When there was an ensemble of runs for an experiment, climatologies were calculated using the first ensemble member. . 57

GLOSSARY

MHT: Meridional Heat Transport

ASR: Absorbed Shortwave Radiation

OLR: Outgoing Longwave Radiation

OHT(EQ): cross-equatorial Ocean Heat Transport

PMIP3: the phase 3 of the Paleoclimate Modeling Intercomparison Project

ITCZ: Intertropical Convergence Zone

CESM: Community Earth System Model

ECHAM: an atmospheric general circulation model developed at the Max Planck Institute for Meteorology

MID-HOLOCENE: a period of roughly 6000 years ago

EARLY-EOCENE: a period of roughly 55 million years ago

ACKNOWLEDGMENTS

Through my seven-year study in Seattle, there are so many people to thank. My first and utmost gratitude goes to my advisor, David Battisti, for his guidance and support over the years. It is David that helped me grow from a research novice to an independent scientist. He taught me not to follow blindly but to give my genuine thinking when picking up a question. He taught me to be rigorous at my research, to think beyond the question, and to have a big-picture view. I feel so fortunate and privileged that I had the opportunity to work with him all these years. Looking backward, I'm particularly thankful that he gave me enough space to learn and grow up in my own pace but also set a high bar on what I should achieve. This has allowed me to maintain a good work-life balance while also produce high-quality science. Other than being an awesome advisor, David is also an important person in my life. I'd like to thank for him being involved in the most important moments of my life. He walked me down the aisle and gave me away at my wedding, and held the baby shower for me at their house. He and Lynn showed their love and support for me having a family here in Seattle and gave me a lot of help whenever I'm in need. I'm extremely grateful for that.

I'd also like to thank my Ph.D. committee – Dargan Frierson, Dennis Hartmann, Gerard Roe, and Eric Steig for all their help and guidance. Dargan taught me the energy budget analysis method. He also gave me many constructive advice at various stages of my research. Gerard taught me the energy diffusion model and gave me a lot of helpful insights on how to write a scientific paper. I'm also always amazed by his British colloquia and humor. I joined the lunch club with Dennis for the past

three years and therefore had the advantage to bug him with all kinds of scientific and nonscientific questions, even question like “whether my baby should go to childcare”. I also want to thank him for teaching me to “always have a small child reside in your heart”. I took the paleoclimate class from Eric. His passion and love at what he is doing is very contagious and inspired me to be a scientist like him.

I’m very fortunate to have been surrounded by so many talented and distinguished scientists through my study at University of Washington. I greatly benefited from interacting with them. I would like to express my gratitudes especially towards Chris Bretherton, Mike Wallace, Abby Swann, Cecilia Bitz, and Robert Wood. I’d like to thank them for their availability and willingness to help when I was writing proposals for postdoc fellowships or running into scientific questions. In addition, I want to give my thanks to all the staff of the Department of Atmospheric Sciences, especially Erica Coleman and Marc Michelsen. They are both so trustworthy and able to solve my problems whenever and wherever they are.

I also greatly benefited from interactions with my fellow graduate students. Whenever I have a question or in need of help, I will get timely help just by sending an email to the grads email list. They also taught me Python and the sense of fighting for our own rights. I’m inspired by them and honored to be part of them. My special thanks go to Elizabeth Maroon, Paulo Ceppi, Xiaoming Shi, Yen-ting Hwang, and Jack Scheff who have been giving me tremendous help and advice on my research and career planning through my graduate study and even now. My thanks also go to the past and present members of the Battisti group – Andy Rhines, Michelle Tigchelaar, Fiona Lo, Yue Dong, Lucas Zeppetello, Robert Wills, Aaron Donohoe and Rachel White. When I first met with David, he said that he didn’t have a group meeting. I didn’t expect that there would be weekly group meetings in the last year of my graduate school. But it is just so helpful and awesome! I would like to give my special

thanks to Aaron and Rachel. I worked with each of them for one project. They are always being available and willing to help. They read my manuscripts carefully, gave constructive comments, and answered my questions in a timely way! I'm inspired by their hard-working and willingness to help.

I would like to thank my dear friends in Seattle. Through my seven years in Seattle, I had so many times of joyful hiking, camping, backpacking, chatting, and dinner gathering with them. My life would have been so dull without them. My special thanks goes to Cheng Dang, Yongfei Zhang, Wenwen Kong, Qianjie Chen, Jiayue Huang, Wei Zhao, Crystal McClure, Viral Shao, Judy Twedt, Marysa Laguë, Isabel McCoy, Daniel McCoy, and Casey Wall. They have been constantly and considerably helping me and supporting me through time!

I am incredibly thankful to my family for their encouragement, support and help. I'd like to thank my parents for allowing me go abroad to pursue my interest in atmospheric sciences and to see something different, and thank my brother for taking good care of my parents when I'm far away so that I can focus on my study. My special thanks goes to my mom and parents-in-law who have been staying far away from home to help take care of my daughter. I'm really grateful for that.

Finally, I want to thank my dear husband, Guozheng, and my adorable daughter, Eleanor. Thank you two for bringing endless happiness and joy to my life, for always believing in my abilities and supporting whatever decision I made, and for giving me your full love. I love you two!

DEDICATION

to my parents, Xiuyi Liu and Zhaomei Wang

Chapter 1

INTRODUCTION

This Earth's climate is strongly influenced by both external and internal forcings. For example, variations in the Earth's orbit modulates the insolation received by the Earth, shuffling the Earth between a warm globe and a frozen world. The rise of atmospheric CO_2 since pre-industrial has increased the global mean surface temperature by almost 1°C. Studying the response of climate system to different forcings will therefore help us identify the factors that are dominating the climate of the Earth. It will also help understand the climate change happened in the past that are caused by one or more of these factors. By putting the current global warming in a historical context, this study will also help us know the resilience of the climate system and the potential risks of the current increase in atmospheric CO_2.

Changes in the Earth's rotation rate, variations in the Earth's orbit, and changes in the land-sea geometry are known to have important impacts on the climate. The Earth's rotation rate determines the atmospheric circulation and hence the spatial pattern of clouds; the latter plays an important role in determining the planetary radiation balance and hence the mean planetary climate (Yang et al., 2014). Variation in the Earth's orbit changes the meridional and seasonal distribution of insolation received by the Earth, and hence the Earth's climate. Land-sea distribution plays an important role in shaping the atmospheric circulation and oceanic circulation that are crucial for the energy transport. For example, both modeling studies and proxy records suggest that opening of the Drake passage gave birth to an Atlantic meridional overturning circulation that warmed the Northern Hemisphere and cooled the Southern Hemisphere (Toggweiler and Samuels, 1995; Toggweiler and Bjornsson, 2000; Sijp and England, 2004).

This thesis explores the impacts of the above astronomical and geological forcings on the

Earth's climate. Specifically, we address the following main questions:

1. **The effect of the Earth's rotation rate on the meridional energy transport;**
2. **The impact of CO_2 and Atlantic geometry on the climate of tropical South America;** and
3. **Effect of the precession of the Earth's rotational axis on tropical rainfall;**

These three questions are investigated in chapters 2-4. Chapter 2 investigates the impact of the Earth's rotation rate on the poleward energy transport, extending previous work by highlighting the leading roles of spatial patterns of clouds. In chapter 3, we explores the effect of Atlantic geometry and increasing the atmospheric CO_2 concentration on the climate of South America, as well as their implication for the climate of the early-Eocene. Chapter 4 studies the impact of the precessional cycle on tropical precipitation and cross-equatorial energy transport during the mid-Holocene, with an emphasis on the role that ocean heat transport plays in shifting the tropical precipitation band.

The work described in Chapters 2 and 4 is published in the Journal of Climate (Liu et al., 2017a,b).

Chapter 2

THE EFFECT OF CLOUD COVER ON THE MERIDIONAL HEAT TRANSPORT: LESSONS FROM VARIABLE ROTATION EXPERIMENTS

2.1 Introduction

The atmosphere-ocean system transports energy poleward, balancing the energy surplus in the tropics with the deficit in the extratropics. In the modern climate, the net annual-mean meridional heat transport (MHT) peaks at 35° in both hemispheres, with atmospheric transport contributing about 80% in the Northern Hemisphere and about 90% in the Southern Hemisphere (Trenberth and Caron, 2001; Fasullo and Trenberth, 2008). Numerical modeling studies show that the MHT tends to stay remarkably invariant even for very different climates, including for LGM boundary conditions, modern boundary conditions with quadrupled CO_2 (Manabe and Bryan, 1985; Donohoe and Battisti, 2012), and for very different ocean heat transport (Magnusdottir and Saravanan, 1999; Rose and Ferreira, 2012). In this paper, we explore the question "what determines the meridional heat transport?"

Based on the one-dimensional energy-balance equation, Stone (1978) argued that the magnitude of the annual mean total MHT is insensitive to the details of dynamics of the atmosphere-ocean system, and this insensitivity is due to: (1) the high efficiency of the dynamical transport mechanisms; (2) the negative correlation between the local planetary albedo and the outgoing radiation to space in the extratropics; and (3) a robust structure in the large-scale meridional profiles of absorbed shortwave radiation (ASR) and outgoing longwave radiation (OLR). As a caveat, Stone also noted that "the precise cancellation of the structure terms may not hold if the structure and dynamics of the atmosphere-ocean system change from those of current state."

One obvious way to test Stone's argument and explore the mechanisms that control MHT is to perform numerical experiments that alter the atmospheric dynamics, while keeping the overall geometry fixed. A straightforward way to achieve this is by altering the Earth's rotation rate. Williams (1988) performed some early simulations with different rotation rates, but did not focus on MHT. Vallis and Farneti (2009) studied the change of MHT with the Earth's rotation rate and found that MHT decreases with increasing rotation rate. However, the study used a gray atmosphere (i.e., no clouds and constant longwave emissivity; Frierson et al., 2006), and therefore omits the potentially important impact that cloud changes might have on the global energy budget (e.g., Trenberth et al., 2009).

In this paper, we explore the question "what determines the meridional heat transport?" by modifying the Earth's rotation rate, and allowing for the concomitant change in clouds and water vapor distribution that we hypothesize are fundamental to determining MHT. This is done by performing experiments with an aquaplanet atmospheric General Circulation model coupled to a slab ocean, changing the planet's rotation rate (Ω) between one-sixteenth and four times the present-day value. We find that in this range of rotation rates, and for our model, the change of MHT with rotation rate falls into two regimes: a slow-rotating regime, in which MHT decreases with increasing rotation; and a fast-rotating regime, in which MHT stays relatively invariant. But to a large extent, MHT stays relatively constant with increasing rotation: the maximum change is about 30% of the ensemble mean MHT. The constancy of MHT in the fast-rotating regime is not a result of a constancy in ASR or OLR with rotation rate, as assumed by Stone; on the contrary, there are large changes in the meridional structure of both ASR and OLR; however, the changes almost completely offset each other, so MHT remains approximately constant. The top-of-atmosphere radiation patterns are associated with the changing width and strength of the Hadley Cell, and are by themselves sufficient to determine the response of MHT to changing rotation rate. We also evaluate how eddies adjust in order to achieve the MHT in each experiment, and whether the eddies' activities scale with metrics such as the Rhines length that depends on rotation rate.

2.2 Experiments and Methods

We use the Geophysical Fluid Dynamics Laboratory Atmospheric Model, version 2.1 (GFDL AM2.1; Anderson et al. 2004) in aquaplanet configuration coupled to a 2.4 m slab ocean without sea ice component. The atmosphere model includes a prognostic cloud scheme in which cloud microphysics are parameterized according to Rotstayn (1997) and cloud fraction is parameterized following the Tiedtke (1993) (see Anderson et al. (2004) for more details). The model is run at a horizontal resolution of 2° latitude × 2.5° longitude with 24 levels. Insolation is set to its annual-mean value at each latitude. We prescribe in all experiments a zonally and hemispherically averaged ocean heat flux (Q-flux) to the slab ocean as in Rose and Ferreira (2012), which features a maximum poleward transport of 2.2 PW at 15° latitude and a zero global mean. Seven experiments are performed, in which the rotation rate is set to 1/16, 1/8, 1/4, 1/2, 1, 2 and 4 times the present-day value, respectively. Results of each experiment are presented in terms of the relative rotation rate $\mathbf{\Omega} = \Omega/\Omega_E$, where $\Omega_E = 7.292 \times 10^{-5}\, rad\, s^{-1}$ is the present terrestrial value.

2.3 Results

Figure 2.1 shows the meridional profile of surface temperature. As the rotation is increased, the surface temperature increases equatorward of 40° and stays constant or even decreases in the polar regions (except as $\mathbf{\Omega}$ changes from 1/16 to 1/8), resulting in an increase in the equator-to-pole temperature gradient. This feature is also seen in previous studies using different models (Williams and Holloway, 1982; Geisler et al., 1983; Del Genio and Suozzo, 1987; Williams, 1988; Jenkins, 1996; Navarra and Boccaletti, 2002), indicating that it is a robust feature across models. That the tropics warm as the rotation rate is increased is often attributed to a reduction in the poleward energy transport. However, additional experiments (described in section 6) show that tropical warming is due to increasing absorbed solar radiation via reduction in tropical clouds; the warming is further amplified by the water vapor feedback.

Consistent with the surface temperature, the meridional gradient of surface moist static energy also increases with increasing rotation (Fig. 2.2). Note that the degree of increase in the surface moist static energy gradient is much greater than that in the surface temperature gradient because of exponentially larger moisture loading in the tropics due to the Clausius-Clapeyron relationship. As will be discussed in section 5, this strong increase in the gradient of surface moist static energy compensates the weakening of the eddies and keeps the MHT relatively unchanged.

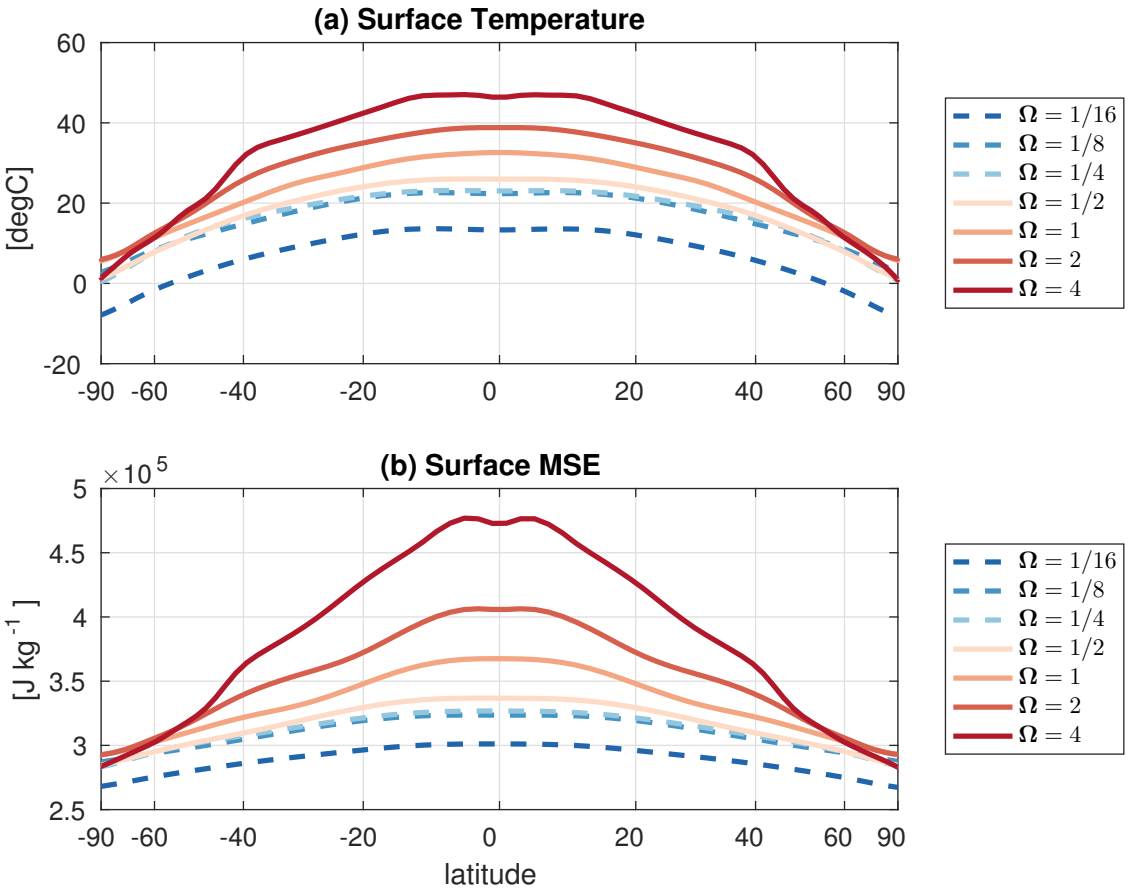

Figure 2.1: (a) Surface temperature, in degree Celcius, for various values of $\mathbf{\Omega}$. Note the displacement of latitude is area-weighted; hence, distance along the abscissa is linearly proportional to area covered. (b) same as (a), but for surface moist static energy (units: J kg^{-1}).

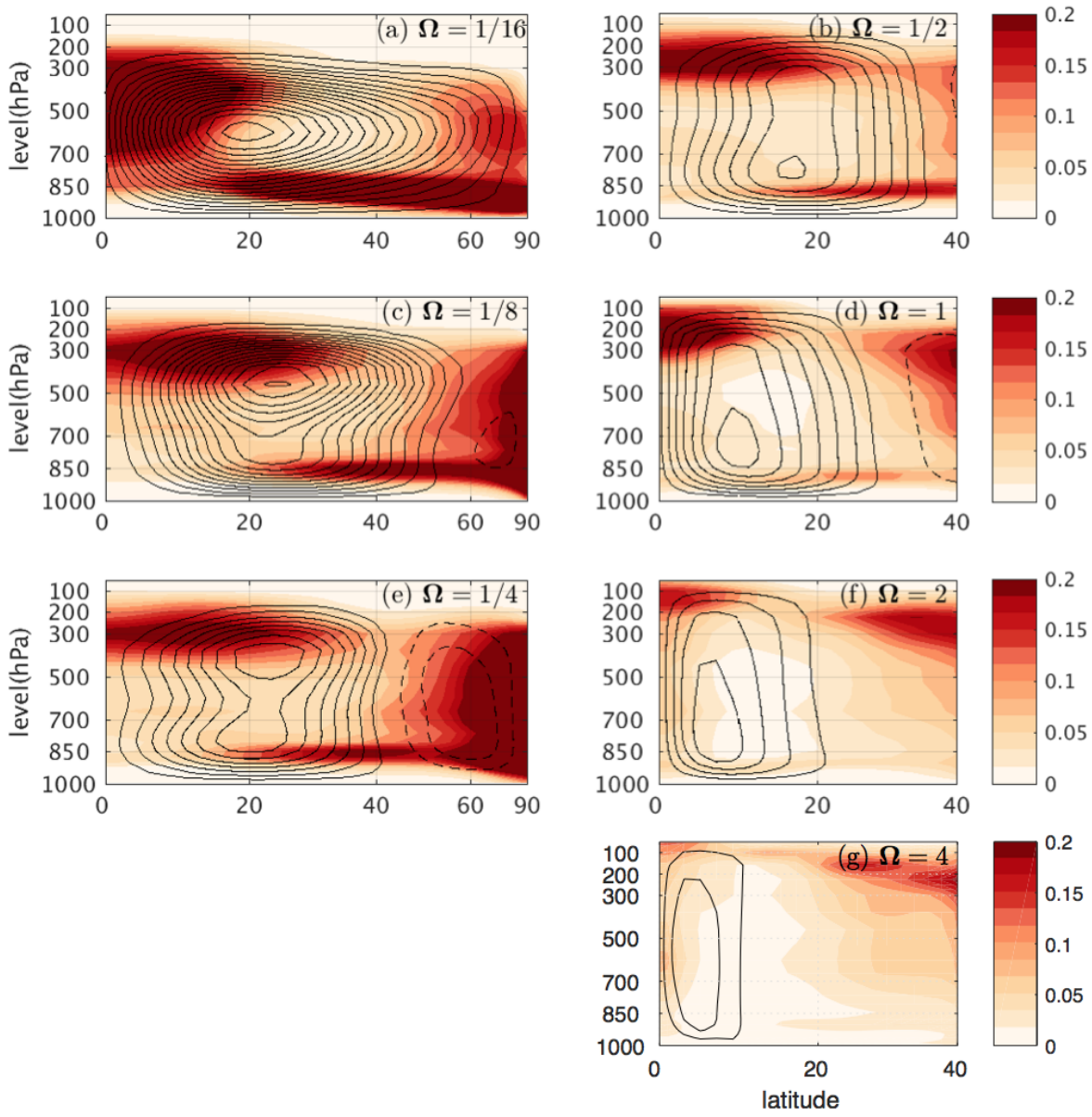

Figure 2.2: Cloud fraction (shading) overlayed with meridional streamfunction (contours) for each experiment; contours start from $\pm 20 \times 10^9 kg\ s^{-1}$, with intervals of $20 \times 10^9 kg\ s^{-1}$ for all experiments except for $\mathbf{\Omega} = 1/16$ (contours start from $\pm 40 \times 10^9 kg\ s^{-1}$ and with intervals $\pm 40 \times 10^9 kg\ s^{-1}$). Note the displacement of latitude is area-weighted. The latitude range in the right panels is 0 to 40° because in the fast-rotating regime ($\mathbf{\Omega} \geq 1/2$) clouds in the high latitudes are saturated and so changes do not affect the energy balance (see Figs. 8b,d).

In the control experiment ($\mathbf{\Omega} = 1$), the Hadley Cell extends from the equator to 30° latitude, approximating well the observed Hadley cell (Fig. 2.2) (Dima and Wallace, 2003). As rotation increases, the Hadley Cell becomes narrower and weaker (Fig. 2.2). The decrease in the width of the Hadley cell with increasing rotation is expected from the heuristic Held-Hou model (Held and Hou, 1980; Held, 2000).

The narrowing and weakening of the Hadley Cell is also associated with a weakening of the midlatitude eddies because the midlatitude eddy momentum fluxes contribute significantly to the width and strength of Hadley Cell: the strength of the meridional overturning circulation is proportional to the divergence of the eddy momentum flux (Schneider, 1984; Hess et al., 1993; Walker and Schneider, 2006; Vallis, 2006). Figure 2.3 shows the eddy momentum flux[1] at 300 mb. Averaged over the width of the Hadley Cell, the eddy momentum flux is a positive contribution to the strength of the Hadley Cell for all but the $\mathbf{\Omega} = 1/16$ case (Table 1). A measure of the relative importance of the eddy momentum fluxes to the strength of the Hadley circulation is given by the ratio of the average of the eddy momentum flux divergence over the Hadley Cell to the Hadley Cell strength, and referred to as the "eddy efficiency". Both the absolute amplitude of the eddy momentum flux divergence and the eddy efficiency are near extrema for the modern day rotation rate and greatly decay for both higher and lower rotation rate.

The maximum poleward MHT in the $\mathbf{\Omega} = 1$ experiment using AM2.1 is 5.4 PW at 35° (Fig. 2.4a) which is indistinguishable from that observed. The latitude of the maximum MHT increases somewhat with rotation rate: from about 25° for $\mathbf{\Omega} = 1/16$ to 38° for $\mathbf{\Omega} = 4$. With increasing rotation rate, MHT falls into two regimes (Fig. 2.4a): a "slow-rotating" regime, $1/16 \leq \mathbf{\Omega} < 1/2$, in which MHT decreases slightly with increasing rotation; and a "fast-rotating" regime, $\mathbf{\Omega} \geq 1/2$, in which MHT stays relatively unchanged with increasing rotation. This two-regime feature of MHT is evident for both maximum MHT ($\mathrm{MHT}_{\mathrm{max}}$)

[1]The eddy momentum flux is defined as the zonal mean time mean of the product of u' and v', where u and v are the zonal and meridional wind components and prime denotes the deviation from the zonal and time mean.

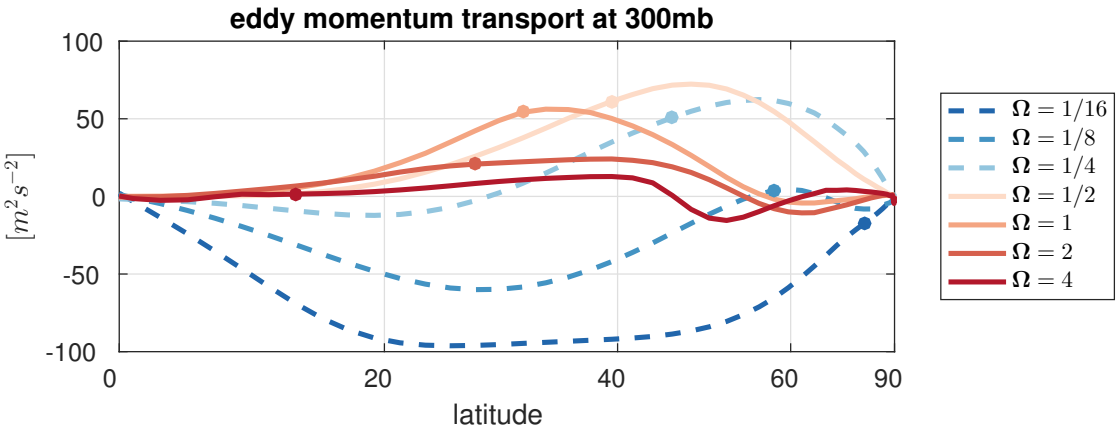

Figure 2.3: The eddy momentum transport measured by the zonal and temporal mean of $u'v'$ at 300mb, where u' and v' are the deviation of the zonal wind and meridional wind from their time and zonal mean, respectively (m^2 s^{-2}) for various values of $\mathbf{\Omega}$. The dot on each line that is of the same color as the line it resides on denotes the poleward edge of the Hadley Cell, i.e. the width of the Hadley Cell. Note the displacement of latitude is area-weighted.

(Fig. 2.4b) and the MHT averaged between 20° to 60° (Fig. 2.4c). In the following analysis, we will be using MHT_{max} as a metric of MHT to understand its change with rotation.

2.4 Understanding Changes in MHT in terms of Radiation

Our analysis of the changes in the MHT_{max} uses the diagnostics developed in Donohoe and Battisti (2012). In an equilibrium climate, MHT_{max} is equal to the net radiative surplus integrated over the tropics or, equivalently, the net radiative deficit integrated over the extratropics:

$$MHT_{max} = 2\pi R^2 \int_0^{x(ASR=OLR)} (ASR - OLR)dx \tag{2.1a}$$

$$= -2\pi R^2 \int_{x(ASR=OLR)}^{1} (ASR - OLR)dx, \tag{2.1b}$$

where x is the sine of latitude (Fig. 2.5). Since an equilibrium climate achieves global radiative equilibrium (that is, the globally integrated ASR is equal to that of OLR), we can

Table 2.1: The Hadley Cell strength versus the mean divergence of the eddy momentum flux. In the table below, width of the Hadley Cell (L_H) is determined as the first latitude poleward of the maximum absolute value of the Hadley Cell streamfunction at which the mass flux streamfunction at the sigma level of its extremum above sigma = 0.7 is 10% of its extremal value, following Walker and Schneider (2006). The Hadley Cell strength is defined as the maximum absolute value of the mass flux streamfunction. The mean divergence of the eddy momentum flux (column four) is the meridional average of the divergence of eddy momentum flux from the equator to L_H, that is, $\frac{\int_0^{L_H} \frac{d(\overline{u'v'})}{d\theta} cos\theta d\theta}{\int_0^{L_H} cos\theta d\theta}$, where $\overline{u'v'}$ is the eddy momentum flux and θ is latitude. Eddy efficiency is defined as the mean divergence of the eddy momentum flux divided by the strength of the Hadley Cell.

$\mathbf{\Omega}$	Width of the Hadley Cell	Hadley Cell strength ($10^{11} kg\ s^{-1}$)	mean divergence of eddy momentum flux ($10^{-5} m\ s^{-2}$)	eddy efficiency ($10^{-16} m\ s^{-1}\ kg^{-1}$)
1/16	74°	7.4	-0.22	0.005
1/8	58°	3.2	0.047	0.02
1/4	46°	1.8	1.1	0.57
1/2	39°	1.43	1.4	0.97
1	31°	1.41	1.5	1.03
2	27°	1.0	0.68	0.59
4	13°	0.6	0.084	0.54

subtract the global average of ASR and OLR from the right hand side to yield:

$$MHT_{max} = 2\pi R^2 \int_0^{x(ASR'=OLR'=0)} (ASR' - OLR')dx \tag{2.2a}$$

$$= -2\pi R^2 \int_{x(ASR'=OLR'=0)}^{1} (ASR' - OLR')dx, \tag{2.2b}$$

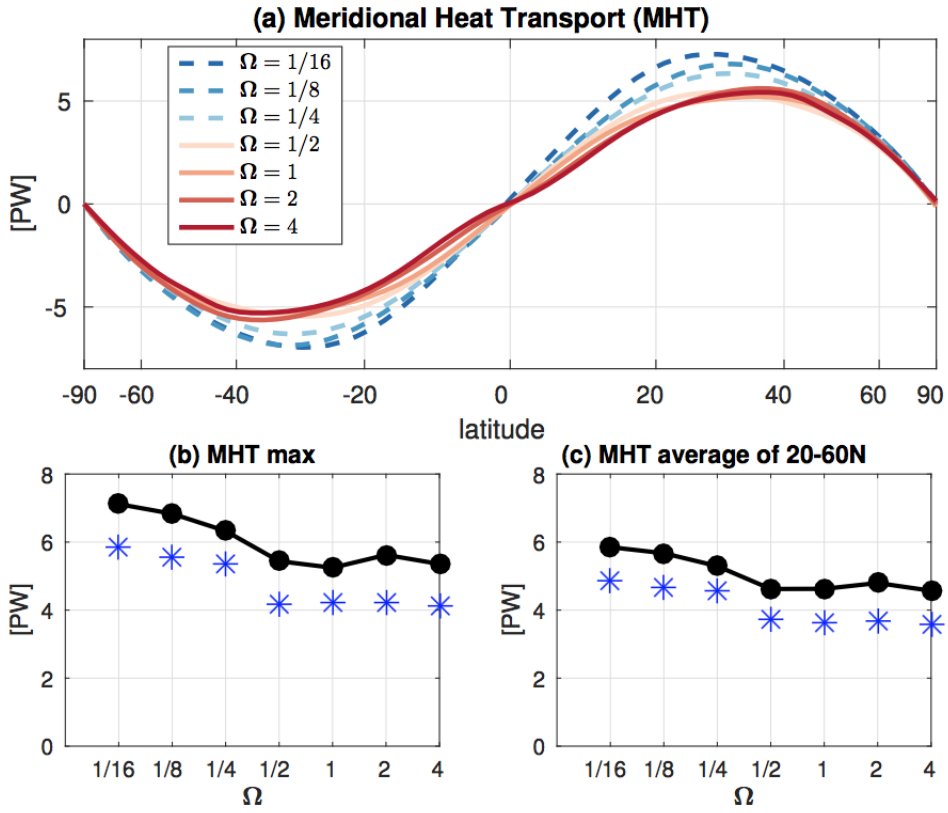

Figure 2.4: (a) The total meridional energy transport, in PW, for various values of $\mathbf{\Omega}$. Note the displacement of latitude is area-weighted. (b) and (c) are the peak value of the meridional energy transport and the transport averaged between 20-60°, respectively. The uncertainty in $\mathrm{MHT}_{\mathrm{max}}$ is typically +/- 0.2 PW. Blue stars are for the experiments without Q-flux.

where primes denote deviations from the global average and it has been assumed that $x(ASR' = 0) = x(OLR' = 0)$. Eqs. (2.2a) and (2.2b) can be combined to give:

$$MHT_{max} = \frac{1}{2}\left(2\pi R^2 \int_0^{x(ASR'=OLR'=0)} (ASR' - OLR')dx - 2\pi R^2 \int_{x(ASR'=OLR'=0)}^{1} (ASR' - OLR')dx \right) \tag{2.3a}$$

$$\approx ASR^* - OLR^*, \tag{2.3b}$$

Table 2.2: Decomposition of atmospheric heat transport (AHT) into the contribution by mean meridional circulation (MMC) and the contribution by eddies. The contribution by MMC is calculated as $\int_{-\pi/2}^{0}\int_{0}^{2\pi}(\int_{p_s}^{0}[v][h]dp)cos\theta d\lambda d\theta$, where v is the meridional wind, h is the moist static energy, p is pressure, p_s is surface pressure, θ is latitude, λ is longitude and $[\cdot]$ denotes zonal and temporal mean. The eddy energy transport is defined as the residual of the MMC transport from the total AHT estimated as $\int_{-\pi/2}^{0}\int_{0}^{2\pi}(\int_{p_s}^{0}(vhdp)cos\theta d\lambda d\theta$. In the calculation of total AHT, the vertical integral of vh is calculated at the model grid at each time step. In the table below, lat_{max} denotes the latitude where AHT calculated from the meridional integral of the net heat flux into the atmosphere reaches its maximum value.

$\mathbf{\Omega}$	lat_{max}	MMC transport (PW)	Eddy transport (PW)	MMC + Eddy (PW)	AHT_{max} (PW)
1/16	33°	4.8	1.1	5.9	5.8
1/8	35°	2.9	2.8	5.7	5.5
1/4	35°	1.4	3.6	5.0	5.1
1/2	37°	0.2	3.8	4.0	4.1
1	41°	-0.6	4.8	4.2	4.3
2	39°	0.0	4.5	4.5	4.6
4	39°	-0.1	4.2	4.1	4.5

where

$$ASR^* \equiv \frac{1}{2}\left(2\pi R^2 \int_0^{x(ASR'=0)} ASR' dx - 2\pi R^2 \int_{x(ASR'=0)}^{1} ASR' dx\right) \tag{2.4}$$

and

$$OLR^* \equiv \frac{1}{2}\left(2\pi R^2 \int_0^{x(OLR'=0)} OLR' dx - 2\pi R^2 \int_{x(OLR'=0)}^{1} OLR' dx\right). \tag{2.5}$$

ASR* is the surplus of ASR in the tropics relative to the global mean, and OLR* is the surplus of OLR relative to the same global mean (or equivalently, ASR* and OLR*, respectively, are the deficit of ASR and the deficit of OLR in the extratropics relative to the global mean). Thus, Eqn. 2.3b is a compact representation of the relationship that must exist between the poleward energy transport and the spatial patterns of ASR and OLR. ASR* and OLR* are fundamental to the energetic gradients that must be accommodated by transport. A graphical illustration of the meaning of ASR* and OLR* is provided in Fig. 2.5 for the

observed climate. The decomposition into ASR* and OLR* provides insight into processes acting via shortwave and longwave fluxes. Changes in the $\mathrm{MHT}_{\mathrm{max}}$ from one experiment to another can thus be understood in terms of changes in ASR* and/or OLR*. In the following text, we will use this method to analyze the different behaviors of MHT as a function of rotation in each regime.

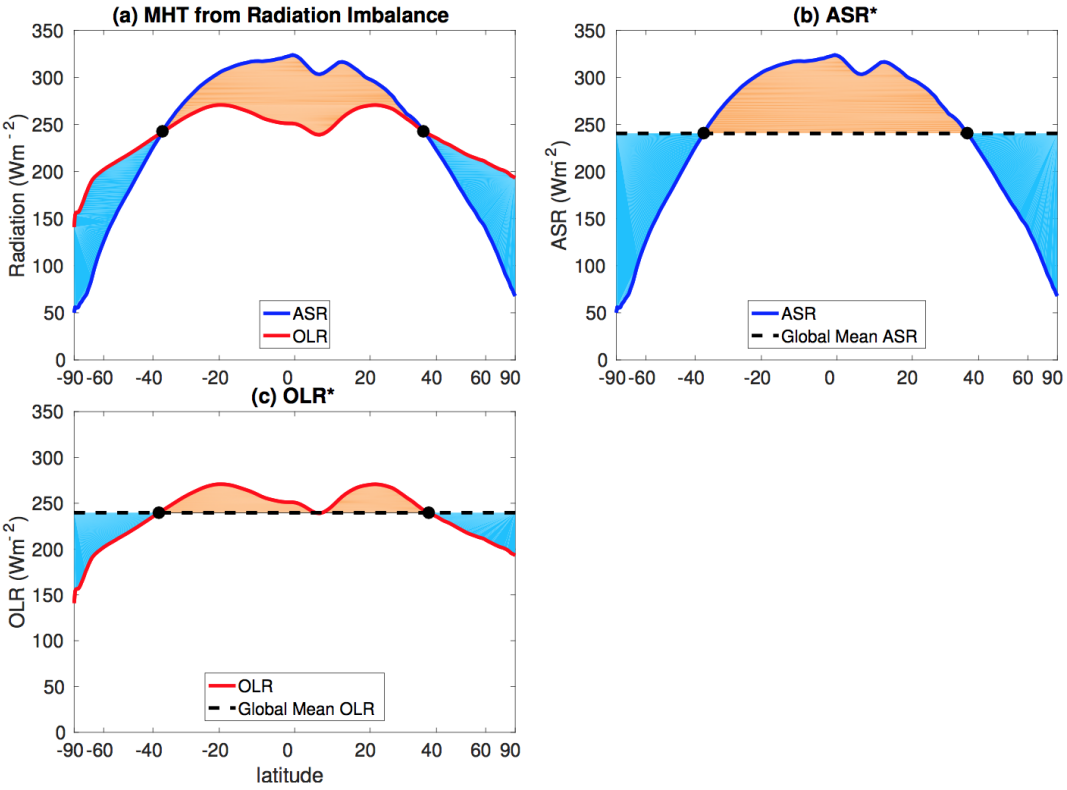

Figure 2.5: Graphical illustration of the calculation of (a) the maximum meridional heat transport ($\mathrm{MHT}_{\mathrm{max}}$), (b) ASR* and (c) OLR*. For each variable, i.e. $\mathrm{MHT}_{\mathrm{max}}$, ASR* and OLR*, and for each hemisphere, the surplus in the tropics relative to the global mean is shaded orange, while the deficit in the extratropics relative to the global mean is shaded blue. Reproduced from Donohoe and Battisti (2012) with permission.

It is worth noting that the near equality in Eqn. (2.3b) holds exactly when the meridional nodes of ASR′ and OLR′ are collocated, which is true for the fast-rotating regime ($\mathbf{\Omega} \geq 1/2$)

but not for the slow-rotating regime ($\mathbf{\Omega} < 1/2$). Nonetheless, even for the slow-rotating regime, this method gives a fair estimate of the change of $\mathrm{MHT_{max}}$ with rotation rate: $\mathrm{ASR^* - OLR^*}$ underestimates $\mathrm{MHT_{max}}$ by only 3 to 16%, depending on rotation rate (cf. Figs. 2.4c and 2.6c). The results shown below are not sensitive to the small changes in the latitude of the nodal points associated with the changes in rotation rate: the same results are found when the nodal point from the $\mathbf{\Omega} = 1$ experiment is used to estimate $\mathrm{ASR^*}$ and $\mathrm{OLR^*}$ for each of the experiments.

2.4.1 The fast-rotating regime

In the fast-rotating regime ($\mathbf{\Omega} \geq 1/2$), both $\mathrm{OLR^*}$ and $\mathrm{ASR^*}$ increase with rotation rate and they increase by approximately equal amounts (Fig. 2.6a, b); as a result, $\mathrm{MHT_{max}}$ is largely insensitive to rotation rate.

To understand why both $\mathrm{ASR^*}$ and $\mathrm{OLR^*}$ increase with increasing rotation rate, we further partition $\mathrm{ASR^*}$ and $\mathrm{OLR^*}$ into the contribution from the clear-sky ($\mathrm{ASR^*_{clr}}$ and $\mathrm{OLR^*_{clr}}$) and the contribution from the clouds ($\mathrm{ASR^*_{cld}}$ and $\mathrm{OLR^*_{cld}}$). Similar to $\mathrm{ASR^*}$ and $\mathrm{OLR^*}$ (cf. Eqs. 2.4 and 2.5), $\mathrm{ASR^*_{clr}}$ and $\mathrm{OLR^*_{clr}}$ are defined to be

$$ASR^*_{clr} = \frac{1}{2}\left(2\pi R^2 \int_0^{x(ASR'_{clr}=0)} ASR'_{clr}dx - 2\pi R^2 \int_{x(ASR'_{clr}=0)}^{1} ASR'_{clr}dx\right) \tag{2.6}$$

and

$$OLR^*_{clr} = \frac{1}{2}\left(2\pi R^2 \int_0^{x(OLR'_{clr}=0)} OLR'_{clr}dx - 2\pi R^2 \int_{x(OLR'_{clr}=0)}^{1} OLR'_{clr}dx\right). \tag{2.7}$$

$\mathrm{ASR^*_{cld}}$ and $\mathrm{OLR^*_{cld}}$ are given by

$$ASR^*_{cld} = ASR^* \; - \; ASR^*_{clr} \tag{2.8}$$

and

$$OLR^*_{cld} = OLR^* \; - \; OLR^*_{clr}. \tag{2.9}$$

$\mathrm{ASR^*_{clr}}$ and $\mathrm{OLR^*_{clr}}$ thus represent the equtor-to-pole gradient of the absorbed clear-sky shortwave radiation ($\mathrm{ASR_{clr}}$) and clear-sky outgoing longwave radiation ($\mathrm{OLR_{clr}}$), respectively.

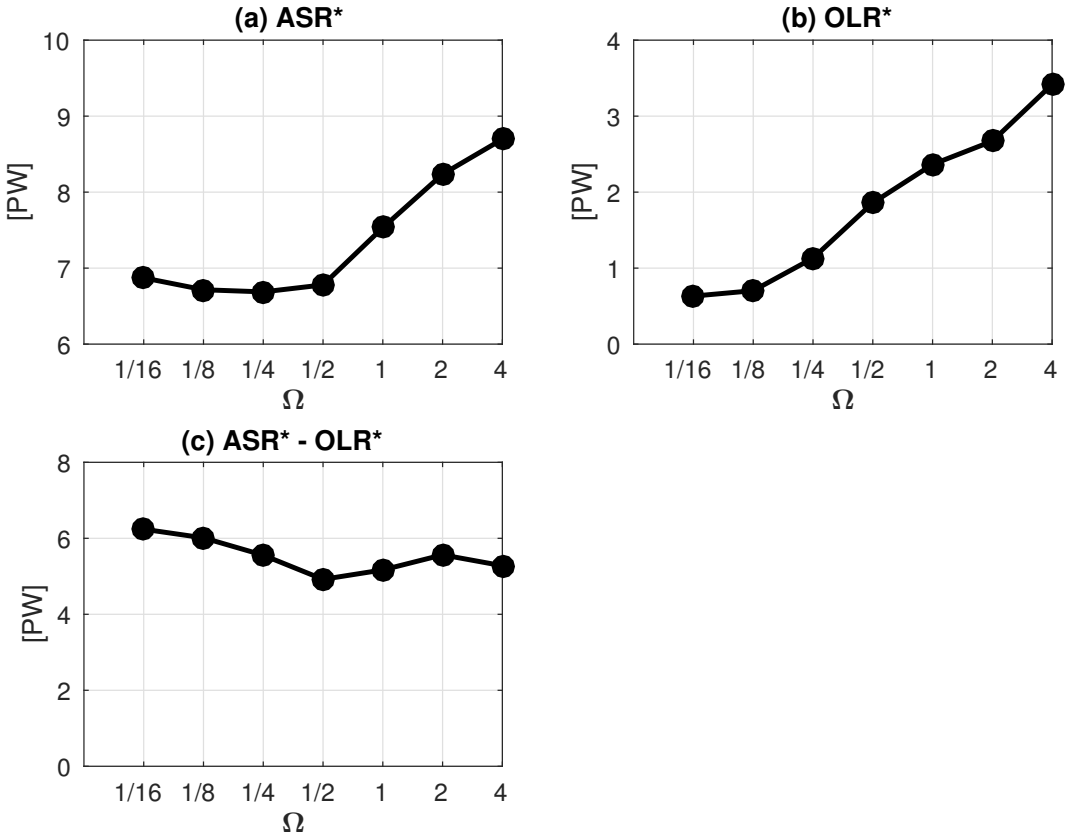

Figure 2.6: ASR* (a; positive downward) and OLR* (b; positive upward), in PW, for each experiment. (c) is the difference between (a) and (b).

$\mathrm{ASR}^*_{\mathrm{cld}}$ describes the equator-to-pole gradient of $\mathrm{ASR}_{\mathrm{cld}}$, the shortwave cloud forcing (that is, the negative of the shortwave reflected by clouds). Similarly, $\mathrm{OLR}^*_{\mathrm{cld}}$ describes the equator-to-pole gradient of $\mathrm{OLR}_{\mathrm{cld}}$, the longwave cloud forcing (that is, the negative of the longwave trapped by the clouds).

In the fast-rotating regime, $\mathrm{ASR}^*_{\mathrm{clr}}$ is essentially invariant of rotation rate (Fig. 2.7a). Therefore, the increase of ASR* with increasing rotation rate is due predominantly to an increase in $\mathrm{ASR}^*_{\mathrm{cld}}$ (cf. Figs. 2.6a and 2.7c). The change in $\mathrm{ASR}^*_{\mathrm{clr}}$ and $\mathrm{ASR}^*_{\mathrm{cld}}$ can be understood by examining the spatial patterns of $\mathrm{ASR}_{\mathrm{clr}}$ and $\mathrm{ASR}_{\mathrm{cld}}$ (Figs. 2.8a,b). $\mathrm{ASR}_{\mathrm{clr}}$ remains nearly constant with rotation rate at each latitude because of the unchanging geometry and solar constant; for all the experiments, the shortwave reflected by the clouds $\mathrm{ASR}_{\mathrm{cld}}$ remains

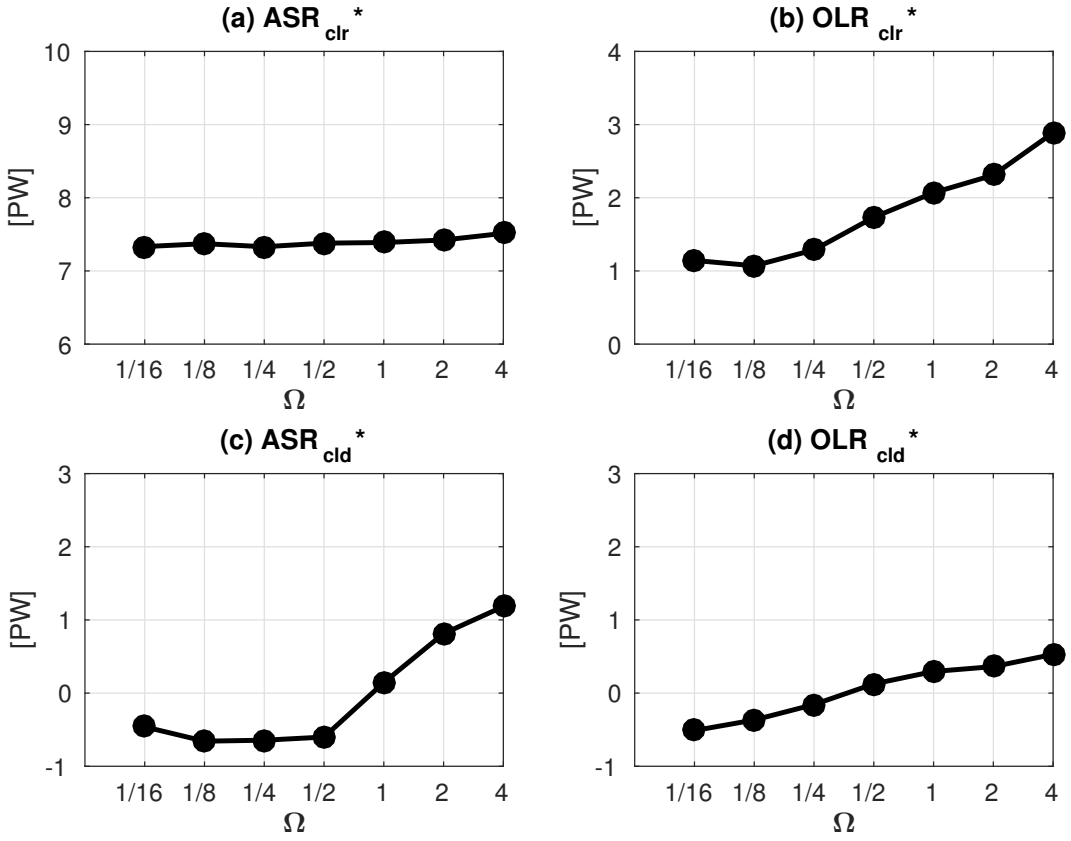

Figure 2.7: Clear-sky ASR^*, $\mathrm{ASR}^*_{\mathrm{clr}}$ (a) and clear-sky OLR^*, $\mathrm{OLR}^*_{\mathrm{clr}}$ (b), in PW, for each experiment. (c) and (d) are the same as (a) and (b), but for $\mathrm{ASR}^*_{\mathrm{cld}}$ and $\mathrm{OLR}^*_{\mathrm{cld}}$, which are defined as $ASR^* - ASR^*_{clr}$ and $OLR^* - OLR^*_{clr}$, respectively.

negative, as it must be by definition. As the rotation is increased, $\mathrm{ASR}_{\mathrm{cld}}$ is less negative equatorward of 40°, indicating that less shortwave is reflected by clouds. This results in an decrease in the equator-to-pole gradient of shortwave reflected, or equivalently, an increase in the equator-to-pole difference of $\mathrm{ASR}_{\mathrm{cld}}$ ($= 2\mathrm{ASR}^*_{\mathrm{cld}}$).

The reduction in the shortwave reflected in the tropics, in turn, is related to a reduction in the high cloud amount from the equator to 20° and a reduction in the low cloud amount from 20° to 40° (Figs. 2.2b, d, f and g); both are associated with the change in the Hadley Cell. As shown in Fig. 2.2, the tropical high clouds are associated with the ascending branch of the Hadley cell and the subtropical low clouds are associated with the sinking branch; both

types of clouds reduce with the weakening and shrinking of the Hadley cell with increasing rotation. Poleward of 40°, $\mathrm{ASR_{cld}}$ stays relatively unchanged because cloud changes are constrained to be over the polar cap where the insolation is weak and clouds are prevalent in all experiments.

The increase in OLR^* with the increasing rotation rate is primarily due to an increase in $\mathrm{OLR}^*_{\mathrm{clr}}$ and secondarily to an increase in $\mathrm{OLR}^*_{\mathrm{cld}}$ (Figs. 2.7b and 2.7d). The increase in $\mathrm{OLR}^*_{\mathrm{clr}}$ with increasing rotation rate is mainly due to an increase in clear-sky OLR equatorward of 20°, consistent with the surface warming in the tropics as rotation is increased (cf. Figs. 2.8c and 2.1). The longwave cloud forcing ($\mathrm{OLR_{cld}}$) is a positive contribution to OLR^*: as the rotation rate is increased, less longwave is trapped by clouds in the tropics; therefore, the equator-to-pole gradient of $\mathrm{OLR_{cld}}$ ($\mathrm{OLR}^*_{\mathrm{cld}}$) increases. The reduction in the trapped longwave is associated with the reduction in the tropical high cloud amount (Figs. 2.2b, d, f and g) which is related to the weakening and narrowing of the Hadley cell (Fig. 2.2).

2.4.2 The slow-rotating regime

In the slow-rotating regime ($\boldsymbol{\Omega} < 1/2$), ASR^* is nearly invariant with rotation, but OLR^* increases as the rotation is increased, resulting in a decrease in $\mathrm{MHT_{max}}$ with increasing rotation (Fig. 2.6). OLR^* increases with rotation primarily due to an increase in $\mathrm{OLR}^*_{\mathrm{clr}}$ (Figs. 2.7b,d).

As in the fast-rotating regime, the increase in $\mathrm{OLR}^*_{\mathrm{clr}}$ with increasing rotation rate is mainly due to an increase in clear-sky OLR in the tropics. Note that the temperature change in the slow-rotation regime is nearly uniform globally, resulting in a larger increase in clear-sky OLR in the tropics than in the polar regions via the nonlinear Planck response (Figs. 2.9c, d). The increase in $\mathrm{OLR}^*_{\mathrm{cld}}$ with increasing rotation rate is due to an decrease in longwave trapping by clouds in the tropics which, in turn, is related to the decrease in tropical high cloud amount associated with the weakening of the Hadley cell (Figs. 2.2a, c, e).

ASR^* does not change with the rotation in the slow-rotating regime because neither

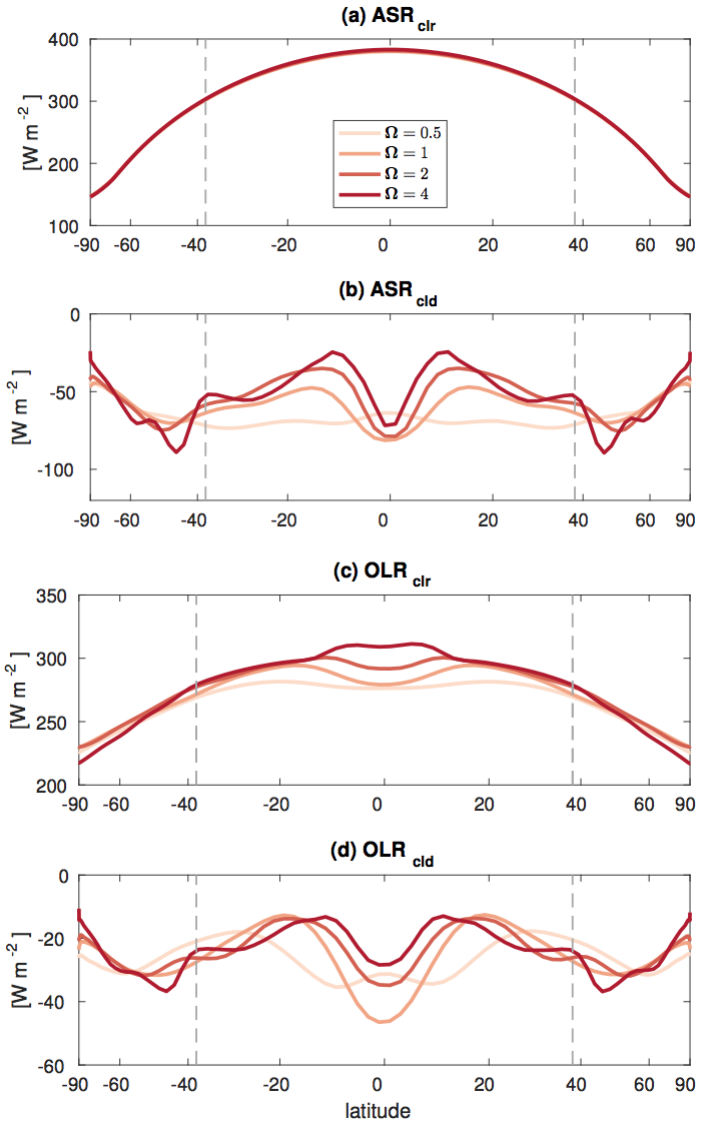

Figure 2.8: The clear-sky ASR, $\mathrm{ASR_{clr}}$ (a) and impact of clouds on ASR, $\mathrm{ASR_{cld}}$ (b), in $W\ m^{-2}$, for experiments in the fast-rotating regime. Note the displacement of latitude is area-weighted. (c) and (d) are the same as (a) and (b), but for OLR. The gray dashed lines indicate location of the nodal point of $\mathbf{\Omega} = 1$. Note the different y-axes in each panel. The results illustrate that the biggest changes are equatorward of the nodal point.

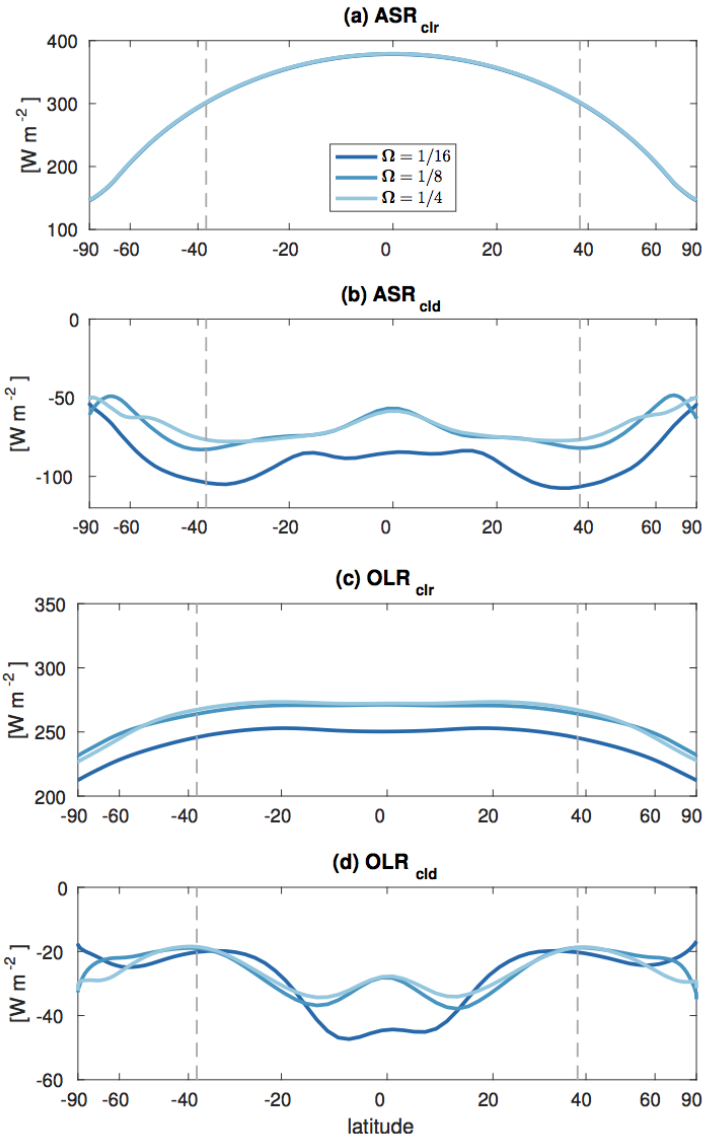

Figure 2.9: Same as Fig. 2.8, but for experiments in the slow-rotating regime.

$\mathrm{ASR}^*_{\mathrm{clr}}$ nor $\mathrm{ASR}^*_{\mathrm{cld}}$ change (Fig. 2.7a,c). $\mathrm{ASR}^*_{\mathrm{cld}}$ remains nearly invariant because as rotation rate increases, $\mathrm{ASR}_{\mathrm{cld}}$ increases the same amount equatorward of the nodal point (roughly 35°) as it does poleward of the nodal point (Fig. 2.9b). The increase in ASR is predominantly due to the reduction in the low clouds (Figs. 2.2a, c, e) that stems from the weakened subsidence associated with the sinking branch of the Hadley cell (note that the Hadley cell is much wider in the slow-rotating regime and extends to the pole in the $\mathbf{\Omega} = 1/16$ experiment). This relationship between the changes of clouds and the changes of the Hadley cell is the same as that of the fast-rotating regime. Although there are large changes in tropical high clouds and middle-to-high clouds in the polar regions, they do not impact the shortwave and hence ASR^* significantly.

2.5 The Connection with Dynamics

For $\mathbf{\Omega} \geq 1/4$ the MHT is accomplished predominantly by the eddies (Table 2). It might be expected that eddy heat transport would depend on the geometry and intensity of the eddies that, in turn, depend on rotation rate via eddy metrics (see Barry et al., 2002 for an important review), such as the Rhines scale (which scales as the inverse of the square root of the meridional gradient of the Coriolis parameter), or the maximum Eady growth rate (which scales as the Coriolis parameter). Turbulence mixing theory suggests that eddy diffusivity scales as VL where V and L are eddy velocity and meridional length scales, respectively (e.g., Vallis, 2006). Figures 2.10a and b show V and L area-averaged between 30° and 60°. Following Barnes and Hartmann (2012), V is taken to be the root-mean-square of the instantaneous (6 hourly) 850mb meridional wind averaged over each latitude band and over time (V_{RMS}); and L is defined as the meridional distance over which the autocorrelation in the instantaneous meridional wind decays by a factor of e. Also shown in Figures 2.10 a and b, respectively, are a velocity scale developed by Barry et al. (2002) [2] and the Rhines β-scale,

[2]Barry et al's velocity scale is $V = V_b \propto (a\overline{T}_y q/T_0)^{2/5}(2/\beta)^{1/5}$, where a is the radius of the Earth, $\overline{T}_y$ and T_0 are the 1000-200 mb vertically integrated meridional gradient of zonal mean temperature and the mean temperature area-averaged over the mid-latitudes (taken to be 30°to 60° latitude), respectively, and following Lapeyre and Held (2003) q is the average heating rate poleward of the latitude of maximum

defined as $\sqrt{\frac{2V}{\beta}}$ where V is, as in the present study, the root-mean-square of meridional velocity.

V weakly depends on the rotation rate – it decreases only slightly as the rotation rate is increased (except for $\mathbf{\Omega} = 4$) (Fig. 2.10a). Across all of the experiments, there is a qualitative similarity between V and the velocity scale developed by Barry et al. (2002). The implication is that the weak dependence of V on rotation is because the increase in baroclinicity with increasing rotation rate is partly offset by the increase in β. L decreases with increasing rotation rate, almost exactly following the change of the Rhines β-scale (Fig. 2.10b), consistent with Barnes and Hartmann (2012). The suggested scaling for eddy diffusivity, VL, decreases monotonously with increasing rotation, mainly associated with the decrease in L (Fig. 2.10c). This implies that the eddies are less effective at transporting heat as the rotation is increased.

Several recent studies have shown atmospheric heat transport (AHT) in GCMs can be emulated by simple downgradient diffusion of near-surface moist static energy (e.g., Flannery, 1984; Frierson et al., 2007; Hwang and Frierson, 2010; Jansen and Ferrari, 2015; Rose et al., 2014; Roe et al., 2015):

$$AHT = -2\pi \cos\theta \frac{p_s}{g} D_{eff}(\theta) \frac{dh}{d\theta}, \tag{2.10}$$

where θ is latitude, p_s/g is mean mass per unit area (taken to be a constant, $10^4\ kg\,m^{-2}$), $\mathrm{D_{eff}}(\theta)$ is the effective diffusivity as a function of latitude, and $h = c_pT + L_vq$ is the near-surface moist static energy (where c_p is specific heat, T temperature, L_v latent heat of vaporization, and q is specific humidity). $\mathrm{D_{eff}}$ can be diagnosed from model output using Eq. (2.10). Figure 2.10c presents a scatter plot of $\mathrm{D_{eff}}$ vs. VL as a function of rotation rate. $\mathrm{D_{eff}}$ decreases by approximately ten-fold as $\mathbf{\Omega}$ increases from 1/16 to 4. There is an impressive, near-linear association between $\mathrm{D_{eff}}$ and VL over a 64-fold variation in rotation rate – the correlation coefficient between these two exceeds 0.99. The results thus show that the model heat transport is indeed approximately diffusive, with an effective diffusivity that

---

AHT. The arbitrary constant is chosen such that V_b matches V_{RMS} at $\mathbf{\Omega} = 1$.

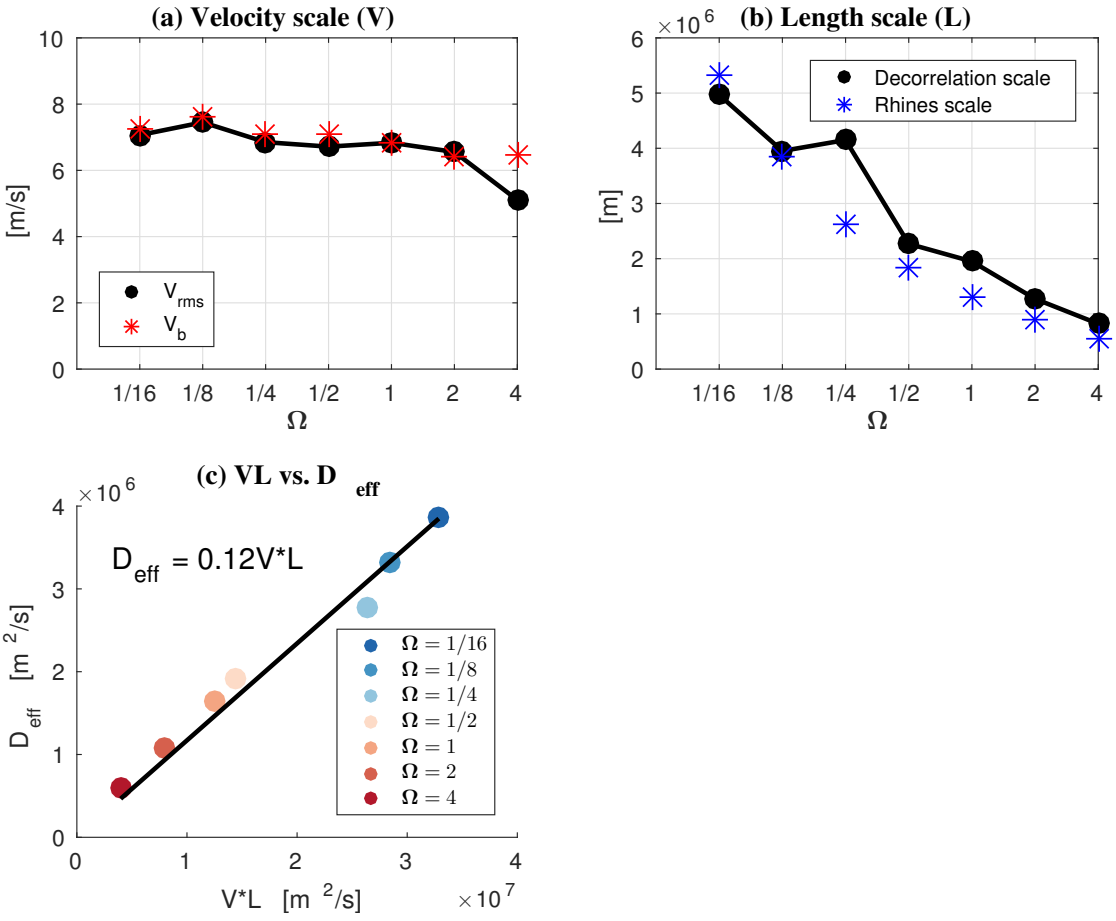

Figure 2.10: (a) Eddy length scale (L) and (b) Eddy velocity scale (V) area-averaged between 30° to 60° for various values of $\mathbf{\Omega}$. (c) scatter plot of effective eddy diffusivity D_{eff} (see Eqn. 2.10 for definition) versus VL averaged between 30° to 60° for the whole ensemble of experiments.

is consistent with eddy mixing-length theory. This is even true in the slow-rotating regime where the eddies are not the dominant transport mechanism. The results are also consistent with the idea that eddies are less effective at transporting heat at higher rotation rates.

Despite the ten-fold decrease in D_{eff}, AHT and hence MHT (because the ocean heat transport is fixed in this series of experiments) changes by no more than about about 30% across this range (Table 2). The reason is that the decrease in D_{eff} is nearly offset by the strong increase in the gradient of moist static energy associated with the tropical warming at high rotation rates (Fig. 1b).

2.6 Discussion

It is evident from the above analysis that the regime feature of MHT with increasing rotation rate is related to the regime behavior of ASR^*_{cld}: it is nearly constant in the slow-rotating regime but increases with increasing rotation in the fast-rotating regime. Why does ASR^*_{cld} change differently with rotation rate in these two regimes, given that the patterns of change in cloudiness that are essential to the change in ASR^*_{cld} are the same for both regimes? It is related to the mean distribution of tropical and subtropical clouds that are associated with the Hadley cell. In both regimes, the tropical high clouds are associated with the rising branch of the Hadley cell and the subtropical low clouds are associated with the sinking branch of the Hadley cell. In the slow-rotating regime, the subtropical low clouds decrease on both the equatorward and the poleward sides of the nodal point (roughly 36°) (Figs. 2.2a, c, e) because the Hadley cell extends poleward of the nodal point, resulting in a near-zero change in the equator-to-pole *gradient* of ASR_{cld}, that is ASR^*_{cld}. On the contrary, in the fast-rotating regime the reduction in tropical high clouds and the reduction in subtropical low clouds are both equatorward of the nodal point (Figs. 2.2b, d, f and g) so they work in a concerted way to reduce the shortwave reflected and hence cause a net increase in ASR^*_{cld} as rotation rate increases.

In terms of dynamics, the two-regime nature of MHT is related to the Clausius-Clapeyron relationship which increases the meridional gradient of surface moist static energy more

dramatically in the fast-rotating regime (Fig. 1b), compensating for the decrease in eddy diffusivity (Fig. 2.10). In the slow-rotating regime, however, because the increase in the gradient of surface moist static energy is not sufficient to compensate the decrease in eddy diffusivity, the MHT decreases with increasing rotation rate. Our results contrast with those of Vallis and Farneti (2009) who found that the MHT decreases monotonously with increasing rotation rate. The primary reason for this difference is the choice of atmosphere models: Vallis and Farneti (2009) use a gray atmosphere with fixed spatial distribution of clouds; as a result, ASR* cannot change with rotation rate. In contrast in our experiments, changing ASR* causes changes in tropical temperature and moist static energy which, in turn, affect the meridional gradient and hence the flux of moist static energy.

Another striking feature revealed in this study is that the eddy diffusivity scales linearly with the effective eddy diffusivity (Fig. 2.10c). The linearity implies an important constraining relationship between the dynamics and the radiation.Our results above suggests that changes in clouds are fundamental to the insensitivity of MHT to rotation. To further test the role of clouds, we repeated the experiments with a gray radiation model in which clouds and longwave emissivity are prescribed. We found that when clouds and water vapor feedback are omitted, the tropical warming is much smaller, ASR* stays constant and OLR* increases with increasing rotation for $\mathbf{\Omega} < 1/2$ and keeps relatively unchanged for $\mathbf{\Omega} \geq 1/2$. This conclusion is further supported by two additional sets of experiments, increasing the rotation rate from $\mathbf{\Omega} = 1/16$ to $\mathbf{\Omega} = 4$: in the first set of experiments, SST was fixed to be that from the control ($\mathbf{\Omega} = 1$) experiment using the slab ocean; in the second set of experiments, the rotation rate is held fixed at $\mathbf{\Omega} = 1$, but the SST is prescribed to be that from the varying rotation experiments using the slab model. Comparing the results from these two sets of experiments to those using the slab model, we found that: (i) the change in clouds and hence in ASR* is primarily due to the changes in the Hadley cell due to changes in rotation – the tropical ASR increases with rotation in the variable-rotation-fixed-SST experiments, but not in the variable-SST-fixed-rotation experiments; and (ii) the change in Hadley cell is predominantly determined by change in the rotation without changing SST –

the Hadley cell contracts and weakens with increasing rotation in the variable-rotation-fixed-SST experiments, but strengthens and widens slightly with increasing rotation in the set of variable-SST-fixed-rotation experiments, in contrast to what is seen in the experiments using slab model.

In the present study, we used the same fixed Q-flux for all of the experiments; if we had used a dynamic ocean model the ocean heat transport would also change with changes in rotation rate. However, using the fixed Q-flux is reasonable in the sense that $\mathrm{MHT}_{\mathrm{max}}$ is dominated by the atmospheric heat transport and therefore should be relatively insensitive to changes in ocean heat transport. We also performed another set of rotation rate experiments in which no Q-flux is used. For this set of experiments, the behavior of MHT, ASR* and OLR* with rotation is the same as discussed in sections 3 and 4 (Figs. 2.4b, c).

The change of MHT with rotation rate is independent of the model resolution. To better resolve the eddies in the fast rotation rate experiments, we performed another set of experiments in which the horizontal resolution is doubled (from $2.0^\circ \times 2.5^\circ$ to $1.0^\circ \times 1.25^\circ$). For each rotation rate, MHT, ASR* and OLR* differ by only 2% to 10% when the model resolution is doubled (not shown). The changes in cloudiness, circulation, radiation and so on that underlie the changes in ASR* and OLR* (and hence MHT) are also independent of the model resolution used. The only notable difference between the sets of high- and low-resolution experiments is that the former set features double Intertropical Convergence Zones (ITCZs), whereas the latter set features a single ITCZ on the equator.

We also repeated our experiments and analysis using the NCAR aquaplanet CAM4 coupled to a slab ocean to examine the model dependence of our results. We found that the dynamics and the radiative fluxes in NCAR CAM4 change with rotation in exactly the same way as those in GFDL AM2.1: as the rotation is increased, the Hadley cell contracts and weakens, and the associated tropical and subtropical clouds are reduced; as a result, ASR increases in the tropics, the tropical temperature increases, the clear-sky OLR increases, and less longwave is trapped by clouds. Hence, just as in the experiments with the AM2 coupled to a slab ocean, both ASR* and OLR* increase as rotation rate increases in the CAM4 plus

slab model, leading to modest change in MHT (figures not shown). Encouragingly, other studies also have found that tropical temperatures increase and subtropical clouds decrease as rotation rate is increased (e.g., Jenkins et al., 1993, using the NCAR Community Climate Model (CCM), Navarra and Boccaletti, 2002, using ECHAM 4, and Salameh et al., 2017, using ECHAM 6). Together, our results and the aforementioned studies give us confidence that as rotation rate increases, changes in clouds will cause changes in ASR that will tend to be compensated by changes in OLR, resulting in only modest changes in MHT relative to those in ASR and OLR – although the degree of compensation might be sensitive to the parameterization of cloud processes, ice microphysics, and the parameterization of the PBL.

2.7 Summary

The atmosphere-ocean system transports energy meridionally from the equator towards the poles. The magnitude of this meridional heat transport (MHT) is such as to achieve a balance between the pattern of absorbed shortwave radiation (ASR) and the pattern of outgoing longwave radiation (OLR) at the top of the atmosphere. In this study we have sought to understand what controls the magnitude of MHT by varying the Earth's rotation rate in a series of numerical experiments. The essential result is that the changes in rotation rate cause changing patterns of clouds. The resulting changes in ASR* and OLR* control changes in MHT. In this regard our results are consistent with a recent study that demonstrated that the large ($\sim$ 2 PW) spread in $\mathrm{MHT}_{\mathrm{max}}$ among CMIP3 GCMs for the modern climatology is related to differences in their representation of ASR* associated with difference in cloud shortwave forcing (Donohoe and Battisti, 2012).

Consistent with basic theory and several other modeling studies, we find that an increasing rotation rate causes a narrowing and weakening of the Hadley Cell. Changes in MHT are linked to the accommpanying changes in both tropical high and subtropical low clouds. For the GFDL AM2.1 model (and for the NCAR CAM4 model), we find two distinct regimes: i) a slowly rotating regime (rotation less than half present-day value) where, with increasing rotation rate, high tropical clouds disperse leading to less trapping of OLR, more local

accommodation of ASR, and hence a reduction in MHT (about 30% going from $\mathbf{\Omega} = 1/16$ to $\mathbf{\Omega} = 1/2$); and ii) a fast rotating regime (rotation greater than half present-day value) where, with increasing rotation rate, there are closely off-setting changes in OLR* and ASR* (the latter mediated by changes in low subtropical clouds), such that MHT remains nearly invariant ($< 5\%$ change going from $\mathbf{\Omega} = 1/2$ to $\mathbf{\Omega} = 4$).

While the detailed response of MHT to rotation rate will of course depend on the GCM used, the basic cloud response to increasing rotation is found in several different models. The fundamental point is that changing cloud patterns are first-order controls on ASR* and OLR* and hence MHT. Our results echo the principle idea laid out in Stone (1978) of the importance of top-of-atmosphere fluxes in setting MHT; but when cloud adjustments are included there is a potential for greater variation in MHT than he recognized. In terms of W/m^2, the magnitude of cloud adjustments with rotation (Figs. 2.7c, 2.8b), are comparable to, or exceed, the magnitude of the climatological ocean heat uptake (e.g., Hartmann, 2015); and so just in energetic terms, cloud variations are arguably more important than ocean transport variations in setting MHT. This is also borne out in a study evaluating the range of MHT among CMIP3 GCMs in modern climatology (Donohoe and Battisti, 2012).

It is worthwhile noting that although we attributed the insensitivity of the MHT to rotation rate to changes in the top-of-atmosphere fluxes, this doesn't mean that dynamics plays no role. On the contrary, dynamics is essential. The changes in clouds that are fundamental to the changes in top-of-atmosphere fluxes are largely determined by changes in the Hadley cell which, as reported in Section 6 are overwhelmingly due to the changing rotation rate.

Our study also suggests that change in $\mathrm{MHT}_{\mathrm{max}}$, if there is any, is most sensitive to changes in the zonal-mean distribution of clouds in the tropics. In speculating about MHT in past climates, this implies that to get a large change in $\mathrm{MHT}_{\mathrm{max}}$ one has to change the tropics dramatically, for example, by moving land into the tropics (such as the Pangea during the Triassic, perhaps). In this regard, the glacial fluctuations of the Pleistocene have primarily involved changes in the high latitudes, and so one wouldn't expect much change

in its $\mathrm{MHT}_{\max}$.

Chapter 3

SOUTH AMERICAN CLIMATE DURING THE EARLY EOCENE: IMPACT OF A NARROWER ATLANTIC AND HIGHER ATMOSPHERIC CO_2

3.1 Introduction

The deep-sea $\delta^{18}O$ record indicates that the early Eocene (∼55 Ma) was the warmest period of the Earth in the past 65 million years (Zachos et al., 2001). The global mean surface temperature is estimated to be 4 to 5°C greater than today (Jones et al., 2011), with the median SST about 30°C in the tropics, ∼22°C in the Northern Hemisphere high latitudes, and 18°C in the Southern Hemisphere high latitudes (see Fig.2 of Hollis et al. (2012) for a summary of the proxy records). The warm Eocene is a likely result of higher atmospheric CO_2 and possibly the disposition of continental geometry. Compared to today, the early Eocene is characterized by a narrower Atlantic basin, a narrower and shallower Drake passage, a more southward position of Australia, an open Panama seaway, land connections between North America and Europe through Greenland, an India isolated from Asia (Seton et al., 2012), and a much higher CO_2 concentration in the atmosphere. The atmospheric CO_2 concentration is believed to have been about four times of the pre-industrial value (Beerling and Royer, 2011).

Pollen data from Colombia and Venezuela (Jaramillo et al., 2006) and from Patagonia (Wilf et al., 2005) suggest that the biodiversity of northern tropical South America rainforest was very high during the early Eocene, exceeding values of modern-day, despite the greater global mean surface temperature and greater CO_2 concentration. We are involved in a large study to evaluate Haffer's (1969) hypothesis that the high biodiversity of the western Amazon is primarily due to the rise of the Andes prior to the Eocene, fracturing the landscape and

altering climate in such as way that promoted extraordinary allopatric specification, resulting in high biodiversity. If Haffer's hypothesis is true, understanding the high biodiversity of tropical South America during the early Eocene may provide insight for future biodiversity changes in the Amazon due to anthropogenic change in CO_2 and climate. Our interest here is to determine how the climate in tropical South America during the early Eocene was different from today's climate and to understand the underlying dynamics of the changes in climate between early Eocene and modern day.

The high biodiversity during early Eocene as indicated by the pollen data is thought to be due to (in part) a humid climate in tropical South America (Jaramillo et al., 2006), but proxy records that are old enough to resolve early Eocene climate in tropical South America are sparse. Many studies have explored the global climate of the early Eocene using numerical models (Huber and Sloan, 2001; Huber et al., 2004; Heinemann et al., 2009; Lunt et al., 2010; Winguth et al., 2010; Huber and Caballero, 2011). However, there is no consensus among modeling studies on what South American precipitation in early Eocene was like (Carmichael et al., 2016). Also, in each of these studies, the goal was to reproduce the climate of the early Eocene using realistic boundary conditions and forcings. Hence, these studies do not isolate the myriad different forcings from the profound geometry changes to determine which forcings and geometry changes are responsible for regional scale climate changes in the early Eocene.

For the purpose of understanding the climate of tropical South America during the early Eocene, two factors are likely to be paramount: the narrower Atlantic and the higher greenhouse gases concentration. While other changes in geometry and changes in other boundary conditions (i.e., the opening of Panama seaway, the narrowing and shallowing of Drake passage, and the change in ocean circulation) may be important for the early Eocene climate in other places of the world, these two factors are likely to be the dominant changes that impact the climate of tropical South America during the early Eocene (see discussion).

In this study, we use semi-idealized GCM simulations to isolate the impacts of the narrower Atlantic Ocean and the high CO_2 concentration on the climate of tropical South

America, allowing a dynamical interpretation of the effects of these two factors during the geological past. Our results show that the high CO_2 concentration generally causes increased precipitation, while the narrow Atlantic generally causes an even greater drying, resulting in a drier climate over tropical South America during the early Eocene, compared to the modern climate. The competing effects of drying from Atlantic narrowing, and wetting from increased CO_2, may help explain why models disagree on the sign of the change in this region (e.g. CCSM3 in Huber and Caballero (2011) vs. ECHAM 5 in Heinemann et al. (2009); also cf. Figs. 1 and 3 of Carmichael et al. (2016)): models in which precipitation is more sensitive to CO_2 are more likely to show wetting overall.

3.2 Model and Experimental Design

We use the ECHAM atmospheric general circulation model, version 4.6 (ECHAM4.6; Roeckner, 1996), in this study. The ECHAM model is a spectral model with T42 resolution (approximately 2.8° in latitude and longitude) with 19 vertical levels, and is coupled to a 50-m slab ocean. We first perform a modern-day experiment (called "Wide_353CO2"), whereby the model is configured with present-day continental geometry, orography, and orbital parameters; and with an atmospheric CO_2 concentration of 353 ppm, and other greenhouse gas concentrations and aerosol distributions from 1850 (Table 3.1). A climatological Q-flux with seasonal cycle is prescribed to the slab ocean in the modern-day simulation to account for the ocean heat flux convergence by ocean currents and for biases in the surface heat flux due to biases in the atmospheric model. Using ECHAM 4.6 coupled to a slab ocean does not allow for changes in the ocean circulation. The possible effects of ocean circulation change are explored in section 3.4.

Although there are myriad geometry and forcing differences that may be important for early Eocene climate in other regions of the world, we are interested in the climate of tropical South America. Hence we isolate the impact of the two changes that are likely to be most important there: a narrower Atlantic Ocean and the higher atmospheric CO_2 concentration. So we perform the *Narrow_1000CO2* experiment, in which the atmospheric CO_2

Table 3.1: Experiments performed in this study.

Experiments	Wide_353CO2 ("modern day")	Narrow_1000CO2 ("early Eocene")	Wide_1000CO2	Narrow_353CO2
continental geometry	Modern	Narrow Atlantic	Modern	Narrow Atlantic
CO_2 concentration	353 ppm	1000 ppm	1000 ppm	353 ppm
other boundary conditions	pre-industrial	pre-industrial	pre-industrial	pre-industrial

concentration is set at 1000 ppm, the upper range of estimates of CO_2 concentration at the early Eocene reconstructed from proxy data (Beerling and Royer, 2011), and the Atlantic Ocean is narrowed by removing a 25° longitude strip from the Atlantic ocean, while the Pacific Ocean is stretched by 25° longitude. The resulting "narrow Atlantic" is close to the reconstructed Atlantic geometry in the early Eocene (Seton et al., 2012). The Q-flux used in the Narrow_1000CO2 experiment is the same as that in the modern-day experiment, except that it is zonally symmetrized in the Atlantic Basin and uniformly, zonally stretched in the Pacific; a small longitudinally invariant correction is then added to the Q-flux so that the zonally integrated ocean heat flux at each latitude is identical to that in the modern-day experiment (see discussion in section 3.4). We also refer to the Narrow_1000CO2 experiment as the "*Early Eocene*" experiment.

To isolate the impact of a narrower Atlantic basin and the impact of higher atmospheric CO_2 on precipitation and temperature, we perform two further experiments: *Wide_1000CO2* is the same as the modern-day experiment except that the atmospheric CO_2 concentration is set to be 1000 ppm; and *Narrow_353CO2* is the same as Narrow_1000CO2 except for a 353 ppm CO_2 concentration. Differences between Wide_1000CO2 and Narrow_1000CO2, or between Wide_353CO2 and Narrow_353CO2 show the effect of narrowing the Atlantic alone in a 1000 ppm and 353 ppm CO_2 world, respectively. Differences between Wide_1000CO2 and modern-day experiment, or between Narrow_1000CO2 and Narrow_353CO2 show the

effect of increasing atmospheric CO_2 concentration alone. All four experiments were repeated using CESM 1.2 instead of ECHAM 4.6; the main conclusions are robust to the choice of models. We focus on the results from the ECHAM 4.6 model which has a better modern-day precipitation climatology in tropical South America than does the modern-day CESM 1.2 simulation.

3.3 Results

3.3.1 Modern-day climate

Figure 3.1 shows the seasonal and annual mean precipitation and 850-hPa winds in observations and the modern-day experiment using ECHAM 4.6. Three major systems define the precipitation of South America (see the review by Garreaud et al., 2009, for more details): the Atlantic intertropical convergence zone (ITCZ), the South American monsoon system (SAMS; Zhou and Lau, 1998; Vera et al., 2006) over the continental South America, and the South Atlantic convergence zone (SACZ). The Atlantic ITCZ is associated with the convergence of trade winds over the ocean from both hemispheres. The Atlantic ITCZ migrates north-south seasonally following the Sun and is responsible for the rainy season of the northeast Brazil in austral autumn (March-April-May), when it reaches its southernmost position. The SAMS-related precipitation also follows the migration of the Sun: it is centered in the northwest South America in austral spring, expanding southward and eastward from austral spring to austral summer, and then retreats to the northwest again from austral summer to austral winter. In austral summer, the SASM brings precipitation to almost the entire tropical South America, reaching as far south as 30°S. The Atlantic SACZ forms due to the convergence of the mid-latitude westerly flow with the northerly flow along the western flank of the South Atlantic anticyclone (Kodama, 1993; Lenters and Cook, 1995; Nogués-Paegle and Mo, 1997); the passage of extratropical transient frontal systems contributes to the southern portion of the SACZ (Garreaud and Wallace, 1998). The SPCZ is present all year, but it is most intense during austral summer when it produces the rainy

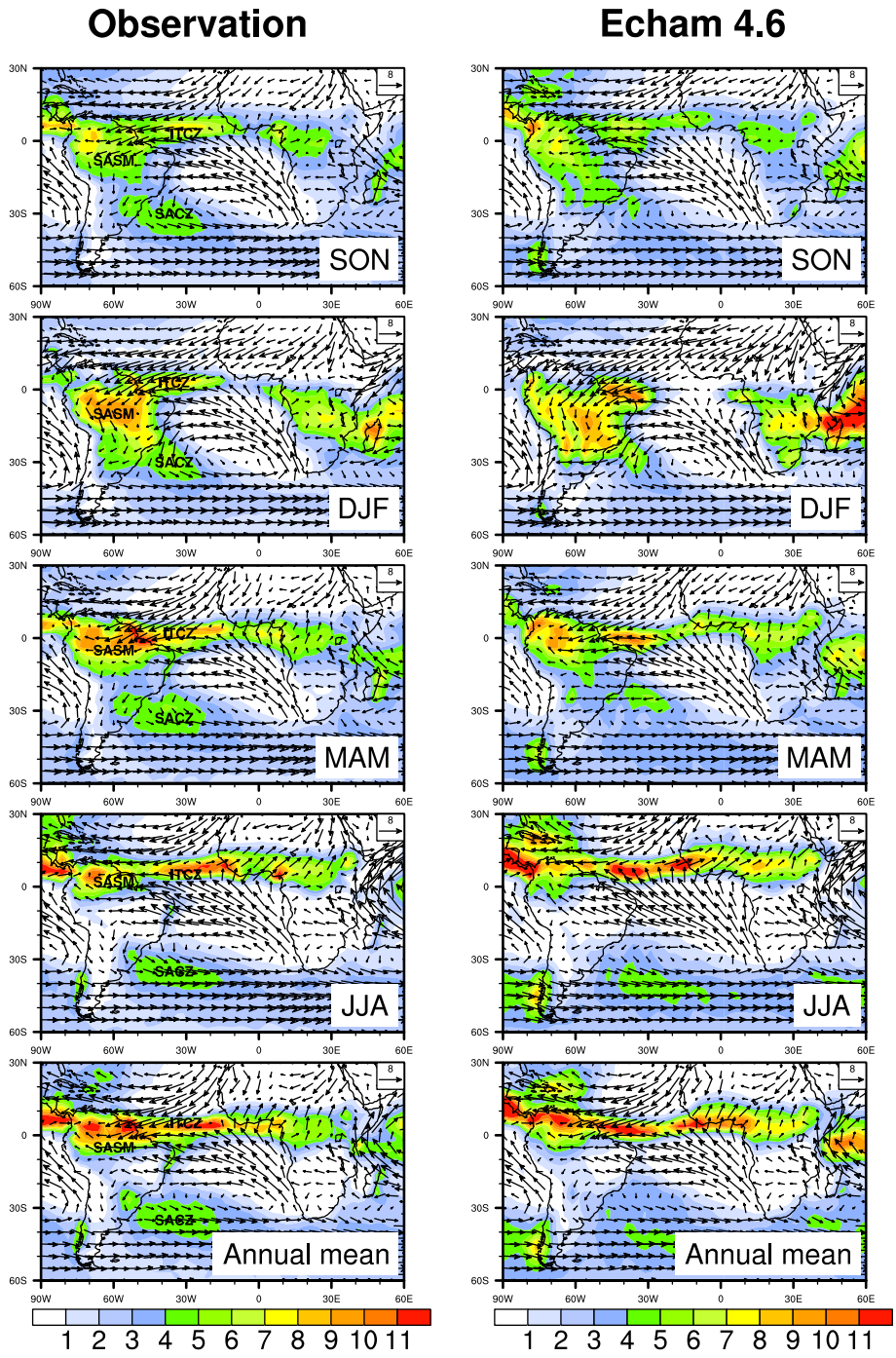

Figure 3.1: The seasonal and annual mean climatological precipitation (shading; mm/day) and 925-hPa winds (vectors; m/s) for (left) observation and (right) from the modern-day simulation using ECHAM4.6 coupled to a slab ocean. Observed precipitation data are from monthly Climate Prediction Center (CPC) Merged Analysis of Precipitation (CMAP; Xie and Arkin 1997) from January 1979 to December 2010, available online at `http://www.esrl.noaa.gov/psd/data/gridded/data.cmap.html`. Observed 850-mb winds are from NCEP2 covering the same period.

season of southeastern Brazil. The major features in the seasonal cycle of the precipitation over tropical South America are fairly well simulated by ECHAM 4.6. This encourages us to use this model as a framework for examining the effect of increasing atmospheric CO_2 and narrowing the Atlantic basin.

3.3.2 Climate of the early Eocene

Figure 3.2 shows the precipitation difference between Narrow_1000CO2 experiment and Wide_353CO2 experiment, representing the difference in the early Eocene climate compared to the modern climate due to the combined impact of increasing atmospheric CO_2 concentration and narrowing of the Atlantic basin. To a first-order approximation, the early Eocene has less annual mean precipitation than today over all of tropical South America. The area- and annually-averaged precipitation over the South American continent decreases by about 15%, from 4.1 mm/day in the modern-day experiment to 3.5 mm/day in the early Eocene experiment (Table 3.2). This drying occurs in most seasons and is strongest in DJF, the rainy season of tropical South America. It occurs in almost every region, except northern tropical South America and along the eastern coast. In northern tropical South America, there is more precipitation in the early Eocene than today in SON and JJA and less than today in the other seasons; along the eastern coast of Brazil, precipitation is enhanced during DJF but reduced during the other seasons. This suggests a change in the seasonality of precipitation in northern tropical South America.

The surface temperature is warmer in the early Eocene than modern day in every season (Fig. 3.3). This result is expected and due to the higher atmospheric CO_2 compared to modern day (not shown).

Figure 3.4 shows the seasonal cycles of precipitation area-averaged over three boxed regions indicated in Fig. 3.2a. These three regions are representative of precipitation of northern South America, central Amazon and the eastern coast. In northern South America today (Box A), the rainy season is from boreal spring to boreal autumn with a peak rainfall in June. This seasonal cycle is in phase with that of Northern Hemisphere summer monsoon

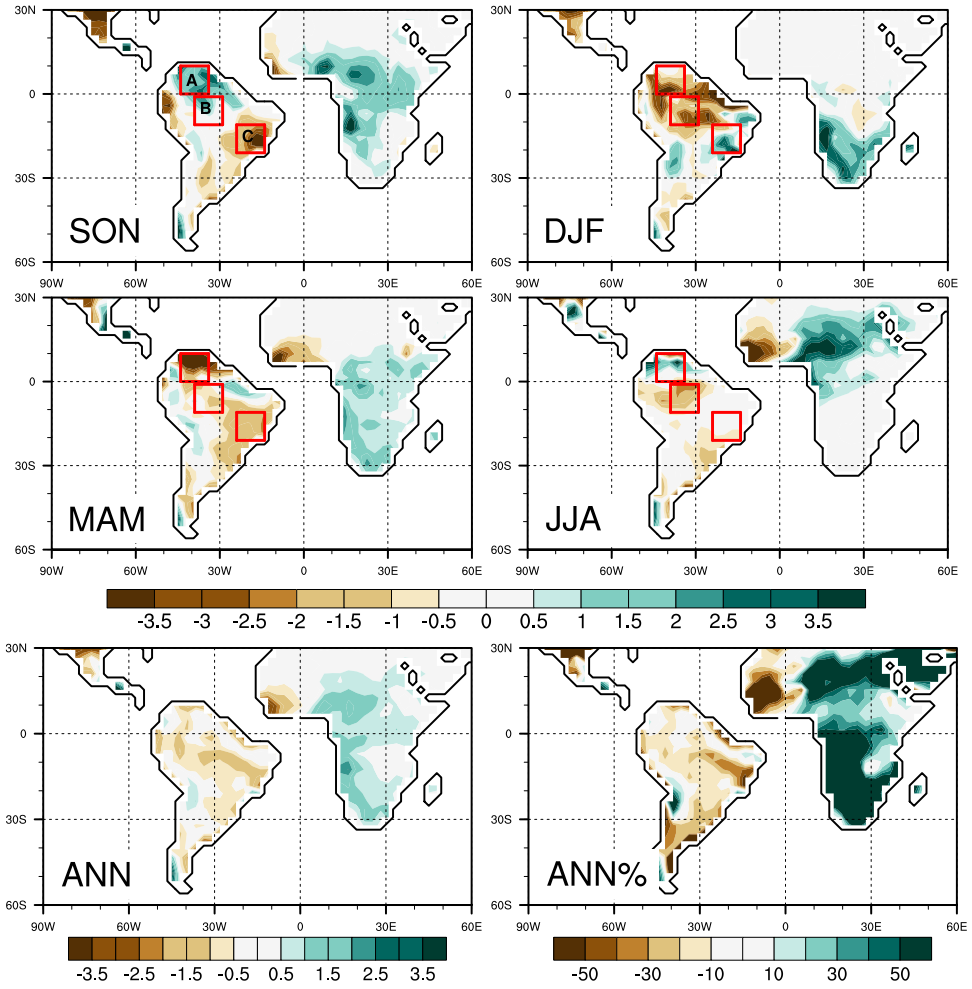

Figure 3.2: The difference in seasonal precipitation (units: mm day^{-1}) due to enhanced CO_2 and a narrower Atlantic (Narrow_1000CO2) compared to that with modern-day geometry and 353 ppm CO_2 (Wide_353CO2). The lower right panel shows the percent change of annual-mean precipitation ((Narrow_1000CO2/Wide_353CO2) - 1) *100). Red boxes represent the regions over which domain averages are examined in Fig. 3.

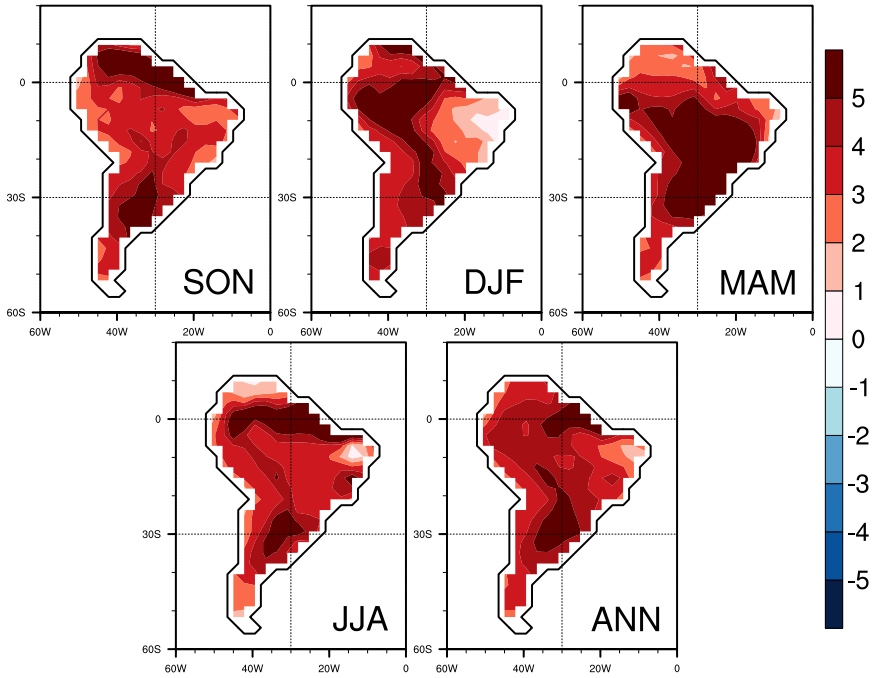

Figure 3.3: The difference in seasonal surface temperature (units: K) due to enhanced CO_2 and a narrower Atlantic (Narrow_1000CO2) compared to that with modern-day geometry and 353 ppm CO_2 (Wide_353CO2).

Table 3.2: Precipitation or change in precipitation area-averaged over South American continent; units: mm day^{-1}.

	DJF	MAM	JJA	SON	Annual
Today	5.5	4.5	2.1	4.3	4.1
Early Eocene	4.5	3.5	1.7	4.0	3.5
Early Eocene minus Today	-1.0	-1.0	-0.4	-0.3	-0.6
Impact of geometry at 1000 ppm (353 ppm)	-1.9(-1.8)	-1.5(-1.0)	-0.6(0.25)	-0.5(0.0)	-1.1(-0.6)
Impact of CO_2 at modern (narrow) Atlantic	0.9(0.8)	0.6(0.1)	0.2(-0.7)	0.2(-0.3)	0.5(0.0)

(e.g. the Asian monsoon). This observed seasonal cycle of precipitation is well captured by the modern-day simulation of ECHAM 4.6 except that the precipitation from June to August is weaker than the observed. During the early Eocene, the rainy season is still from boreal spring to boreal autumn, but the peak rainfall shifts from June in the modern-day experiment to October in the early Eocene (Narrow_1000CO2) experiment. Precipitation during the dry seasons is also weaker in the early Eocene compared to that of modern day.

In the central Amazon (Box B), the rainy season lasts from austral spring to late austral summer, out of phase with precipitation of northern South America. This feature is roughly captured by the modern-day simulation of ECHAM 4.6. Compared to modern day, there is less precipitation in the early Eocene in almost every month except October.

Along the eastern coast (Box C), precipitation occurs from austral spring to autumn with complete dryness from May to August. This feature is almost well reproduced in the modern-day simulation. Compared to modern day, precipitation in the early Eocene is reduced the dry season and increased in the rainy season, resulting in enhanced seasonality in the early Eocene.

For the rest of the chapter, we focus our analysis on the mechanisms responsible for the

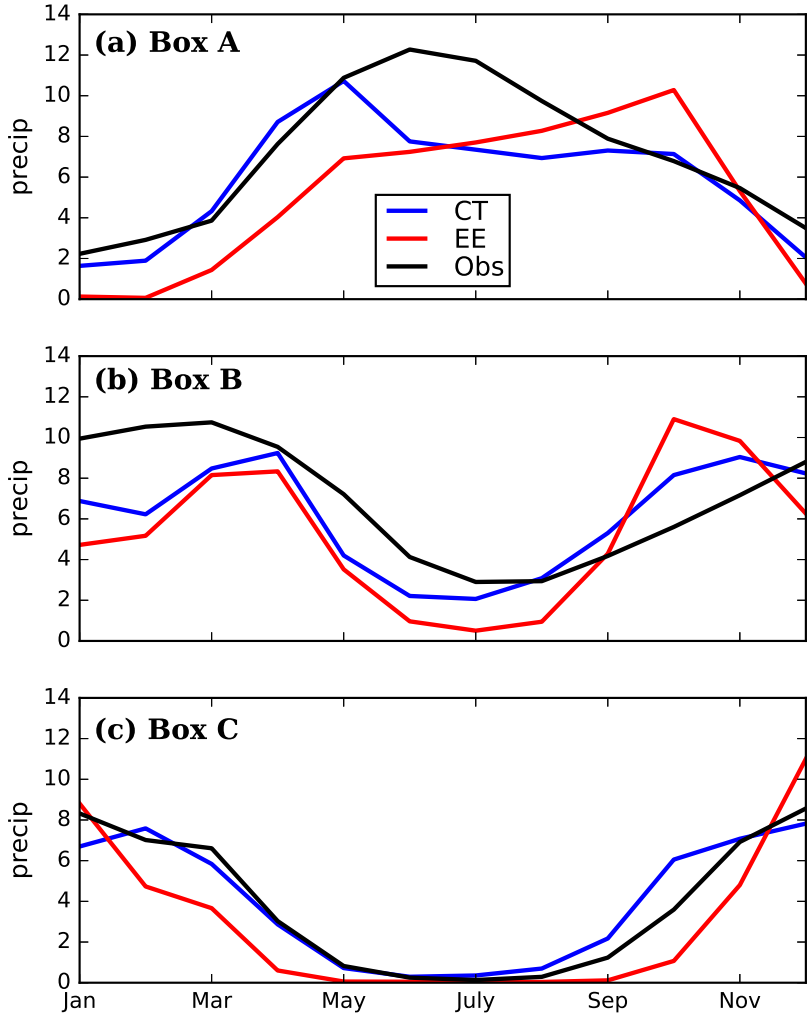

Figure 3.4: Seasonal cycle of precipitation (units: mm day^{-1}) area-averaged over the box regions indicated in Fig. 3.2: observations (black line), from the modern-day simulation today (Wide_353CO2, blue line), and from the early Eocene simulation (Narrow_1000CO2, red line).

precipitation change in DJF. DJF is the rainy season for the entire South America except for the northern tropical South America (north of the equator). It is also representative of the overall drying in the early Eocene (cf. the DJF and annual precipitation changes in Fig. 3.2). We present a brief analysis of the change during SON in section 3.3.4, as SON is unique in a wetting of northern tropical South America during the early Eocene.

Figure 3.5 shows the differences in DJF precipitation between early Eocene and modern climate (top panel), the impact of narrowing the Atlantic basin only (middle panels), and the impact of increasing CO_2 only (bottom panels). Note that precipitation difference in panels b and d (c and e) add up exactly to the precipitation difference shown in the top panel. The drying of tropical South America due to the narrowing of the Atlantic is opposed by the wetting due to increase in CO_2 (see Table 3.2). In modern geometry, increasing atmospheric CO_2 concentration from 353 ppm to 1000 ppm increases the precipitation inland of South America (Fig. 3.5d), enhancing the mean precipitation during DJF (cf. Fig. 3.1). The precipitation response over subtropical South Atlantic due to increased CO_2 is in agreement with the IPCC AR5 models (subtropical South America is the only place on the planet where over where 90% of climate models agree on the sign of the change in precipitation; Stocker, 2014). The precipitation enhancement over the Amazon is consistent with the theoretical understanding of the impact of increasing CO_2: that is, increasing CO_2 warms the ocean and therefore increases evaporation which enhances the lower-tropospheric water vapor and thus enhances the moisture transport into tropical South America (Seager et al., 2010). The enhancement of precipitation due to increased CO_2 is largely independent of Atlantic geometry; it also occurs when the Atlantic is narrower (cf. Figs. 3.5 d, e and Table 3.2). Narrowing the Atlantic decreases DJF precipitation, independent of the atmospheric CO_2 concentration (cf. Figs. 3.5b and c). This effect dominates over increasing CO_2, causing a net drying of tropical South America during the early Eocene. For the rest of the chapter, we will illuminate the process by which the narrowing of the Atlantic decreases the precipitation of South America.

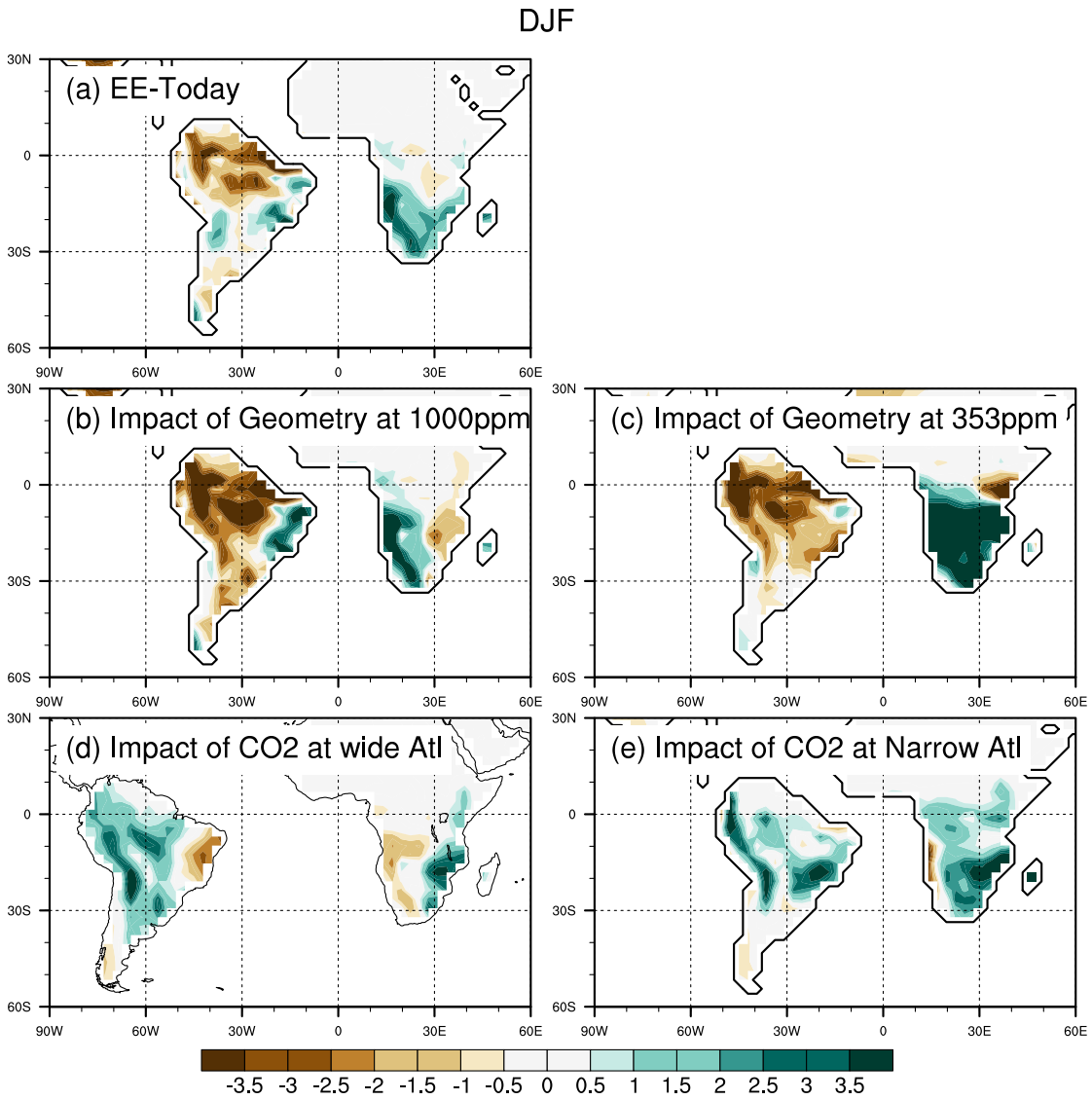

Figure 3.5: Changes in precipitation (units: mm day^{-1}) during DJF. (a) early Eocene minus today (repeated from Fig. 3.2), (b) The impact of geometry at 1000 ppm CO_2 concentration (i.e. Narrow_1000CO2 minus Wide_1000CO2), (c) impact of geometry at 353 ppm (i.e. Narrow_353CO2 minus Wide_353CO2), (d) impact of CO_2 concentration at modern Atlantic geometry (i.e. Wide_1000CO2 minus Wide_353CO2), and (e) impact of CO_2 concentration at narrow Atlantic geometry (i.e. Narrow_1000CO2 minus Narrow_353CO2).

3.3.3 Impact of Narrowing the Atlantic

We study the effect of narrowing the Atlantic by examining the water budget over South America. The equation for the conservation of water can be written as

$$\frac{\partial W}{\partial t} = E - P - \bigtriangledown \cdot \int_0^{P_s} (q\overrightarrow{V}dp) = E - P - \int_0^{P_s} dp \oint q\overrightarrow{V}d\overrightarrow{n}, \tag{3.1}$$

where W is the column-integrated precipitable water vapor, P is precipitation, and E is evaporation. In all the experiments, the tendency of W, $\frac{\partial W}{\partial t}$, is much smaller than the other terms, indicating that W is in steady state. In steady state, the column integrated vapor flux convergence over South America equals precipitation minus evaporation. We use monthly climatology data to calculate vapor flux convergence; as a result, the water budget does not exactly close due to the neglect of sub-monthly covarying anomalies associated with eddies. Nonetheless, the change in the calculated vapor flux convergence qualitatively agrees with what is implied by change in precipitation minus evaporation.

Table 3.3: Changes in DJF precipitation, evaporation, precipitation minus evaporation, and water vapor flux between Narrow_1000CO2 and Wide_1000CO2. All quantities are area-averaged over South America; units: mm day^{-1}.

	ECHAM 4.6	CESM 1.2
Precipitation	-1.87	-1.14
Evaporation	-0.13	-0.19
Precipitation minus Evaporation	-1.74	-0.95
Water vapor convergence	-3.28	-1.15
Water flux across eastern boundary	-0.77	-0.66
Water flux across northeastern boundary	-2.09	-1.12
Water flux across western boundary	-0.80	0.39

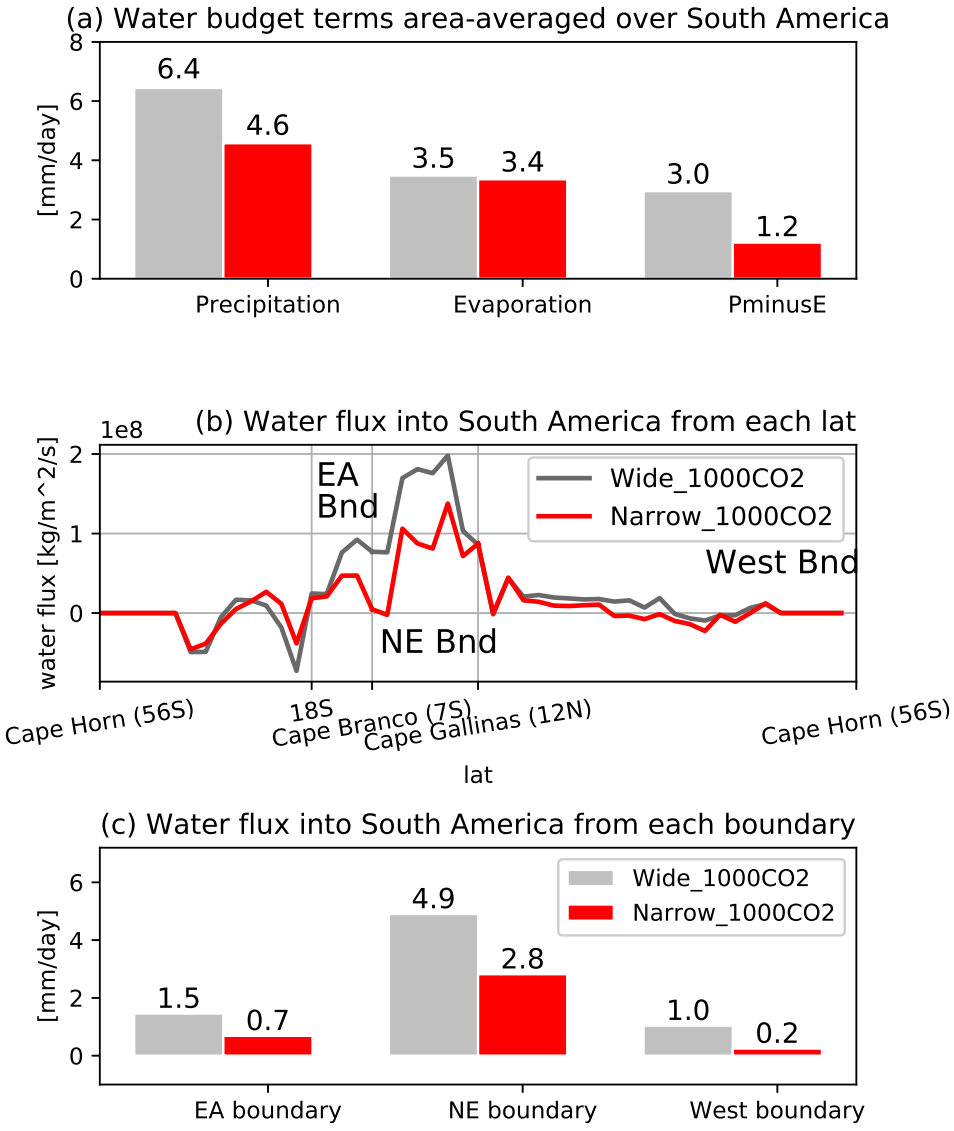

Figure 3.6: Water budget in the Wide_1000CO2 (gray) and the Narrow_1000CO2 (red) experiments. (a) Precipitation, evaporation, and precipitation minus evaporation, all area-averaged over the entire South American continent. All quantities are converted to be in the units of mm day^{-1}. Convergence of water flux is calculated as the sum of water flux into South America across all boundaries shown in panel (b). (b) Vertically integrated water vapor flux into South America across each boundary (units: kg m^{-2} s^{-1}) as a function of latitude (see text). (c) Total water flux into South America across each boundary, converted to be in the units of mm day^{-1} by dividing the sum by the area of South America.

Figure 3.6a shows the precipitation, evaporation, and precipitation minus evaporation in Wide_1000CO2 and Narrow_1000CO2 experiments; all fields are area-averaged over the South American continent and expressed in units of mm/day. Hence, precipitation minus evaporation represents the convergence of water vapor fluxed into South America due to circulation. The area-averaged precipitation decreases by by 30% due to a narrowing of the Atlantic, from 6.4 mm/day in the modern-day geometry experiment to 4.5 mm/day in the narrow Atlantic experiment, both with 1000 ppm CO_2. This change is almost exclusively due to change in the convergence of water flux over South America: the area-averaged water vapor flux convergence decreases by 1.7 mm/day (as implied by the change of precipitation minus evaporation) whereas the evaporation decreases by only 0.2 mm/day. This result is in qualitative agreement with results from the identical experiments using CESM 1.2 model which includes contributions due to transients and so the water budget is almost exactly closed (Table 3.3).

Figure 3.6b shows the contribution to the area-averaged water vapor convergence into South America due to flow across each boundary. Note that the x-axis in Fig. 3.6b starts in the farthest south and goes northward along the eastern boundary of South America. It continues northwestward to the northern tip of tropical South America, Cape Gallinas at 12°N, and then goes southward along the western boundary to Cape Horn. The decrease in water fluxed into South America is mainly due to a reduction in water transported into South America across the northeastern and the eastern boundaries of tropical South America (Fig. 3.6b; note that our eastern boundary and northeastern boundary are defined as from 18°S to 7°S and from 7°S to 12°N, respectively: sections in which water vapor is fluxed *towards* South America). The decrease in water flux across these two boundaries accounts for about 80% of the total decrease in water vapor delivered to South America in the early Eocene compared to modern climate (Fig. 3.6c), most of which is due to a decrease in the water transported across the northeastern boundary (Fig. 3.6c). There is also a small negative contribution to water vapor convergence from the western boundary (Fig. 3.6b), but this result is model dependent – difference in the same pair of experiments using CESM 1.2

features a weak increase in the water flux *into* South America across the western boundary when the Atlantic is narrowed, opposite to what is shown in ECHAM model (see also Table 3.3).

To determine why the water flux across the northeastern and eastern boundaries decreases when the Atlantic is narrowed, we calculated the water vapor that is accumulated by an air parcel that follows the climatological trajectory, starting from Africa and crossing the Atlantic to South America (Fig. 3.7). Specifically, we calculate the total water vapor that enters the boundary layer on its passage from the eastern Atlantic to South America

$$q(\boldsymbol{x}_f) = q(\boldsymbol{x}_0) + \int_{t_0}^{t_f} E(\boldsymbol{s}, t) d\boldsymbol{s}, \tag{3.2}$$

where $E(\boldsymbol{s}, t)$ is evaporation, $q(\boldsymbol{x}_0)$ is the amount of water vapor in the air parcel when it leaves Africa and South Atlantic Ocean, $\boldsymbol{s}$ is the location of air parcels at time t, which is a function of its initial location $\boldsymbol{x}_0$ and wind $\boldsymbol{v}$:

$$\boldsymbol{s} = \boldsymbol{x}_0 + \int_{t_0}^{t} \boldsymbol{v} dt. \tag{3.3}$$

The solution to this equation represents the upper limit of the total water vapor in the air column, assuming zero initial moisture content. We take $\boldsymbol{v}$ to be the wind velocity at 925 hPa which is representative of flow at the boundary layer. We also neglect the negligible amount of water vapor the air parcels initially contain when they leave Africa and South Atlantic Ocean, i.e. $q(\boldsymbol{x}_0) = 0$.

The results of Eqn. 3.2 are shown in Fig. 3.7. Water vapor that flows across the northeastern boundary and condenses over South America is due to evaporation into air parcels that flow across the tropical Atlantic ocean from the western coast of northern Africa. In the modern-day experiment, it takes an air parcel over four days (see Fig. 3.6a) to get from the western coast of Africa to the northeastern coast of South America. The transit time reduces to less than two days in the narrow Atlantic experiment. Therefore the air parcels contain much less vapor when arriving at South America; this is despite an increase in the

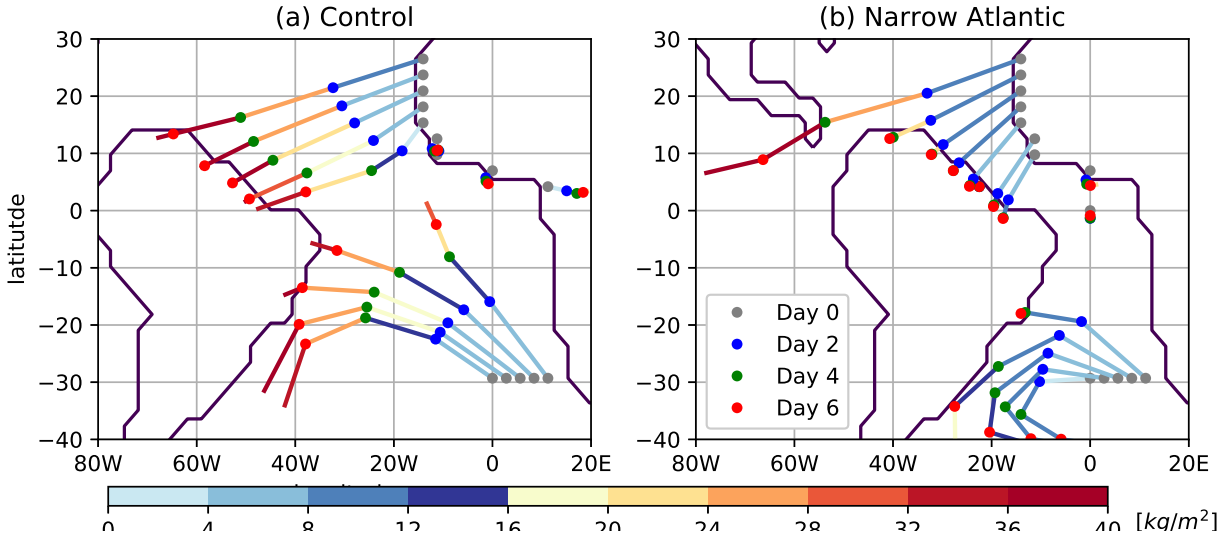

Figure 3.7: Integral of evaporation (units: kg m^{-2}) along the trajectory of climatological DJF 925-hPa winds for (a) the Wide_1000CO2 experiment and (b) Narrow_1000CO2 experiment. Trajectories are terminated when they reach South America.

evaporation rate that air parcels experience during the first two days in the narrow Atlantic experiment compared with the modern-day experiment.

Unlike the air coming across the northeastern boundary, the decrease in water flux across the eastern boundary is due to both the shorter distance travelled over ocean (shorter fetch) and weaker evaporation, with the dominant contribution from the smaller fetch which is a direct result of a narrower Atlantic. When the Atlantic is narrower, it takes air parcels that start from the eastern South Atlantic Ocean four days to reach the eastern coast of South America, two days fewer than when the Atlantic is like modern-day.

3.3.4 Precipitation change during SON

Different from DJF, in SON precipitation is enhanced in the early Eocene experiment in northern South America and reduced elsewhere (Fig. 3.8a). In a gross sense, this precipitation change is mainly caused by narrowing the Atlantic (cf. Figs. 3.8b and c with Fig. 3.8a). However, it is not due to a change in the water vapor flux; just as in DJF, in SON the net

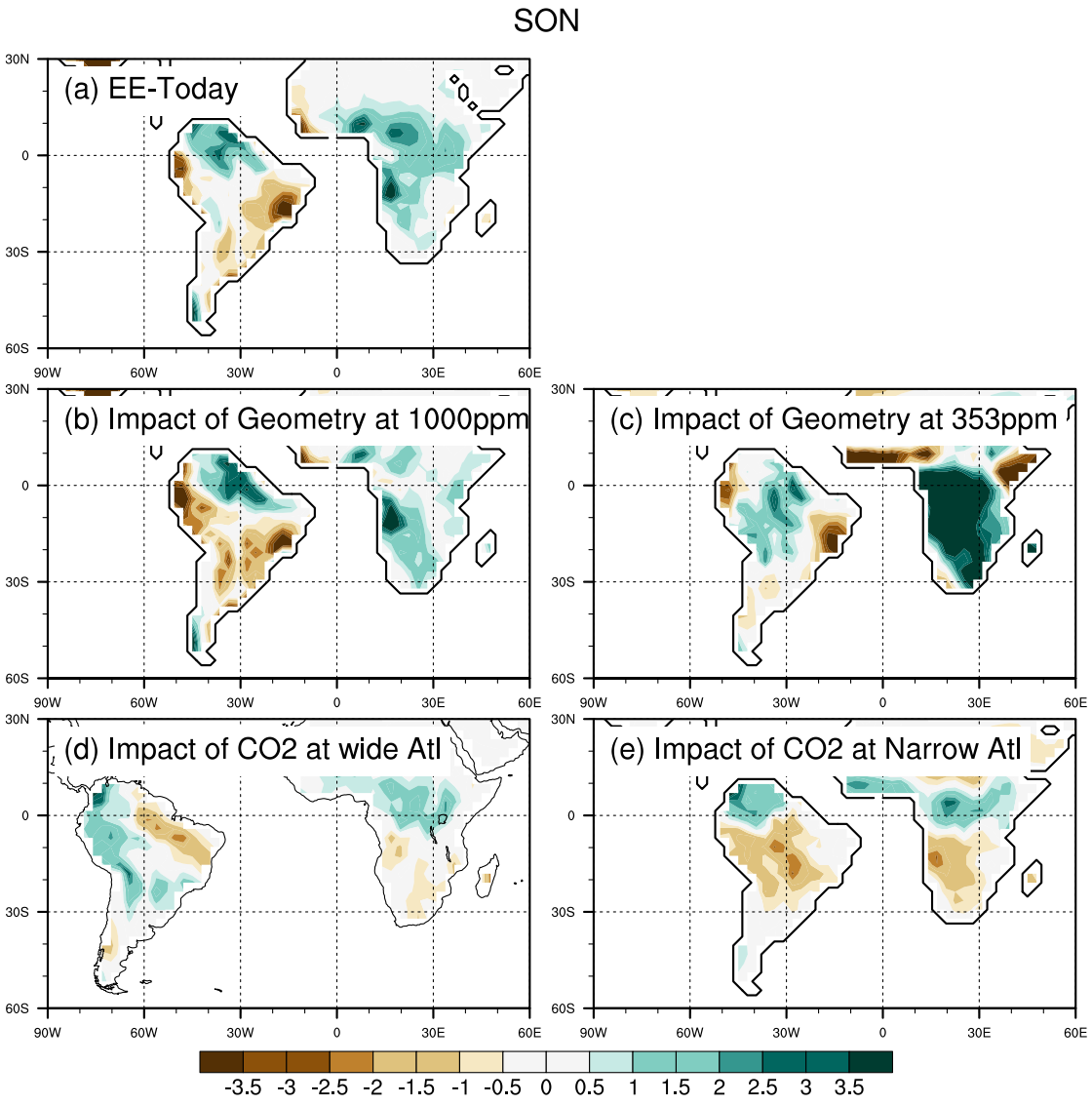

Figure 3.8: As in Fig. 3.5, but for SON.

water vapor flux into South America decreases when the Atlantic is narrower (not shown). Instead, the precipitation increase in northern tropical South America is due to a change in the Atlantic ITCZ. Under modern-day geometry, precipitation in SON occurs mainly in northwestern tropical South America, i.e., Colombia, Ecuador, northern Peru and western Brazil during SON (Fig. 3.9a). Northern Brazil is relative dry because it is located south of the Atlantic ITCZ, in a region of sinking air (Fig. 3.9c). When the Atlantic is narrowed, the ITCZ disappears (cf. Figs. 3.9a and c) and thus the sinking region over northern Brazil weakens and the precipitation in northern South America expands eastward (Figs. 3.9b,d). It is worth noting that the impact of narrowing the Atlantic depends weakly on the ambient atmospheric CO_2 concentration (cf. Figs. 3.8a,b and Table 3.2).

Increasing atmospheric CO_2 changes the precipitation of South America slightly differently in SON than in DJF (cf. Figs. 3.8c,d and Figs. 3.5c,d). Under modern-day geometry, precipitation is enhanced in far western Amazonia (Colombia, Ecuador, and along the Andes) when the CO_2 is increased from 353 to 1000 ppm, but it is decreased elsewhere. The region of precipitation enhancement colocates with that of mean SON precipitation of the modern-day experiment, suggesting the "rich-get-richer" mechanism (Seager et al., 2010) increases the precipitation. In a narrow Atlantic geometry, however, increasing the atmospheric CO_2 concentration increases precipitation in northern South America, but decreases the precipitation in the central Amazon. It is not clear to us why the precipitation response to increasing CO_2 depends on the Atlantic geometry. What is more interesting is that the effects of increasing CO_2 always opposes that of narrowing of the Atlantic (Table 3.2).

3.4 Discussion

Water budget analysis of tropical South America shows that precipitation is reduced when the Atlantic is narrowed – mainly due to the reduction in the import of water vapor across the northeastern and eastern boundaries of South America which, in turn, is due to a reduction in the amount of water picked up from the ocean by air traveling eastward across the Atlantic; it is not due to changes in atmospheric circulation. In fact, there is no

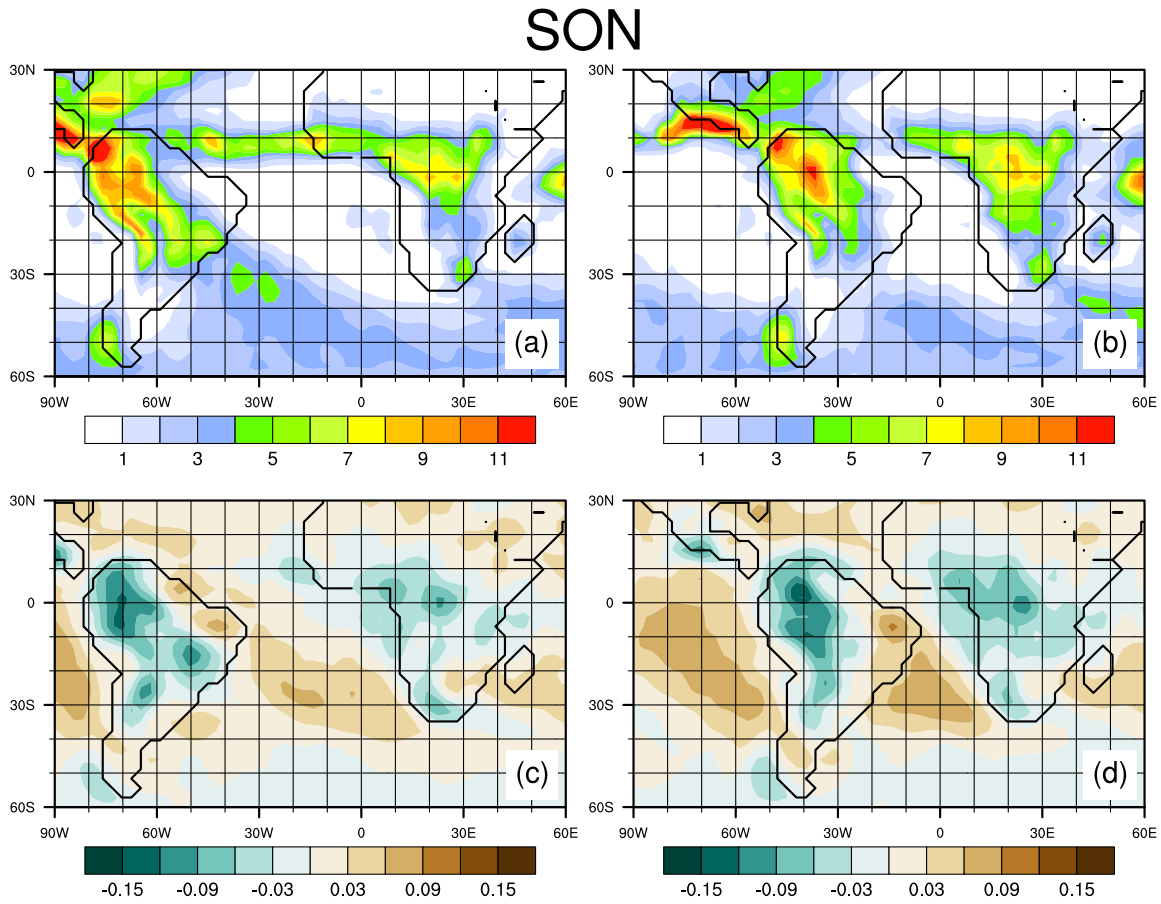

Figure 3.9: Precipitation (shading; mm/day) during SON from (a) "Wide_1000CO2" experiment and (b) "Narrow_1000CO2" experiment. c and d are the same as a and b, respectively, but for vertical velocity at 500-hPa (shading; Pa/s).

dramatic atmospheric circulation change around South America even though the Atlantic Ocean is shrunk to less than half its modern width.

By using ECHAM 4.6 coupled to a slab ocean, this study does not allow for changes in ocean circulation that would arise in a narrower Atlantic. To explore whether changes in ocean circulation might be important for changes in precipitation, we performed a sensitivity experiment in which we re-did the Narrow_1000CO2 experiment but set the Q-flux in the tropical Atlantic to zero. Although setting Q-flux to zero is arbitrary, it is also a draconian change that likely provides a speculation on the amplitude of precipitation change that might be caused by changes in Atlantic ocean circulation. Figure 3.10 shows the precipitation changes for this experiment. A large (but arbitrary) change in "ocean circulation" has a negligible effect on precipitation in tropical South American precipitation compared to that of increasing CO_2 and narrowing the Atlantic basin.

To explore whether the primary results are model dependent, we repeated all the experiments with CESM 1.2 and found qualitatively similar results: a drier early Eocene compared to the modern climate, with the drying effects of narrowing the Atlantic overwhelming the wetting effects of increasing the atmospheric CO_2. Both ECHAM 4.6 and CESM 1.2 show that narrowing the Atlantic dries tropical South America, and that the drying is due to a decrease in water vapor flux into South America across the northeast boundary (Table 3.2) which is due to a decrease in the fetch over which the air travels before crossing the coastline.

3.5 Conclusion

Proxy records show that climate during the early Eocene is very different from modern day. In this study, we examined the impact of changes in two boundary conditions that are likely to be most important for tropical South American climate during the early Eocene: a higher atmospheric CO_2 concentration and a narrower Atlantic basin. As seen in both ECHAM 4.6 and CESM 1.2 coupled to a slab ocean, narrowing the Atlantic alone decreases the precipitation of South America, whereas increasing atmospheric CO_2 alone tends to increase the precipitation. The net impact of these two is to dry the tropical South America.

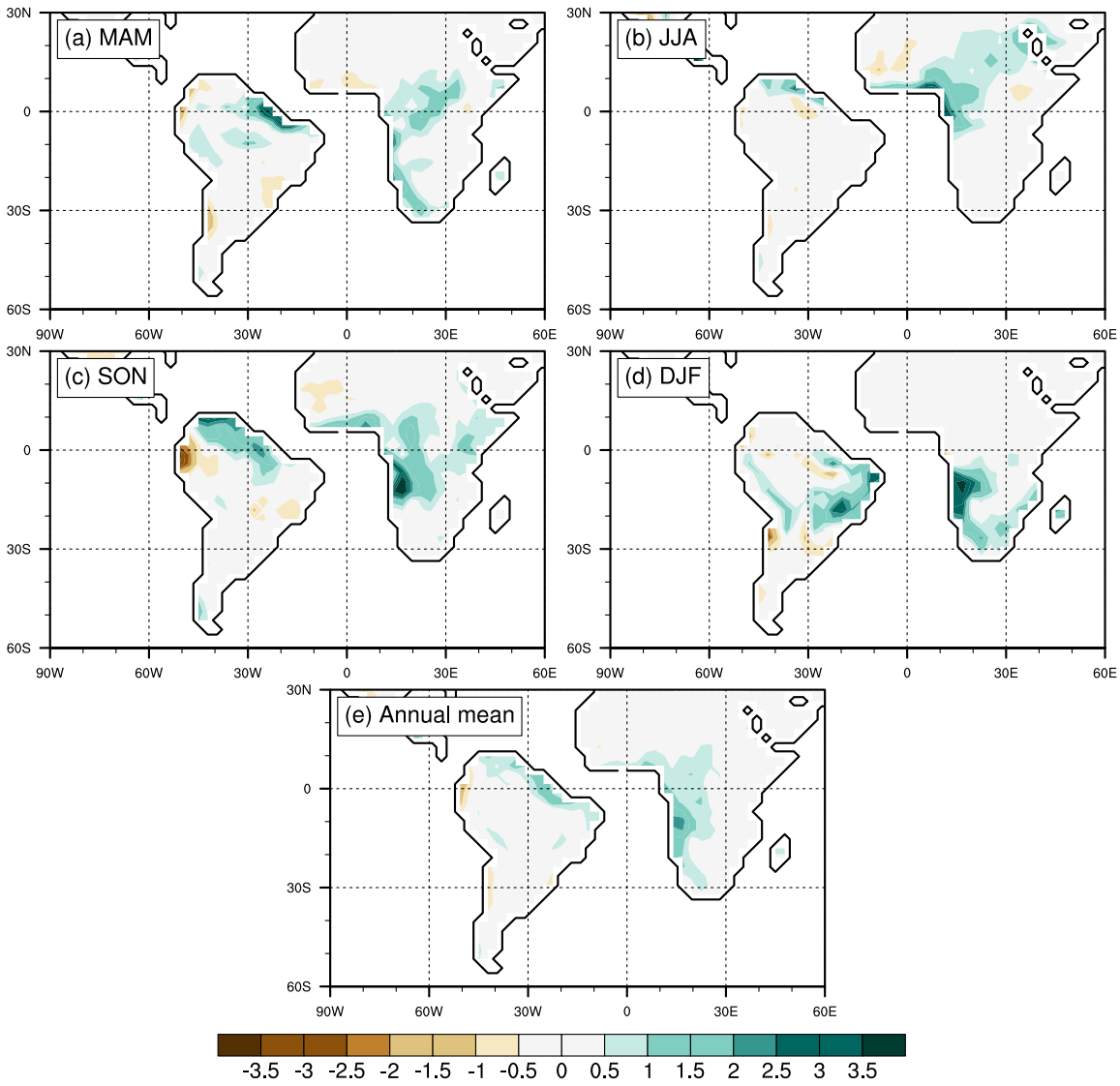

Figure 3.10: Differences of precipitation (units: mm day^{-1}) in the "early Eocene" due to draconian change in "ocean circulation"; that is, Narrow_1000CO2 minus Narrow_1000CO2 with Q-flux = 0. Changes over ocean are not shown.

An analysis of the water budget shows that the drying of tropical South America under a narrower Atlantic geometry is due to a reduction in the water vapor transported into South America across the northeastern and eastern boundaries, and not due to changes in the atmospheric circulation. For both narrow and wide Atlantic basins, the water vapor that flows into and condenses over South America is collected as air parcels transit across the tropical Atlantic Ocean. When the Atlantic is narrower, air parcels traveling across the ocean have less time to pick up water from the ocean below; as a result, they contain much less vapor when crossing the coastline of South America.

Chapter 4

TROPICAL PRECIPITATION AND CROSS-EQUATORIAL OCEAN HEAT TRANSPORT DURING THE MID-HOLOCENE

4.1 Introduction

By the time of the mid-Holocene, roughly 6,000 years ago, the large continental ice shelves that occupied much of North America during the last glaciation had retreated to near modern-day extent (Paillard, 2010) and greenhouse gas concentrations were also near modern-day values. Hence, the main driver of climatic differences between the mid-Holocene and present day was differences in Earth's orbit about the Sun: i) the Earth's elliptical orbit about the Sun passed closest to the Sun in late August during the mid-Holocene compared to early January in the present day orbital configuration, resulting in more (less) intense insolation during boreal (austral) summer (Fig. 4 of Bosmans et al., 2012); ii) obliquity was slightly higher during the mid-Holocene, resulting in greater high-latitude (less tropical) insolation compared to modern day. There is ample geological and geochemical evidence that the changes in insolation at the mid-Holocene modulates the climate, especially precipitation in the tropics. The fossil pollen and lake sediments from Africa show that the Sahel and Sahara regions were considerably wetter during the mid-Holocene than at present (Street and Grove, 1976; Jolly et al., 1998; Bartlein et al., 2011). The sediment record from the Cariaco basin suggests that precipitation over the northern tip of South America was enhanced during the mid-Holocene (Haug et al., 2001). Similarly, oxygen isotope records in speleothems around the Indian basin are consistent with a more intense Indian monsoon in the mid-Holocene than at present (LeGrande and Schmidt, 2009). Whether the compilation of these records suggest an intensification of the Northern Hemisphere summer monsoons systems (Boos and Korty, 2016) or a more zonally homogenous northward shift/expansion

of the tropical precipitation (Collins et al., 2011a; Arbuszewski et al., 2013) is subject to interpretation.

Numerical modeling studies show that the precipitation response to mid-Holocene orbital changes is zonally asymmetric and seasonally heterogeneous. There is a robust enhancement of the Northern Hemisphere summer monsoon and a weakening of the Southern Hemisphere summer monsoon (Kutzbach and Guetter, 1986; Joussaume et al., 1999; Braconnot et al., 2007a; Prado et al., 2013; Battisti et al., 2014; Liu and Battisti, 2015). Braconnot et al. (2007b) showed that intense tropical precipitation extended farther north during the boreal summer over India, the Sahel and western Africa – with much smaller changes over the ocean (see their Fig. 3b) – in all the mid-Holocene simulations participating in the second phase of the Paleoclimate Modeling Inter-comparison Project (PMIP2). This zonal asymmetry in the precipitation response to mid-Holocene orbital changes is common to almost all simulations of the mid-Holocene no matter whether a slab or a dynamic ocean is used (cf. Figs 4.1a and 4.1b; see also Hsu et al. (2010); Chamales (2014)). It is also present in experiments with more extreme precessional forcing, such as the difference between 11 Kyr BP and modern day, and the difference between 218 and 207 Kyr BP (Clement et al., 2004; Battisti et al., 2014; Liu and Battisti, 2015). By synthesizing the paleoclimate records and results from climate model simulations of the mid-Holocene, McGee et al. (2014) argue that zonal mean precipitation changes were remarkably small (ITCZ shifts could not have exceeded 50 km) and the precipitation changes inferred from mid-Holocene proxy records are primarily regionally and seasonally heterogeneous.

Despite the predominant zonally and seasonally inhomogeneous characteristic of tropical precipitation changes during the mid-Holocene, we demonstrate here that coupled model simulations of the mid-Holocene have a robust northward shift of the annual-mean zonal-mean tropical precipitation (called "mean ITCZ" in the following text for convenience). The majority (9 out of 12) of the phase 3 of the Paleoclimate Modeling Intercomparison Project (PMIP3) models shift the mean ITCZ northward in response to mid-Holocene orbital parameters (see Fig. A2). This is consistent with the findings of Donohoe et al. (2013), who

documented a robust northward mean ITCZ shift in the previous generation (PMIP2) of coupled climate model simulations of the mid-Holocene. A northward ITCZ shift requires anomalous energy input to the atmosphere in the Northern Hemisphere and atmospheric cooling in the Southern Hemisphere (see review by Schneider et al. (2014)). Therefore, the robust northward ITCZ shift in the mid-Holocene seen in the climate models (each of which has a unique physical package) suggests a basic underlying mechanism for the hemispherical asymmetric energy input to the Northern Hemisphere atmosphere due to either changes in radiative processes or ocean dynamics.

While the mean ITCZ shifts northward in the PMIP3 models that feature an atmospheric general circulation model coupled to a dynamic ocean model, it shifts southward when an atmospheric general circulation model is coupled to a slab ocean model. This includes the ECHAM4.6 used in this study (Battisti et al., 2014; Liu and Battisti, 2015) and the CCSM3 (personal communications with Kim Chamales in August, 2013). That the sign of the meridional displacement of mean ITCZ depends on whether the models employ a dynamic ocean provides a fortuitous window for understanding how changes in ocean circulation in response to precessional forcing impact the tropical precipitation.

This paper studies the tropical zonal-mean annual-mean precipitation change in PMIP3 simulations of the mid-Holocene. We take as a starting point that the fundamental precipitation and circulation response to mid-Holocene orbital forcing is the enhancement of the Northern Hemisphere summer monsoon which has been noted extensively in the literature, and that this response is the direct response to the insolation change which does not depend on dynamical coupling to an ocean. We emphasize that, while the mid-Holocene precipitation changes are dominated by this seasonally and zonally inhomogenous response, the focus of this manuscript is how the hemispherically asymmetric changes in monsoon strength impact the zonal mean ITCZ location. We invoke the following mechanism to explain the northward ITCZ shift in coupled climate models and the near-zero ITCZ shift in models without a dynamic ocean (Fig. 4.5): i) the wind stress change due to the enhanced Northern Hemisphere (diminished Southern Hemisphere) summer monsoon increases the circulation of

the northern tropical Pacific Ocean gyre (decreases the circulation of the southern tropical Pacific gyre), bringing energy into the Northern Hemisphere; ii) the Northern Hemisphere atmosphere is heated, resulting in a northward mean ITCZ shift. The latter process can be thought of as resulting from the compensating cross-equatorial energy transport between the ocean and the atmosphere whereby the enhanced northward ocean energy transport across the equator is (partially) balanced by a compensating southward atmospheric energy transport across the equator associated with a northward shifted Hadley cell and mean ITCZ (Frierson et al., 2013). We expand on and elaborate on the mechanisms modulating the mean ITCZ and the central role of changes in the ocean circulation in this manuscript.

4.2 Data and Methods

4.2.1 Model runs used

We make use of the output from PMIP3, wherein the climates of pre-industrial and mid-Holocene were simulated using climate models that include full dynamic ocean module (Braconnot et al., 2012). We analyzed all models for which the requisite output required for the analyses we perform is publicly available; details of the models and references are found in Table 4.1. The major difference between the pre-industrial and the mid-Holocene simulations is insolation: in the mid-Holocene, perihelion is in boreal summer (around August 21)[1], and there is a slightly greater obliquity than today; perihelion in the pre-industrial and modern climate is in boreal winter (around January 3). This leads to an increase of insolation by 21 W m^{-2} at 20°N in the Northern Hemisphere summer (June-July-August) and to a decrease of insolation in the Southern Hemisphere summer (December-January-February) (see Fig. 4 of Bosmans et al. (2012)) during the mid-Holocene compared to today. The change in mean ITCZ is therefore due to both change in precession and change in obliquity, with a dominant contribution from change in precession.

Each simulation used the same boundary conditions for the mid-Holocene and pre-

[1]Vernal equinox is fixed on March 21.

Table 4.1: List of the model names, resolutions and references for the PMIP3 models used in this study. Also shown is the length of the pre-industrial (PI) and the mid-Holocene (6ka) simulations. When there was an ensemble of runs for an experiment, climatologies were calculated using the first ensemble member.

		Resolution			Length of run (years)	
Model name	Institution	Atmos. Lat × Long Level	Ocn Lat × Long Level	Reference	PI	6ka
1-BCC-CSM1.1 (BCC-CSM1.1);	Bejing Climate Center, China Meteorological Administration	T42 L26	232×360 L40	Xin et al. (2013)	500	100
2-CCSM4	National Center for Atmospheric Research, United States	0.9°×1.25°L26	384×320 L60	Gent et al. (2011)	1050	300
3-CNRM-CM5	Center National de Recherches Météorologiques, France	T127 L31	292×362 L42	Voldoire et al. (2013)	850	200
4-CSIRO-Mk3.6.0 Center of Excellence, Australia	Commonwealth Scientific and Industrial Research Organization in collaboration with the Queensland Climate Change	T63 L18	189×192 L31	Rotstayn et al. (2010)	500	100
5-CSIRO-Mk3L.1.2	University of New South Wales, Sydney, Australia	R21 L18	122×128 L21	Phipps et al. (2011)	1000	500
6-FGOALS-g2 Sciences; and CESS, Tsinghua University, China	LASG, Institute of Atmospheric Physics, Chinese Academy of	2.81°×2.81°L26	196×360 L30	Li et al. (2013)	700	685
7-FGOALS-s2 Sciences	LASG, Institute of Atmospheric Physics, Chinese Academy of	T42 L26	196×360 L30	Bao et al. (2013)	500	100
8-GISS-E2-R	NASA Goddard Institute for Space Studies	2°×2.5°L20	180×288 L32	Schmidt et al. (2006)	1200	100
9-MIROC-ESM Japan	Japan Agency for Marine-Earth Science and Technology, Atmosphere and Ocean Research Institute (The University of Tokyo), and National Institute for Environmental Studies,	T42 L80	192×256 L44	Watanabe et al. (2011)	630	100
10-MRI-CGCM3	Meteorological Research Institute, Japan	T159 L48	368×360 L51	Yukimoto et al. (2012)	500	100
11-HadGEM2-ES	Met Office Hadley Centre, United Kingdom	1.875°×1.25°L38	NA	Collins et al. (2011b); Jones et al. (2011); Bellouin et al. (2011)	577	100
12-MPI-ESM-P	Max Planck Institute for Meteorology, Germany	T63 L47	220×256 L40	Raddatz et al. (2007); Marsland et al. (2003)	1155	100

industrial simulations: ice sheet geometry, topography and greenhouse gas concentrations – except for CH_4 concentration, which is reduced from 760 ppb in the pre-industrial simulation to 650 ppb in the mid-Holocene simulation (Taylor et al., 2012; https://pmip3.lsce.ipsl.fr). The resulting difference in radiative forcing due to changes in CH_4 is negligible compared to the orbitally induced changes in insolation. We use the monthly climatological data downloaded from the CMIP5 data portal (http://cmip-pcmdi.llnl.gov/cmip5/data_portal.html).

4.2.2 Energetic Analysis

The position of mean ITCZ is closely linked to the cross-equatorial energy transport by the atmosphere, with a northward displacement of the mean ITCZ corresponding to a southward atmospheric energy transport across the equator because the meridional transport of moisture, sensible heat, and potential energy in the deep tropics is primarily accomplished by the Hadley Circulation. Thus, understanding changes in the position of mean ITCZ is synonymous with understanding the changes in inter-hemispheric energy transport and the energetic processes that lead to such changes. In equilibrium, divergence of the atmospheric energy transport $\nabla \cdot \mathrm{AHT}$ is balanced by the net input energy to the atmosphere $\mathrm{F_{net}}$:

$$\nabla \cdot AHT = F_{TOA} + F_{SFC} \equiv F_{net} \quad , \tag{4.1}$$

where $\mathrm{F_{TOA}}$ is the net radiation at the top of the atmosphere, and $\mathrm{F_{SFC}}$ is the net heat flux entering the atmosphere from the surface. The northward atmospheric energy transport across a latitude band $\mathrm{AHT}(\phi)$ can then be calculated by integrating Eq. (4.1) as follows:

$$AHT(\phi) = R^2 \int_{-\pi/2}^{\phi} \int_{0}^{2\pi} F_{net}\, cos\phi\, d\lambda d\phi \quad , \tag{4.2}$$

where R is the radius of the Earth, and $F_{net} = F_{TOA} + F_{SFC}$ is a function of latitude ϕ and longitude λ. The cross-equatorial atmospheric energy transport $AHT(EQ) \equiv AHT(\phi = 0)$ can be expressed as either the integral of the net energy into the atmosphere from the South Pole to the Equator or from the Equator to the North Pole as follows:

$$AHT(EQ) = R^2 \int_{-\pi/2}^{0} \int_{0}^{2\pi} F_{net}\, cos\phi\, d\lambda d\phi \tag{4.3}$$

$$= -R^2 \int_0^{\pi/2} \int_0^{2\pi} F_{net}\, cos\phi\, d\lambda d\phi \quad , \tag{4.4}$$

which can also be written as

$$AHT(EQ) = -\frac{1}{2}\left([F_{net}] \Big|_{SH}^{NH} \right) = -\frac{1}{2}\left([F_{TOA} + F_{SFC}] \Big|_{SH}^{NH} \right) \quad , \tag{4.5}$$

where [.] denotes the integral over the hemisphere. Eq. (4.5) states that the hemispheric asymmetry in net energy into the atmosphere is balanced by atmospheric energy transport across the equator from the hemisphere receiving excess energy to the hemisphere with a net energy loss. The AHT(EQ) is equal to the asymmetry in hemispherically integrated F_{net}, which, in turn, is due to the hemispheric asymmetry in F_{TOA}, F_{SFC} or both.

4.3 Results

4.3.1 Changes in precipitation at the mid-Holocene

Figure 4.1a shows the multi-model-mean change (hereafter we define change as mid-Holocene minus pre-industrial) in the precipitation between the mid-Holocene and the pre-industrial simulations from the PMIP3 models. Figure 4.1b shows the same change, but from the ECHAM4.6 model coupled to a 50 m slab ocean. The dominant features in the model with the slab ocean and in the models with a dynamical ocean are the shifts in precipitation from the ocean to the land in the Northern Hemisphere and from the land to the ocean in the Southern Hemisphere. This land-sea asymmetry is also seen in other modeling studies (Kutzbach and Guetter, 1986; Clement et al., 2004; Braconnot et al., 2007a; Hsu et al., 2010), including those associated with stronger precessional cycles (Bartlein et al., 2011; Battisti et al., 2014; Liu and Battisti, 2015): the stronger Northern Hemisphere summer insolation in the mid-Holocene shifts the location of the maximum moist entropy from the Bay of Bengal and Southeast Asia to be over northern India and the Arabian Peninsula (Battisti et al., 2014); similarly, the reduced summer (December-January-Feburary) insolation over South America and southern Africa in the mid-Holocene reduces moist entropy and thus precipitation in these regions compared to that over the adjacent oceans (Liu and Battisti,

2015). Note that change in the mutli-model-mean precipitation in the PMIP3 models is not as strong as that in the ECHAM4.6-slab ocean model because averaging over all models partly smoothes out the signal and – unlike the circulation changes (see section 4.34.3.3) – details in spatial pattern of the precipitation change can differ substantially from the multi-model mean in some models.

It is worth mentioning that the change in precipitation in the mid-Holocene compared to pre-industrial also features a northward shift of ITCZ over the land in the boreal summer and a southward shift of ITCZ over the ocean in austral summer (not shown; please refer to Braconnot et al. (2007b) for more details). This might be related to the slight increase in obliquity which enhances the summer insolation and weakens the winter insolation in both hemispheres equally. Nonetheless, its contribution to the mean ITCZ shift is negligible (Mantsis et al., 2011).

The change in the annual mean zonal mean precipitation in models that include a dynamic ocean is shown in Fig. 4.1c (red dashed line). In the mid-Holocene there is an increase in precipitation north of the mean rainfall peak in the pre-industrial and a decrease in precipitation south of it, indicating a northward shift of the mean ITCZ in the mid-Holocene (Fig. 4.1c). Contrary to the results from the PMIP3 models that have dynamic oceans, the mean ITCZ shifts southward in the mid-Holocene compared to the pre-industrial simulation using the ECHAM4.6 model which is coupled to a slab ocean. A southward shift in the mean ITCZ is also seen in the extreme precession experiments using the ECHAM4.6 model coupled to a slab ocean (Battisti et al., 2014; Liu and Battisti, 2015) and in a pair of summer perihelion versus winter perihelion experiments using CCSM3 coupled to a slab ocean (personal communications with K. Chamales, August, 2013). That ocean dynamics is responsible for the difference in the directions of mean ITCZ location change between models with a slab ocean and models with a coupled ocean is explored in sections 4.34.3.3 and 4.

It is worth keeping in mind that the dominant feature of the precipitation change in the mid-Holocene is the seasonal asymmetry; the annual mean change is just the residual of the large seasonal changes although it is consistent across the models.

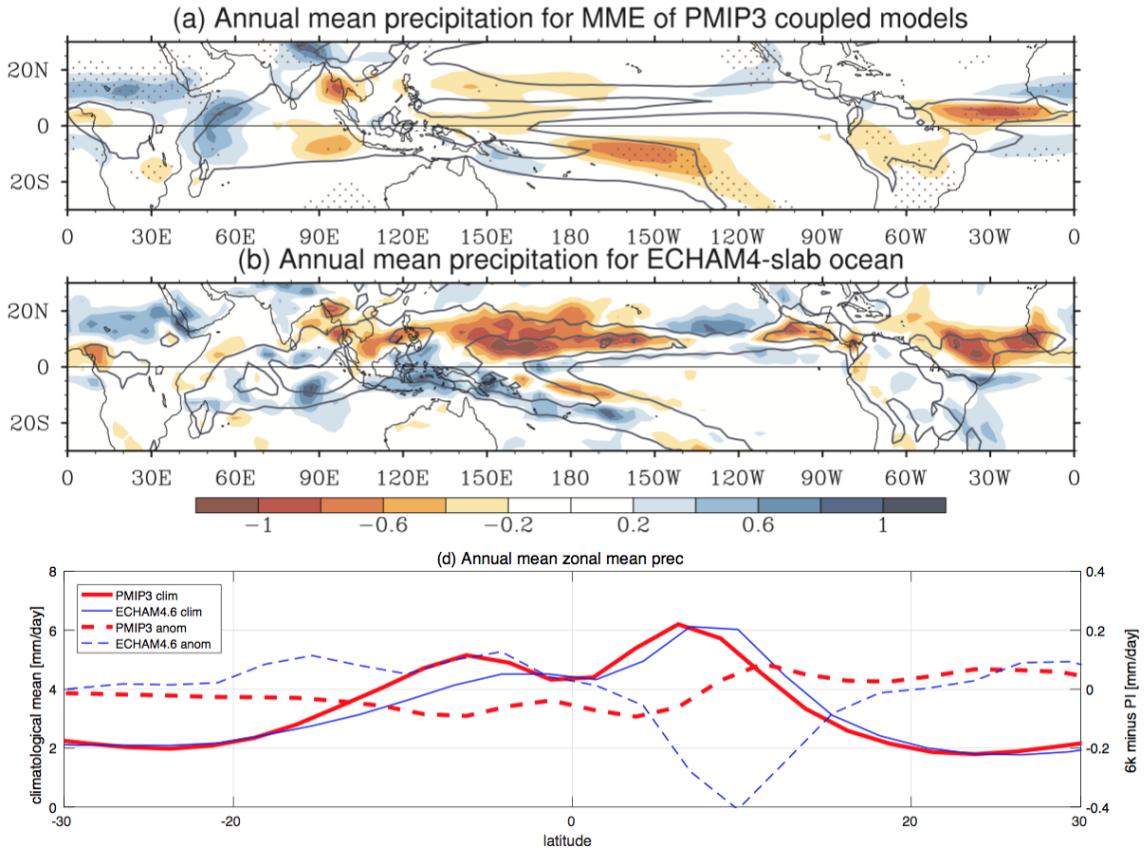

Figure 4.1: (a) The multi-model mean of climatological annual-mean precipitation in the pre-industrial experiment (contours; mm day^{-1}), and of the change in precipitation (mid-Holocene minus pre-industrial) from the PMIP3 models (shaded; mm day^{-1}). All of the PMIP3 climate models include dynamic oceans. (b) Same as (a), except for ECHAM4.6-slab ocean model. (c) Zonal-mean annual-mean climatological precipitation (solid lines; mm day^{-1}) and change in precipitation (dashed lines; mm day^{-1}) from the PMIP3 models (red) and from the ECHAM4.6-slab ocean model (blue).

4.3.2 Changes in cross-equatorial atmospheric heat transport

We use the precipitation centroid to indicate the mean ITCZ location. The precipitation centroid is defined as the latitude that delineates an equal area-average precipitation between 20°N and 20°S (Frierson and Hwang, 2012; Donohoe et al., 2013). In 9 out of 12 PMIP3 models, precipitation centroid shifts northward in the mid-Holocene compared to the pre-industrial climate (Fig. 4.2a). The ensemble mean shift is 0.11° with a spread from 0° to 0.32° (2 standard deviations).

A scatter plot of the changes in precipitation centroid versus changes in AHT(EQ) for the PMIP3 models shows that the change in the precipitation centroid is anti-correlated with the change in AHT(EQ), with a slope of $3.0°PW^{-1}$, close to that reported by Donohoe et al. (2013) for the seasonal cycle case (Fig. 4.2a) [2]. Figure 4.2a also shows that the atmosphere transports more energy southward across the equator ($\Delta AHT(EQ)<0$) in all PMIP3 models and is near zero in the ECHAM4.6 - slab ocean model. What causes the enhanced southward AHT(EQ) in the coupled simulations?

As shown in Eq. (4.5), in equilibrium, changes in the AHT(EQ) are related to changes in the hemispheric asymmetry (defined as "the spatial integral over the Northern Hemisphere minus that over the Southern Hemisphere, divided by 2") in the net energy input into the atmosphere, which, in turn, are determined by changes in the asymmetry in the hemispheric integral of $\mathrm{F_{TOA}}$ ($\frac{1}{2}\left[F_{TOA}\right]\Big|_{SH}^{NH}$) and/or $\mathrm{F_{SFC}}$ ($\frac{1}{2}\left[F_{SFC}\right]\Big|_{SH}^{NH}$), respectively. Decomposing the AHT(EQ) into these two components shows that in almost every model (9 out of 12 models), the change in AHT(EQ) is predominantly due to the change in $\frac{1}{2}\left[F_{SFC}\right]\Big|_{SH}^{NH}$, the hemispheric asymmetry in energy input to the atmosphere from the surface (Fig. 4.2b). In all 12 PMIP3 models, the change in surface energy fluxes leads to an increase in the heating of the atmosphere in the Northern Hemisphere and a decrease in atmospheric heating in the Southern Hemisphere, resulting in a positive anomaly in $\frac{1}{2}\left[F_{SFC}\right]\Big|_{SH}^{NH}$. There is no consistent change

[2] in calculating the slope, we leave out the apparent outlier, HadGEM2-ES. The slope would be $2.2°PW^{-1}$ if it was included

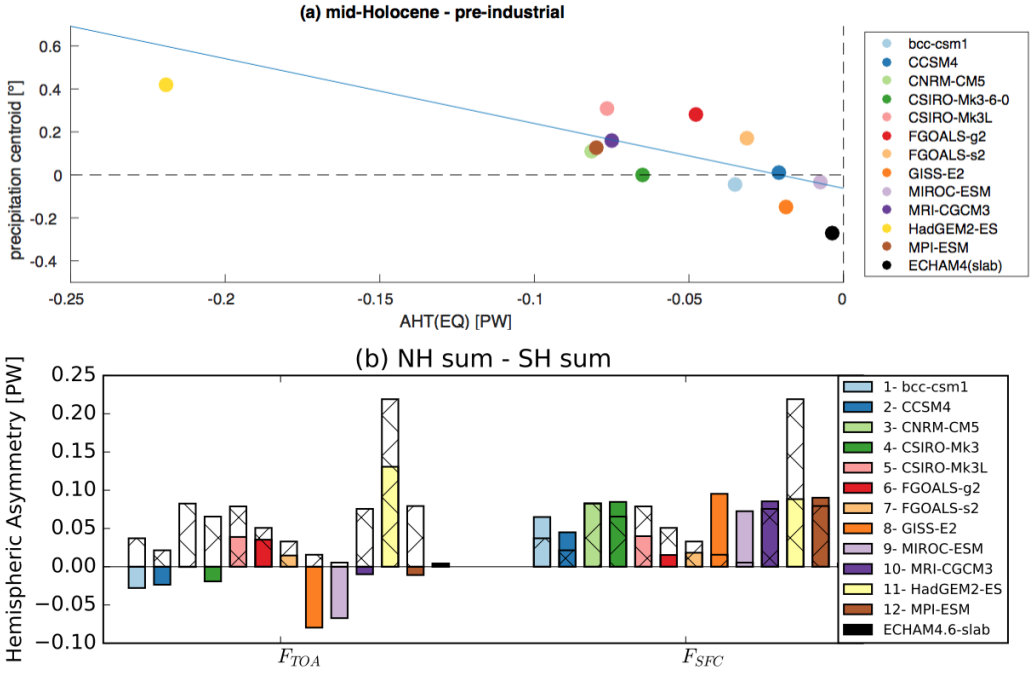

Figure 4.2: (a) Scatterplot of the change (mid-Holocene minus pre-industrial) in the latitude of the precipitation centroid versus the change in cross-equatorial atmospheric energy transport (ΔAHT(EQ); PW). The solid line is the least squares fit, 3° latitude/PW. (b) The change in the hemispheric difference in the net hemispherically integrated energy flux into the atmosphere (colored bars) at the top of the atmmosphere ($\frac{1}{2}[F_{TOA}]\Big|_{SH}^{NH}$, left) and at the surface ($\frac{1}{2}[F_{SFC}]\Big|_{SH}^{NH}$, right). For each model, the hatched bar represents the hemispheric difference in the net energy into the atmosphere; that is, the hatch bar is $-\Delta$AHT(EQ), which is the sum of the two colored bars for each model (see Eq. (4.5)). Note that at equilibrium, the change in the net surface flux in the ECHAM4.6-slab ocean model is zero. The coloring in (b) follows the key in panel (a).

in $\frac{1}{2}\left[F_{TOA}\right]\Big|_{SH}^{NH}$ across the models (Fig. 4.2b). In equilibrium, the change in $\frac{1}{2}\left[F_{SFC}\right]\Big|_{SH}^{NH}$ has to be balanced by an anomalous ocean heat transport across the equator from the Southern Hemisphere to the Northern Hemisphere. This is discussed next.

Note that there is an imbalance in global average energy budget in each model (Lucarini and Ragone, 2011). This imbalance is much smaller than the change in hemispheric asymmetry between the mid-Holocene and the pre-industrial climate. It is also explicitly removed from the calculation of energy transports by subtracting the change in Northern Hemisphere top-of-atmosphere fluxes and surface fluxes from those in the Southern Hemisphere (Eq. (4.5)). It therefore does not impact the validity of the results presented here.

4.3.3 Change in cross-equatorial oceanic heat transport

Changes in the cross-equatorial ocean heat transport (OHT(EQ)) between the mid-Holocene and pre-industrial simulations are given by

$$\Delta OHT(EQ) = \rho_0\, C_p \int_{-H}^{0}\int_{0}^{L} \left[(vT)_{6K} - (vT)_{PI}\right] dx\, dz. \tag{4.6}$$

where ρ_0 is density of seawater, C_p is the heat capacity, and the product of $\rho_0 C_p$ is nearly constant in the ocean with a mean value of $4.1 \times 10^6 Jm^{-3}K^{-1}$ used here. v is meridional velocity, T is ocean potential temperature, and H and L are the depth and width of the ocean of the longitude-height cross section along the equator, respectively; subscripts $6K$ and PI represent the mid-Holocene simulation and the pre-industrial simulation, respectively.

We use the monthly climatology of v and T to calculate ΔOHT(EQ), neglecting the contribution by submonthly covarying anomalies associated with natural variability. OHT(EQ) and ΔOHT(EQ) calculated this way, however, are close to the "exact" answer output by the ocean model throughout the integration (see Appendix). Note that changes in OHT(EQ) calculated this way are not exactly the same with those derived from the hemispheric asymmetry in the change in surface energy flux, $\Delta\frac{1}{2}[F_{SFC}]\Big|_{NH}^{SH}$ (cf. blue and green bars in Fig. 3). Differences between these two estimates of ΔOHT(EQ) could be due to several factors, including: neglecting the contribution of submonthly covarying anomalies associated with

natural variability, changes in ocean dissipation, and inaccuracies in the *a posteriori* calculation of ocean heat transport due to the re-gridding of the model output. Nonetheless, both methods yield qualitatively similar results and both methods indicate that in all 12 models, the oceans are transporting more heat into the northern hemisphere during the mid-Holocene. The likelihood of 12 models all showing the same direction of change from simply averaging errors is 1 in 2^{11}. The robustness of increase in northward OHT(EQ) during the mid-Holocene that we have extracted using the full ensemble of models and using multiple methods to calculate the OHT(EQ) is truly astonishing.

In the analysis that follows, we do not present results from the HadGEM2-ES because the ocean data from this model are not available from the archive. We also neglect the MPI model because the complex grid configuration makes an *a posteriori* calculation of OHT(EQ) unreliable.

The change in the OHT(EQ) calculated from the spatial integral of the surface heat fluxes ($\Delta\frac{1}{2}[F_{SFC}]\Big|_{NH}^{SH}$) is shown in green in Fig. 4.3a and those calculated from the ocean temperature and currents (Eq. (4.6)) are shown in blue. Both methods calculate positive OHT(EQ) change in every model (Fig. 4.3a). We next apply Eq. (4.6) and the spatial integral of surface heat fluxes to each ocean basin. In all models, the changes in the Indo-Pacific Ocean are responsible for the northward ΔOHT(EQ); the contribution to ΔOHT(EQ) from the Atlantic basin is highly model dependent (cf. Figs. 4.3b and 4.3c).

The change in OHT(EQ) can be further decomposed into that due to a change in the ocean circulation Δv and that due to a change in ocean temperature ΔT:

$$\Delta OHT(EQ) = \rho_0\, C_p \int\int T\, \Delta v\, dx\, dz + \rho_0\, C_p \int\int v\, \Delta T\, dx\, dz + \rho_0\, C_p \int\int \Delta v\, \Delta T\, dx\, dz. \tag{4.7}$$

Hereafter, we refer to the first term of the right-hand side as the "dynamic" contribution and the second term as the "thermodynamic" contribution. Of the two, the "dynamic" component is the larger term in all but one model (cf. Figs. 4.3e and 4.3f). As such, there is a fair correspondence between the "dynamic" contribution and the total change in OHT(EQ) (cf.

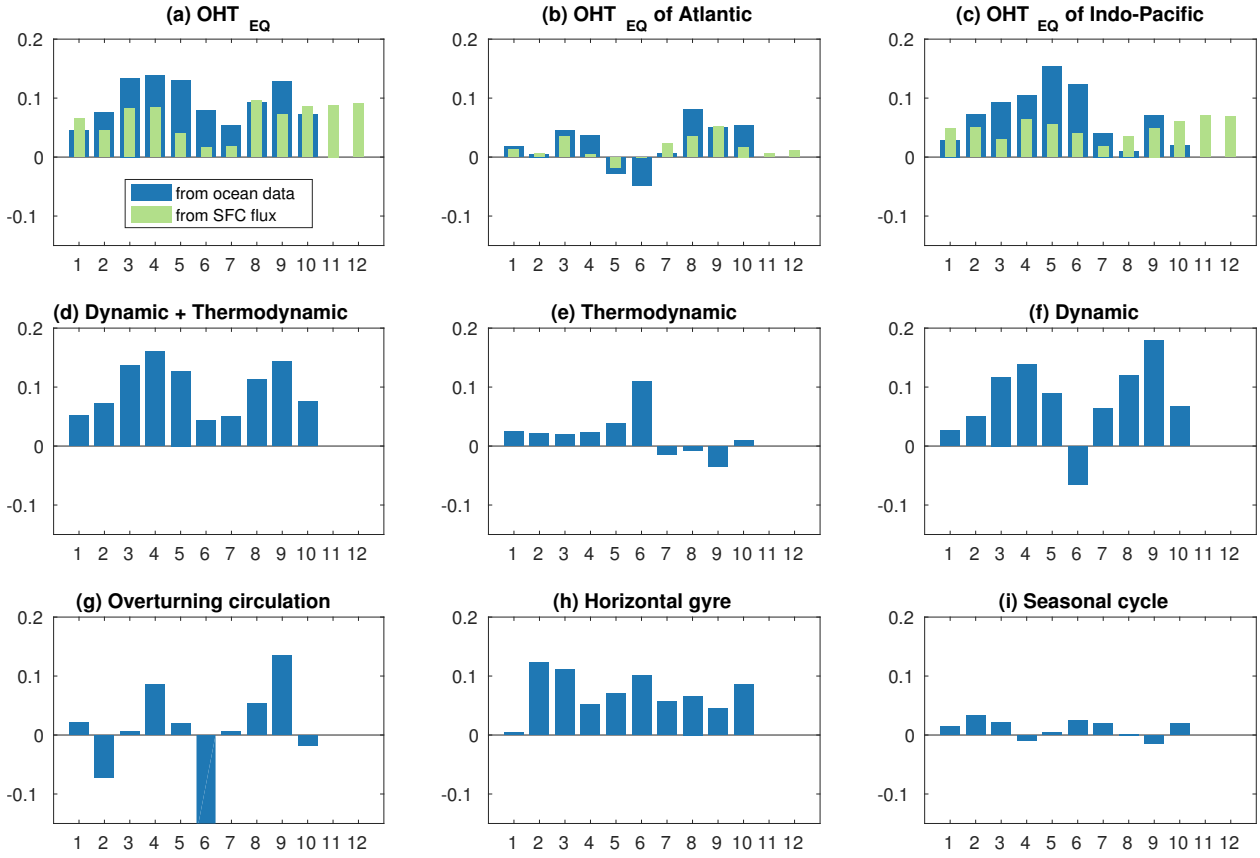

Figure 4.3: Change in the cross-equatorial ocean heat transport (ΔOHT(EQ); PW) between the mid-Holocene and the pre-industrial for (a) the sum of the ocean basins, (b) the Atlantic basin only, and (c) the Indo-Pacific basins only. The green bars in panels (a - c) represent the results derived from the hemispheric asymmetry in the change in surface energy flux, $\Delta\text{OHT(EQ)} = -\Delta\frac{1}{2}[\text{F}_{\text{SFC}}]\Big|_{\text{SH}}^{\text{NH}}$, and blue bars denote results obtain directly from the ocean model output (Eq. (4.6)). Panels (e) and (f) are the changes in OHT(EQ) associated with changes in the ocean temperature only and changes in the ocean circulation only, respectively (see Eq. (4.7)); panels (e) and (f) sum to the results shown in panel (d). The dynamic contribution shown in (f) is further broken into contributions associated with (g) the change in overturning circulation and (h) the change in gyre circulation (see Eq. (4.8)). (i) shows the changes in the dynamic contributions that are due to the changes in the seasonal cycle.

the blue bars in Fig. 4.3a with the bars in 4.3f). The nonlinear term (the last term of the right-hand side of Eq. (4.7)) is negligible, evident by comparing the sum of the "dynamic" and "thermodynamic" components (Fig. 4.3d) with the total change in OHT(EQ) (Fig. 4.3a).

The dynamic term can be further broken into overturning and horizontal gyre components (Hall and Bryden, 1982):

$$\rho_0 C_p \int\int \overline{T\,\Delta v}\,dx\,dz = \rho_0 C_p \int \bar{T}\,\Delta\overline{v}\,dz \int dx + \rho_0 C_p \int\int \overline{T'\,\Delta v'} dz\,dx, \qquad (4.8)$$

where overbars represent the zonal mean at each vertical level and primes denote deviations from the zonal mean. The first term on the right-hand side of Eq. (4.8) is the contribution due to the zonal average overturning circulation, while the second term is associated with the horizontal gyres. The systematic northward change in the OHT(EQ) is clearly associated with changes in the horizontal gyre circulation (cf. Figs. 4.3g and 4.3h). Of the three ocean basins, the western Pacific is the primary contributor to the changes in OHT(EQ) associated with changes in ocean circulation. In the Indian Ocean, a weakened Somali jet drives southward OHT(EQ) anomalies that are largely offset by northward anomalies in the interior ocean, rendering a small net dynamic contribution in Indian Ocean (not shown). Changes in the overturning circulation do not contribute to Δ(OHT(EQ)) in a systematic way across the models. Finally, changes in OHT are relatively uniform through the year. The influence of the seasonal covariance of temperature and current changes is small (Fig. 3i). [3]

The changes in ocean circulation and hence OHT(EQ) are primarily due to changes in wind stress in the Indo-Pacific region that have a common pattern across nearly all of the

[3]Fig. 3i shows the importance of seasonal covariance of temperature and current changes for the change in cross equatorial OHT estimated as follows. We first calculate the change in annual mean heat transport using (i) the monthly climatology of currents and temperatures from the pre-industrial and mid-holocene simulations (shown in blue bars of Fig. 3a). We then estimate the change in OHT by (ii) adding the annual mean changes (mid-Holocene minus pre-industrial) in the currents and temperatures to the climatological annual cycle in the pre-industrial simulation, and then subtracted the pre-industrial heat transport. The difference between (i) and (ii) is plotted in Fig. 3i, and shows that the changes in cross equatorial OHT are largely independent of the changes in the seasonal cycle in currents and temperatures.

models. Figure 4.4c shows the multi-model-mean change in the annual-mean wind stress in the PMIP3 models associated with the mid-Holocene compared to the present. The pattern seen in Fig. 4.4c is common to all the PMIP3 models we examined (cf. Figs. 4.4c, 4.4d and Fig. A3). Over the Indian Ocean and far western Pacific, enhanced Trades (easterly stress anomalies) are seen along and to the north of the equator in 10 of 12 models (including the ECHAM4.6 model coupled to a slab), resulting in a positive wind stress curl near the equator. According to Sverdrup transport theory, the positive curl in the western Indo-Pacific basin drives northward movement of water in the upper ocean. Although there are negative curl anomalies in the eastern Pacific which drives southward movement of water in the upper ocean, because the upper ocean water in the western Indo-Pacific is warmer than that in the eastern Pacific, the anomalous gyre circulation produces a northward zonally averaged ocean heat transport anomaly across the equator. The role of surface wind stress and hence horizontal gyre in generating the anomalous ocean heat transport is also found by Braconnot et al. (2000) using the coupled version of Institut Pierre Simon Laplace (IPSL) model.

From the analysis above, it is clear that the increase in northward OHT(EQ) in the mid-Holocene – seen in all of the 10 models coupled to a dynamic ocean – is due to changes in wind stress in the western Pacific. These wind anomalies are seen in nearly every PMIP3 model (which employ dynamical ocean models), as well as in an ECHAM4.6-slab ocean model (Fig. 4.4d), and hence are independent of the ocean circulation changes. Indeed, the wind changes are a monsoonal response to the orbitally driven changes in insolation during the mid-Holocene (Battisti et al., 2014; Liu and Battisti, 2015): in the Northern Hemisphere, the stronger summer insolation shifts convection from the ocean to the land in the Indian Ocean Basin, resulting in annually averaged easterly anomalies in the tropical Indian Ocean basin and the western Pacific ocean; in the Southern Hemisphere, the weaker summer insolation shifts convection from the land to the ocean, resulting in annually averaged westerly anomalies in the tropical Indian Ocean basin and the western Pacific ocean (Figs. 4.4a, b).

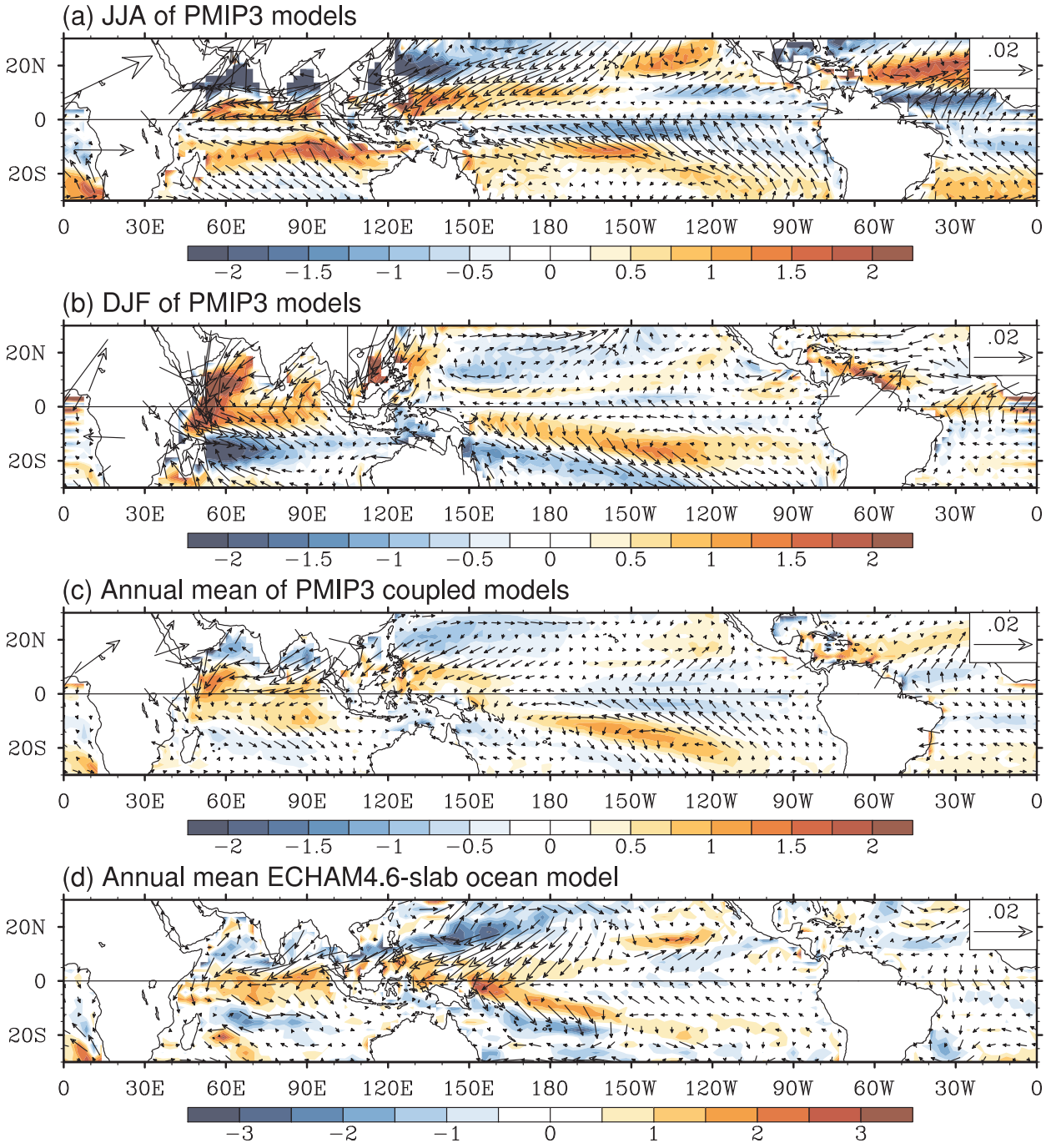

Figure 4.4: Change in the annual-mean surface wind stress over the oceans (vectors; Pa) and its curl (shading; 10^{-8} N m^{-3}), mid-Holocene minus pre-industrial. Shown in (a), (b) and (c) are the June-July-August mean change, December-January-February mean change and annual mean change from the multi-model mean of the PMIP3 models, respectively. (d) Same as (c), except for from the ECHAM4.6-slab ocean model. Note the color bar of panel d is different from the others.

4.4 *A Mechanistic Model of the change in mean ITCZ and in the cross-equatorial ocean heat transport*

In the ECHAM4.6 model that employs a slab ocean, insolation changes are responsible for a southward shift of the mean ITCZ. In most of the models (9 out of 12) with a dynamic ocean, however, there is a northward shift in ITCZ. The analyses presented in the previous section suggest changes in ocean circulation play a crucial role in the changes in the interhemispheric energy transport associated with insolation forcing. The mechanism responsible for the different responses in the model that employs the slab ocean and all of the models that employ dynamical oceans is shown schematically in Fig. 4.5 and is summarized as follows.

In the previous section, we showed that insolation differences between the mid-Holocene and today drive similar changes in precipitation and very similar changes in tropical atmospheric circulation in both the models with and without a dynamic ocean (Hsu et al., 2010; Chamales, 2014). The changes in precipitation and atmospheric circulation are overwhelmingly zonally asymmetric in all of the models (cf. Fig. 4.1 with Fig. 4.6); indeed the zonally averaged wind stress anomalies are less than 20% of the typical wind stress anomaly. The robust changes in atmospheric circulation over the Indian and Pacific Oceans feature a change in the wind stress curl in the equatorial regions of these ocean basins that, acting on a zonally asymmetric climatological temperature structure, results in basin averaged northward increase in ocean heat transport across the equator, particularly in the tropical Pacific. The atmosphere, in turn, experiences an increase in heat absorbed in the northern hemisphere that is not completely compensated for by changes in the top-of-the atmosphere radiation. Hence, to maintain equilibrium, the atmosphere must move anomalous heat into the Southern Hemisphere. Since the atmosphere moves energy across the equator overwhelmingly by the zonally averaged overturning circulation, this requires the zonally averaged Hadley circulation and attendant ITCZ to shift northward. In contrast, in the ECHAM4.6 model coupled to a slab ocean, there is a southward shift in the ITCZ and an anomalous increase in AHT(EQ). Radiative feedbacks (i.e. radiation changes in response to changes in clouds

and water vapor) in response to mid-Holocene insolation changes result in a radiative input to the Southern Hemisphere ($\Delta\frac{1}{2}\left[F_{TOA}\right]\Big|_{SH}^{NH} < 0$) that shift the mean ITCZ southward.

The mechanism discussed above –whereby enhanced wind-driven northward ocean heat transport induces a northward shift in the Hadley Cell and ITCZ– explains the robust ensemble mean northward ITCZ shift from the perspective of the energetic framework of ITCZ shifts. While the northward ocean energy transport increases in all models considered here, there are two main reasons that individual model simulations show varying magnitudes and directions of ITCZ shifts (Fig. 4.2): i) the hemispheric contrast of top-of-the-atmosphere radiative changes varies in sign and direction between models: a nearly equal number of models simulating anomalous radiative input in to the Northern Hemisphere as those that simulate anomalous energy input to the Southern Hemisphere (left panel of Fig. 4.2b); and ii) the relationship between AHT(EQ) and precipitation centroid explains a significant portion of the ensemble average and spread in ITCZ shifts but is far from perfect (i.e. the individual dots do not fall exactly on the a straight line through the origin in Fig. 4.2a. The latter could result from changes in static stability or local precipitation changes projecting onto the zonal mean precipitation without concomitant changes in the Hadley cell. As a result, even though the enhanced northward ocean transport is seen in every model, it is not a useful predictor of ITCZ shifts in a given climate model.

4.5 Conclusion and Discussion

Orbitally induced insolation changes impact tropical precipitation dramatically. We have demonstrated that, in addition to the intensification of the Northern Hemisphere monsoon and (not emphasized) the weakening of the Southern Hemisphere monsoon in the mid-Holocene, in all 12 PMIP3 climate models that employ a dynamic ocean, the northward OHT(EQ) is enhanced and the southward AHT(EQ) is also enhanced as a result. In contrast, in models without interactive oceans, AHT(EQ) is nearly unchanged. The change in cross-equatorial atmospheric heat transport is accomplished by the Hadley Cell; hence, the mean ITCZ shifts northward in the models with an interactive ocean.

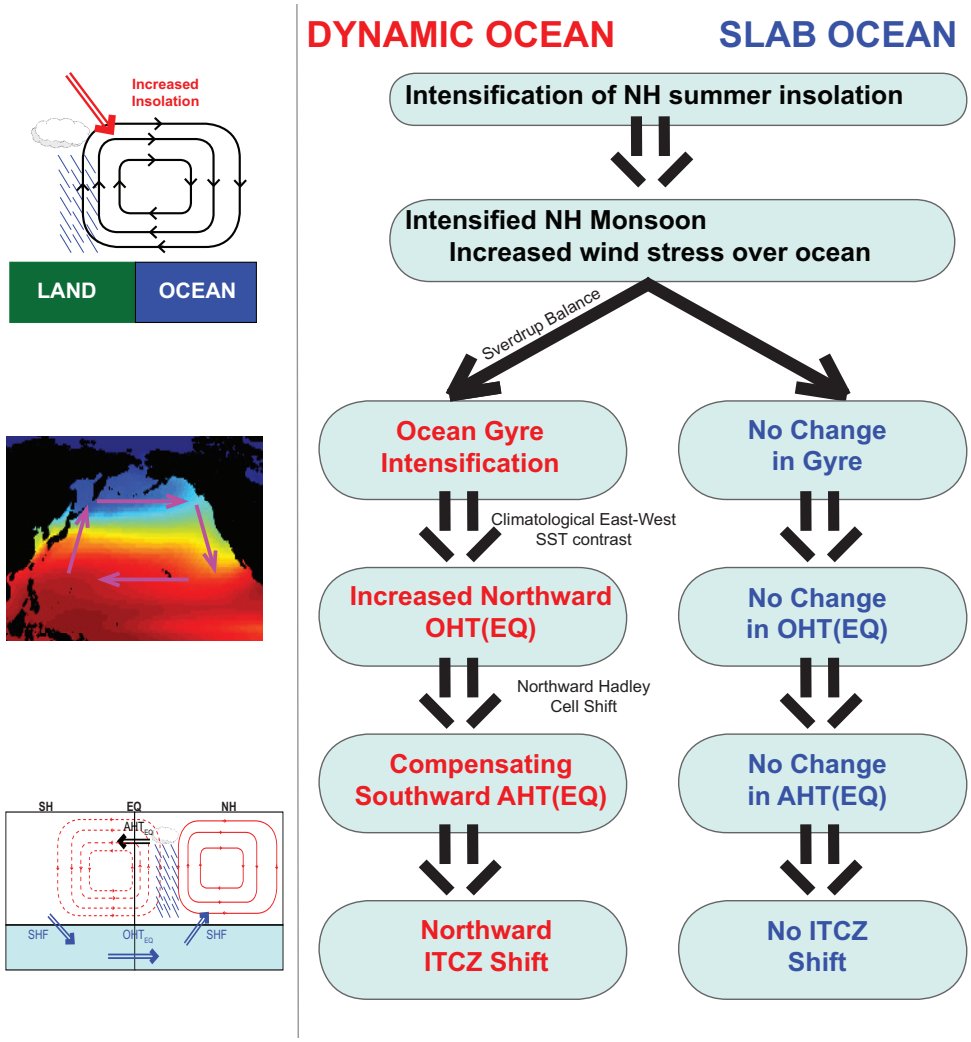

Figure 4.5: Processes controlling how insolation differences between the mid-Holocene and present day change ITCZ and AHT(EQ) differently in an atmosphere-dynamic ocean model (left) versus an atmosphere-slab ocean model (right). Insolation differences first drive zonally and seasonally asymmetric anomalies in atmospheric circulation and hence in the surface wind stress. In the slab ocean, the changes in wind stress don't impact the ocean circulation or the heat transport. In the dynamic ocean, however, the changes in wind stress over the Indo-Pacific oceans drive zonally asymmetric change in ocean circulation, which, acting on the zonally asymmetric climatological temperature, induces a zonally-averaged anomalous northward ocean heat transport across the equator and results in anomalous heating of the Northern Hemisphere (cooling of the Southern Hemisphere). To maintain equilibrium, the atmosphere moves anomalous heat from the Northern Hemisphere to the Southern Hemisphere by shifting the Hadley Cell and the attendant mean ITCZ northward.

The increase in northward OHT(EQ) is accomplished by changes in the upper ocean gyre circulations in the Indo-Pacific, and particularly the Pacific Ocean; there is no systematic change in the ocean heat transport in the Atlantic Ocean. The changes in the wind stress that drive the anomalous gyre circulations are independent of whether the models have a dynamical ocean: the surface circulation pattern that drives the gyre circulation changes is clearly seen in all but one of the 12 models examined; it is also simulated by the ECHAM4.6 coupled to a slab-ocean model used in this study. However, the impact of this wind stress change on the mean ITCZ varies between coupled simulations and slab ocean simulations: in coupled simualtions the wind stress changes spin up the tropical Pacific gyre, enhancing the northward ocean heat tranpsort and demanding a northward Hadley cell and ITCZ response, whereas this same mechanism is absent in slab ocean simulations. The ITCZ shift in a minority of models (bcc-csm1, MIROC-ESM and GISS-E2) is southward – contrary to the northward shift expected from the above mechanism – due to both radiative feedbacks and departures from the energetic framework. However, the robust northward ITCZ shift seen in the ensemble of PMIP3 mid-Holocene simulations would not exist without the coupling between the wind stress changes and the ocean circulation. We speculate that an ensemble of slab-ocean mid-Holocene simulations would exhibit inter-model differences in the ITCZ shift with no significant ensemble mean shift.

Many modeling studies examining the impact of forcing on the ITCZ employ atmospheric models coupled to slab ocean models. However, results from our study demonstrate that – at least for changes in insolation – the response of ITCZ is mainly due to dynamical changes in the ocean that are driven by the overwhelmingly zonally asymmetric atmospheric circulation anomalies that are, in turn, independent of the ocean circulation changes (the latter result is also found in several other studies: Clement et al., 2004; Hsu et al., 2010; McGee et al., 2014; Battisti et al., 2014; Liu and Battisti, 2015).

We note that the difference in insolation between the mid-Holocene and pre-industrial periods induce changes in atmospheric circulation in the tropical Indian and Pacific Oceans that are common to almost all models (cf. Figs. 4.4 and A3), regardless of whether dynam-

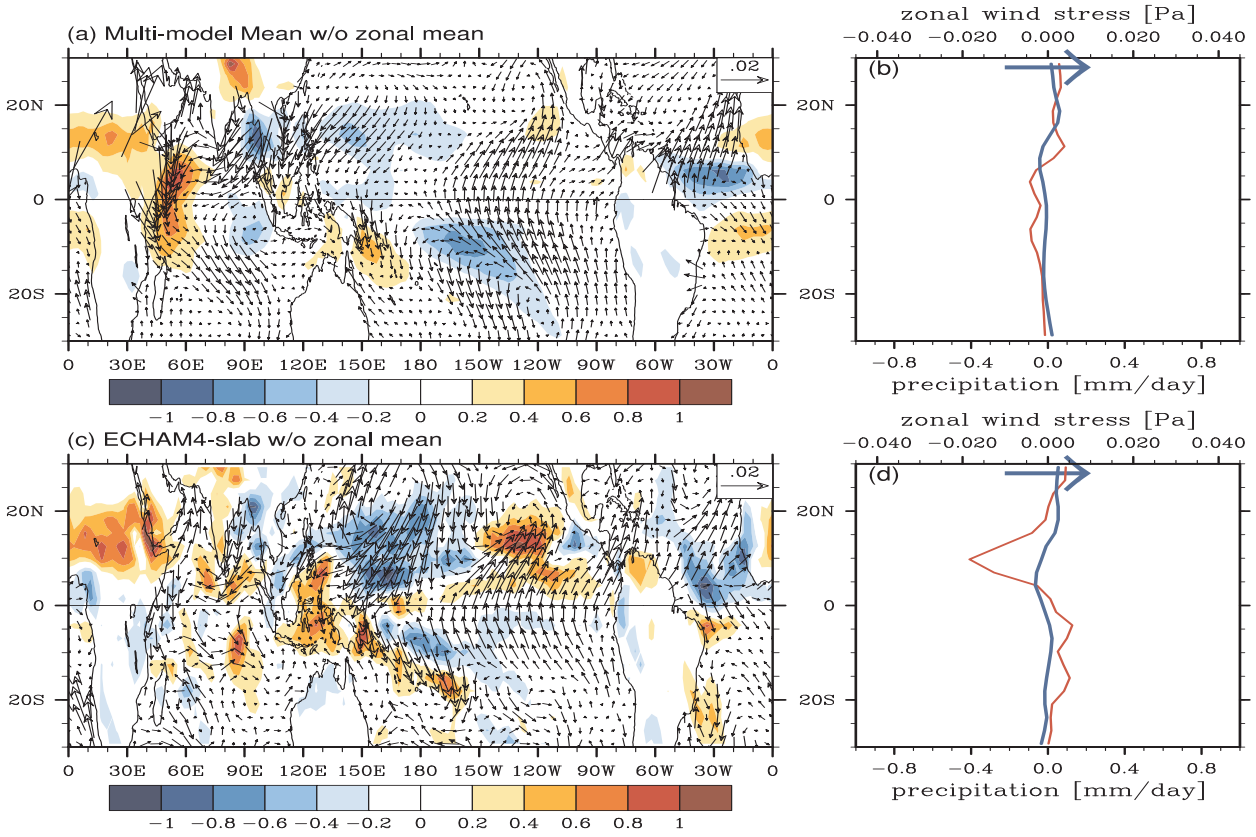

Figure 4.6: (a) Change (mid-Holocene minus pre-industrial) in the annual-mean surface wind stress over the oceans (vectors; Pa) and precipitation (shading; mm day^{-1}) after removal of the zonal mean value of each latitude. Shown in (a) is the multi-model mean from the PMIP3 models. Panel (b) shows the zonal mean change in surface zonal wind stress (blue) and in precipitation (red) which, when removed from Figs. 1a and 4c, create the figure shown in panel (a). Panels (c) and (d) are the same as panels (a) and (b), but for the ECHAM4.6-slab ocean model. The arrow in (b) and (d) is the reference wind stress vector used in (a) and (c).

ical changes in the ocean are considered. The pattern of insolation induced precipitation changes over tropical land regions is also common to most of the models, but less so than the circulation changes – particularly over the ocean basins (cf. Figs 4.1a and 4.1b). This result has been reported in a previous study of the response of the circulation and precipitation of the maritime continent to increasing CO_2 (Vimont et al., 2010) and is expected. Monsoon circulations and precipitation are intimately related to the near-surface moist static energy (Prive and Plumb, 2007a,b; Bordoni and Schneider, 2008; Boos and Kuang, 2010). The dynamical scale associated with changes in the monsoon circulations due to changes in near-surface moist static energy is the equatorial Rossby radius, which is $\sim 10^6$m; in contrast, the storms that release the energy that drives the monsoon circulations are at least an order of magnitude smaller than the spatial scale associated with the monsoon circulations. Hence, the relevant heating for the monsoon circulations is the aggregate of the precipitating elements: the details of the distribution of precipitation are secondary for setting the circulation response. In addition, the dynamics associated with the monsoon circulations is explicitly resolved in climate models, while the convective elements that convert the surface energy to atmospheric heating are parameterized.

Finally, although the focus of our paper is on understanding the zonal mean response to insolation forcing, it is important to keep in mind that the dominant changes in tropical climate (precipitation, temperature (not shown), wind) are zonally asymmetric. This can be seen, for example, in the asymmetry of the precipitation changes (Fig. 4.1), as well as by comparing the maps of precipitation and wind stress change with and without the zonal mean removed (cf. Figs. 4.1, 4.4 and 4.6): the figures are nearly identical. Indeed, although the global zonal average precipitation in the deep tropics (represented by the precipitation centroid) moves northward in response to mid-Holocene insolation compared to pre-industrial insolation, changes in ITCZ are accomplished by the sum of differential changes in the zonal average precipitation over each ocean basin and over the land regions (Fig. 4.7): on average the zonal average precipitation over the Atlantic ocean moves southward, while that over land moves northward (over the Indian and Pacific oceans, the sign of the meridional dis-

placement is not a robust model result). We note that a follow up study (Atwood et al., in preparation) shows that the zonally averaged ITCZ displacement due to other forcings (volcanic, freshwater, CO_2, and land ice) is also accomplished by a sum of differential displacements in the zonal mean precipitation averaged over each basin. The implications for inferring larger scale climate changes from local proxy records of precipitation are apparent.

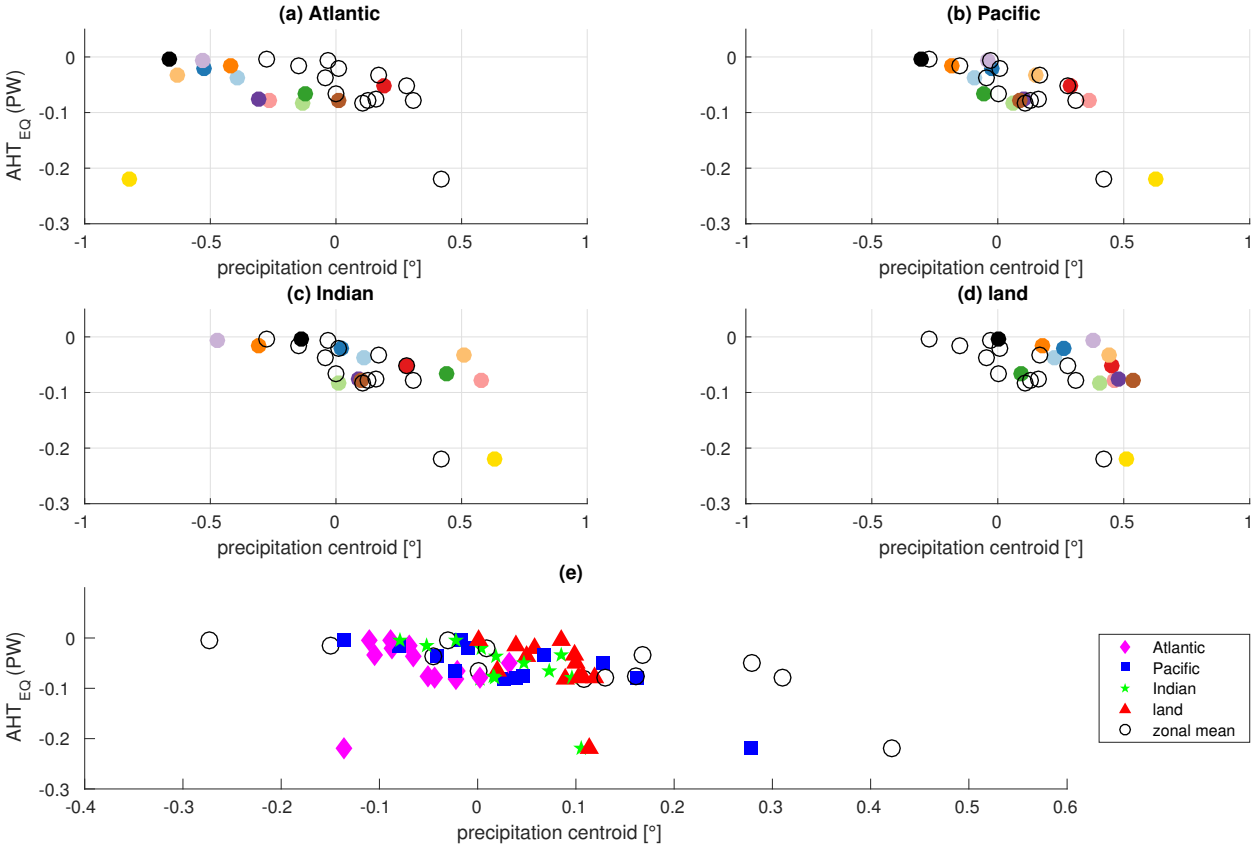

Figure 4.7: Scatter plots of changes in precipitation centroid vs. ΔAHT(EQ). Averages are shown over (a) the Atlantic Basin, (b) the Pacific Basin, (c) the Indian Basin, and (d) all land. The color code in panels (a)-(d) is the same as the one used in Fig. 4.2. The results in panels (a)-(d) are re-plotted in panel (e) with the precipitation centroid scaled by the fraction of the latitude circle occupied by the respective basin. Black unfilled circles in each panel represent the changes in the zonal mean precipitation centroid vs. ΔAHT(EQ), i.e. the same as the colored dots in Fig. 4.2a.

Chapter 5

CONCLUDING REMARKS

The Earth's climate is influenced by external forcings through time. The goal of this thesis is to understand the impacts of large-scale forcings on the Earth's climate, providing insights for understanding climate change that happened in the past and might happen in the future. The key findings of our study are listed below:

1. **An example that dynamics dictates the Earth's meridional energy transport** We explored the question "What determines the meridional heat transport (MHT)?" by varying Earth's rotation rate between 1/16 and 4 times the present-day value and allowing for the concomitant change in clouds and water vapor distribution that we hypothesize are fundamental to determining MHT. Increasing rotation rate causes a narrowing and weakening of the Hadley Cell, which in turn induces changes in tropical and subtropical clouds. Changes in the meridional heat transport (MHT) are linked to the accommpanying changes in both tropical high and subtropical low clouds. For both GFDL AM2.1 and CAM4, the adjustments of clouds cause changes in absorbed shortwave radiation and outgoing longwave radiation and these changes compensate each other. In GFDL AM2.1, the compensation is nearly complete, resulting in a fast-rotating regime in which MHT stays relative invariant.

2. **Narrowing the Atlantic and increasing atmospheric CO_2 changes the South American precipitation in the opposite way.** In an attempt to understand the tropical South American climate during the early Eocene, we examined two factors that are potentially most important: a narrower Atlantic ocean and enhanced atmospheric CO_2 concentration, using ECHAM 4.6 and CAM5. Our numerical experiments show that, to first order, narrowing the Atlantic decreases the precipitation of tropical South America, whereas increasing atmospheric CO_2 tends to increase the precipitation. The precipitation enhance-

ment associated with higher atmospheric CO_2 is as predicted by the "rich-get-richer, poor-get-poorer" mechanism. The precipitation reduction associated with a narrower Atlantic is mainly due to a reduction in the water vapor flux into South America across the northeast and east boundaries, not due to change in the atmospheric circulation. This, in turn, is due to reduction in the amount of water vapor the air parcels picked up from the ocean as they travel from Africa to the South American continent, which is a result of reduction in transit time. The early Eocene tropical South America in both models (driven by both a narrower Atlantic and a higher CO_2) is drier than today. It is a near-linear contribution of change in atmospheric CO_2 concentration and change in Atlantic geometry, with a dominant contribution from the latter.

3. **Orbitally induced insolation changes impact tropical precipitation dramatically.** In the mid-Holocene, changes in the seasonality of insolation drive an enhancement of the Northern Hemisphere monsoon and (not emphasized) the weakening of the Southern Hemisphere monsoon. This feature is seen in both climate models coupled to a slab ocean and climate models coupled to a dynamic ocean. In models with an interactive ocean, the monsoonal atmospheric circulation changes intensifies the northward ocean heat transport across the equator, by driving an enhanced upper-ocean gyre circulation in the tropical Pacific acting on the zonally asymmetric climatological temperature distribution. To maintain energy equilibrium, the Hadley cell and the attendant intense zonal mean precipitation (mean ITCZ) shift northward, transporting atmospheric energy southward across the equator. This feature is absent in climate models coupled to a slab ocean.

Appendix A

APPENDIX FIGURES FOR CHAPTER 4

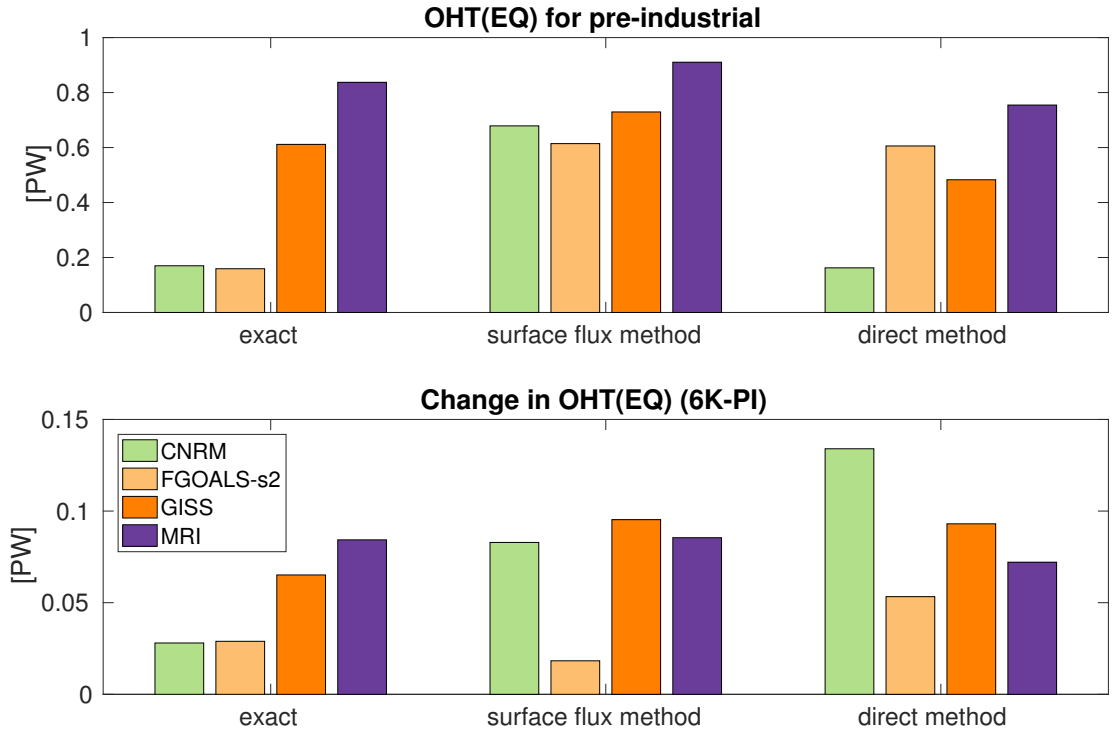

Figure A.1: OHT(EQ) of the pre-industrial simulation (upper) and the difference in OHT(EQ) between pre-industrial and mid-Holocene (ΔOHT(EQ); lower), calculated using three methods. In the figure, "exact" denotes OHT(EQ) calculated by the model and outputed during the simulation (the "exact" answer); and surface flux method refers to OHT(EQ) derived from the hemispheric asymmetry in the change in surface energy flux, $\Delta\text{OHT(EQ)}) = -\Delta\frac{1}{2}[\text{F}_{\text{SFC}}]\Big|_{\text{SH}}^{\text{NH}}$; and direct method refers to the calculation of OHT(EQ) from ocean current and temperature output from the model.

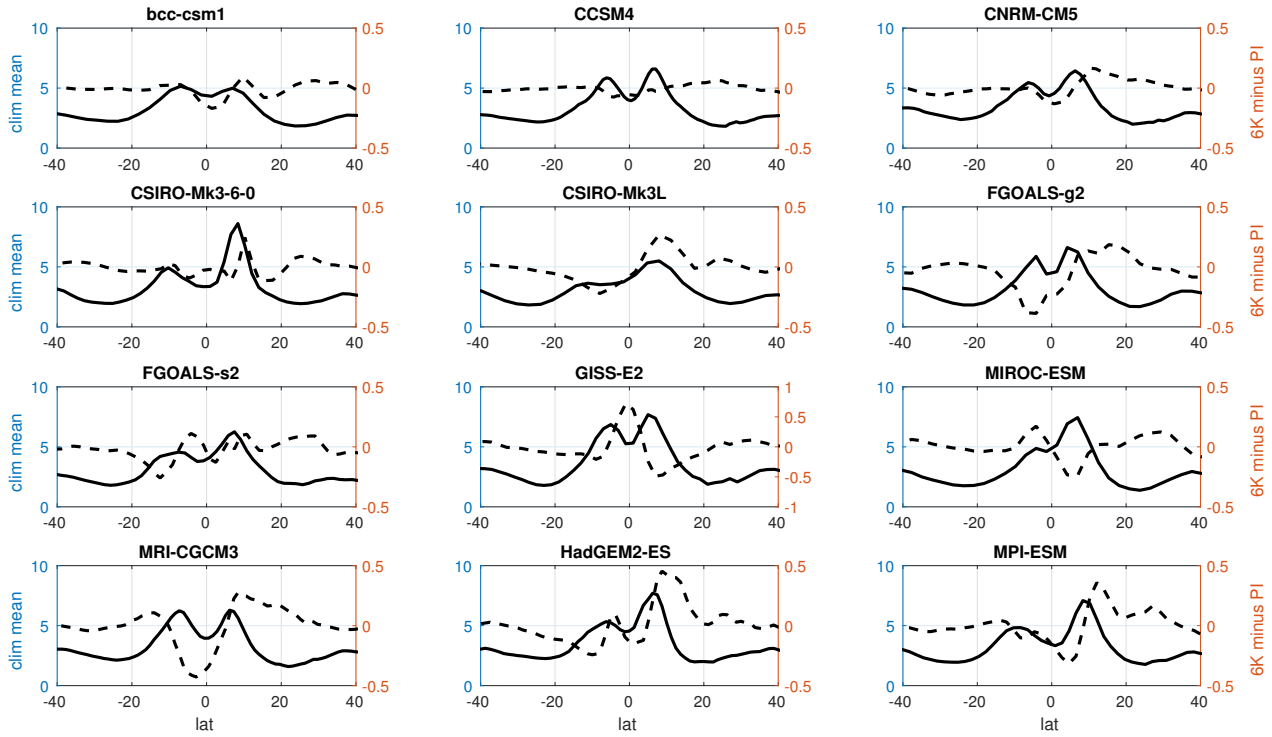

Figure A.2: The climatological annual-mean precipitation in the pre-industrial experiment (solid line; units: mm/day) and the change in annual-mean precipitation (mid-Holocene minus pre-industrial; dashed line; units: mm/day) for each PMIP3 model.

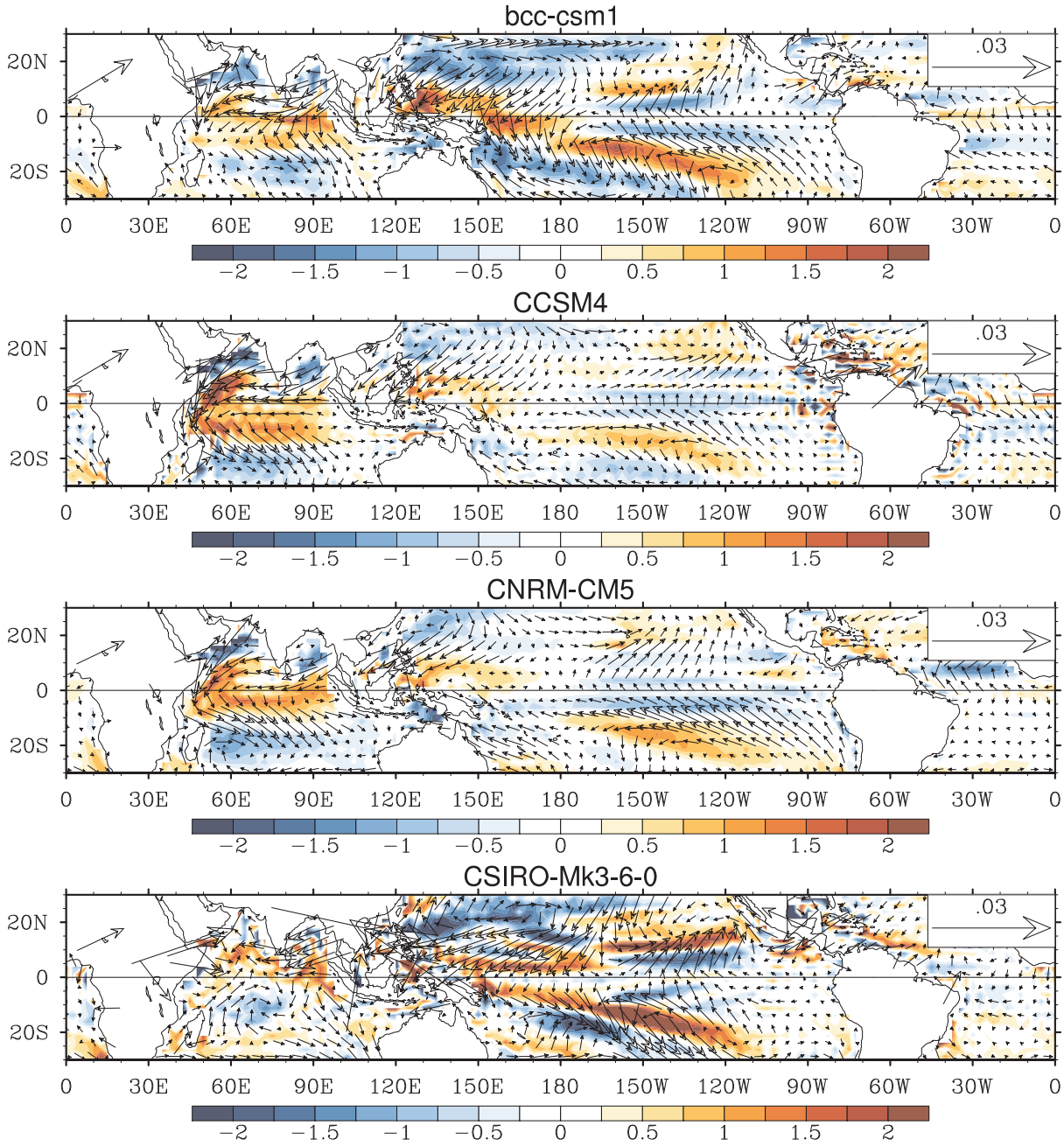

Figure A.3: Changes (mid-Holocene minus pre-industrial) in the annual mean surface wind stress (vectors; Pa) and wind stress curl (shading; 10^{-8} N m^{-3}) for each PMIP3 model.

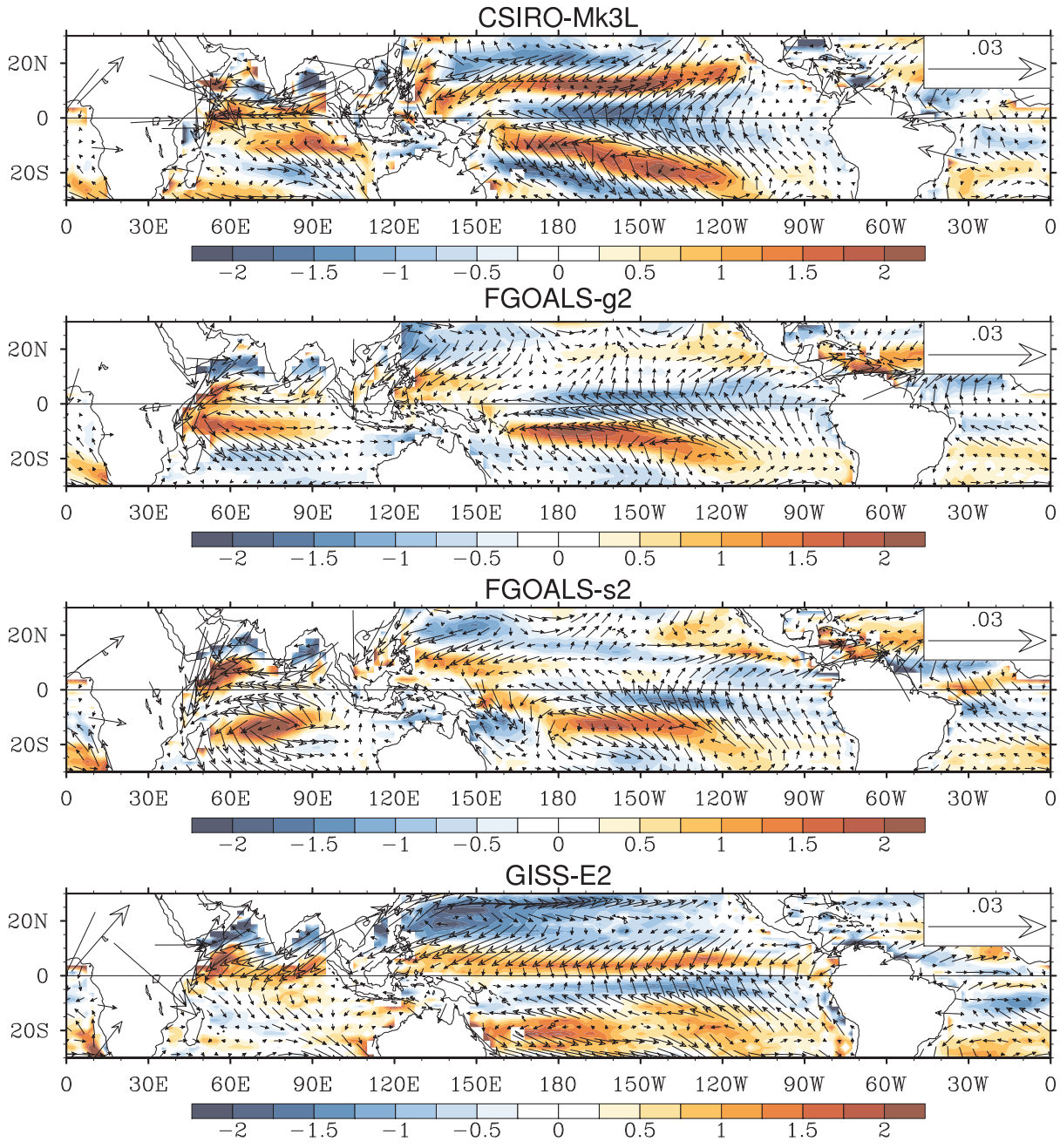

Figure A.4: Fig. A.3 continued.

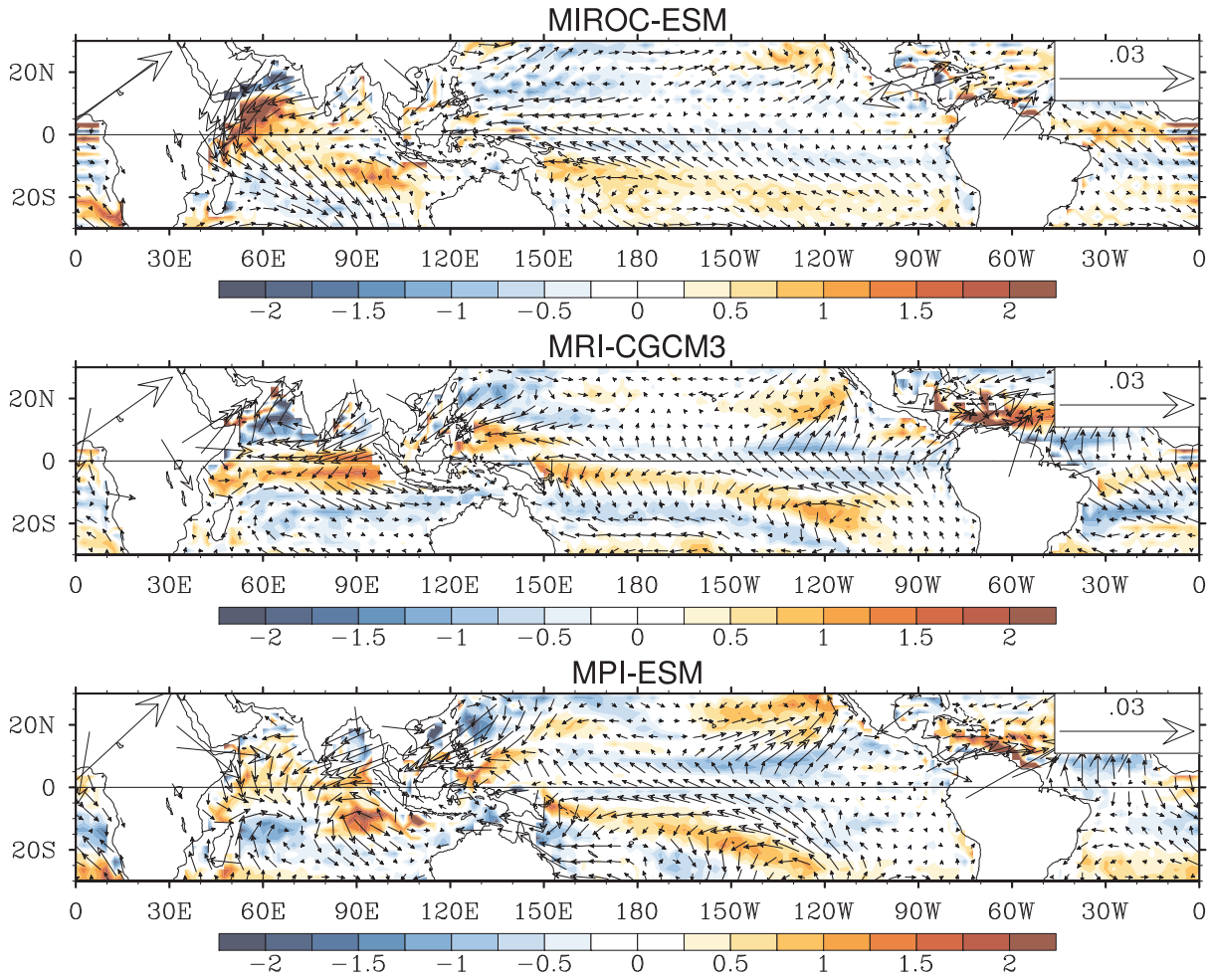

Figure A.5: Fig. A.3 continued.

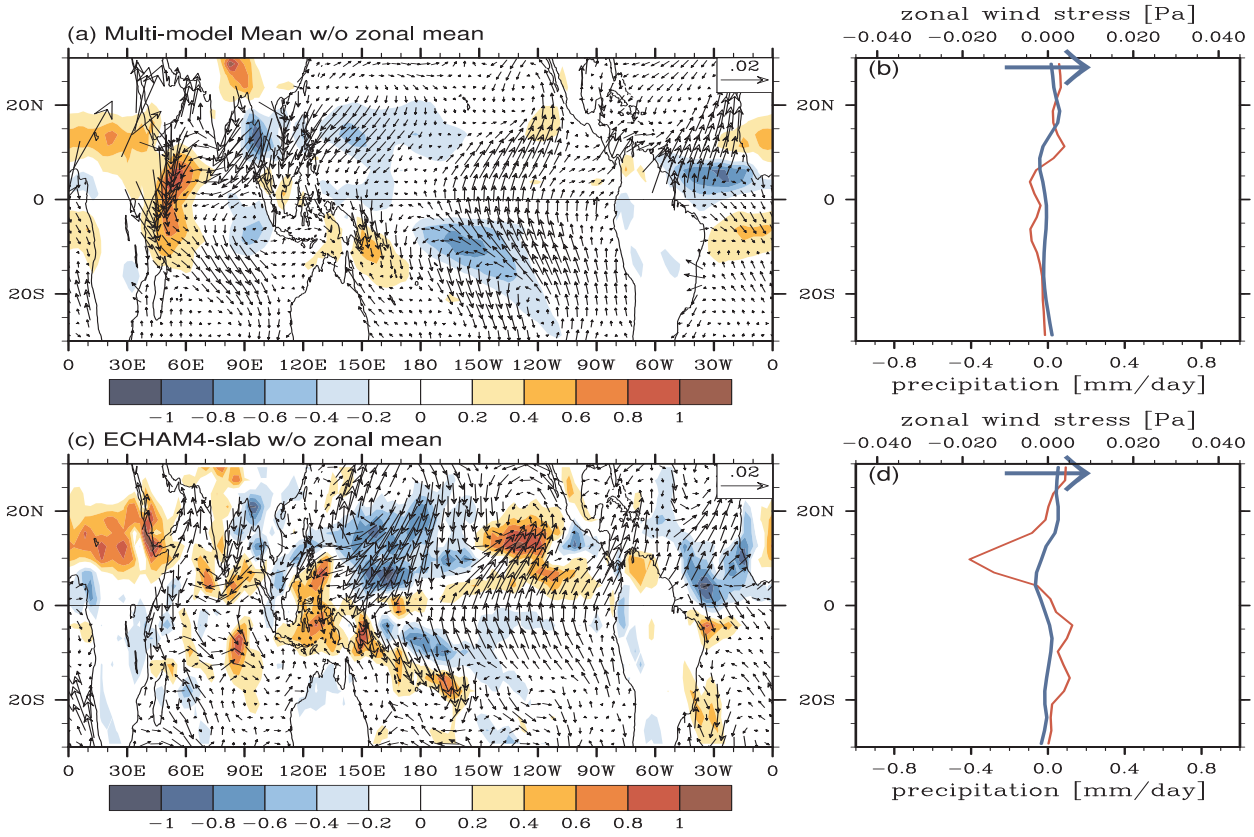

Figure A.6: (a) Change (mid-Holocene minus pre-industrial) in the annual-mean surface wind stress over the oceans (vectors; Pa) and precipitation (shading; mm day^{-1}) after removal of the zonal mean value of each latitude. Shown in (a) is the multi-model mean from the PMIP3 models. Panel (b) shows the zonal mean change in surface zonal wind stress (blue) and in precipitation (red) which, when removed from Figs. 1a and 4c, create the figure shown in panel (a). Panels (c) and (d) are the same as panels (a) and (b), but for the ECHAM4.6-slab ocean model. The arrow in (b) and (d) is the reference wind stress vector used in (a) and (c).

BIBLIOGRAPHY

Anderson, J. L., V. Balaji, A. J. Broccoli, W. F. Cooke, et al., 2004: The new GFDL global atmosphere and land model AM2-LM2: Evaluation with prescribed SST simulations. *Journal of Climate*, **17 (24)**, 4641.

Arbuszewski, J. A., C. Cléroux, L. Bradtmiller, A. Mix, et al., 2013: Meridional shifts of the Atlantic intertropical convergence zone since the Last Glacial Maximum. *Nature Geoscience*, **6 (11)**, 959–962.

Bao, Q., et al., 2013: The flexible global ocean-atmosphere-land system model, spectral version 2: FGOALS-s2. *Advances in Atmospheric Sciences*, **30**, 561–576.

Barnes, E. A. and D. L. Hartmann, 2012: The global distribution of atmospheric eddy length scales. *Journal of Climate*, **25 (9)**, 3409–3416.

Barry, L., G. C. Craig, and J. Thuburn, 2002: Poleward heat transport by the atmospheric heat engine. *Nature*, **415 (6873)**, 774–777.

Bartlein, P., et al., 2011: Pollen-based continental climate reconstructions at 6 and 21 ka: a global synthesis. *Climate Dynamics*, **37 (3-4)**, 775–802.

Battisti, D., Q. Ding, and G. Roe, 2014: Coherent pan-Asian climatic and isotopic response to orbital forcing of tropical insolation. *Journal of Geophysical Research: Atmospheres*, **119 (21)**.

Beerling, D. J. and D. L. Royer, 2011: Convergent cenozoic CO_2 history. *Nature Geoscience*, **4 (7)**, 418.

Bellouin, N., et al., 2011: The HadGEM2 family of Met office unified model climate configurations. *Geoscientific Model Development*, **4 (3)**, 723–757.

Boos, W. R. and R. L. Korty, 2016: Regional energy budget control of the intertropical convergence zone and application to mid-holocene rainfall. *Nature Geoscience*, **9 (12)**, 892.

Boos, W. R. and Z. Kuang, 2010: Dominant control of the South Asian monsoon by orographic insulation versus plateau heating. *Nature*, **463 (7278)**, 218–222.

Bordoni, S. and T. Schneider, 2008: Monsoons as eddy-mediated regime transitions of the tropical overturning circulation. *Nature Geoscience*, **1 (8)**, 515–519, doi:10.1038/ngeo248, URL `http://www.nature.com/doifinder/10.1038/ngeo248`.

Bosmans, J., S. Drijfhout, E. Tuenter, L. Lourens, F. Hilgen, and S. Weber, 2012: Monsoonal response to mid-Holocene orbital forcing in a high resolution GCM. *Climate of the Past*, **8**, 723–740.

Braconnot, P., S. P. Harrison, M. Kageyama, P. J. Bartlein, V. Masson-Delmotte, A. Abe-Ouchi, B. Otto-Bliesner, and Y. Zhao, 2012: Evaluation of climate models using palaeoclimatic data. *Nature Climate Change*, **2 (6)**, 417–424.

Braconnot, P., O. Marti, S. Joussaume, and Y. Leclainche, 2000: Ocean feedback in response to 6 kyr BP insolation. *Journal of Climate*, **13 (9)**, 1537–1553.

Braconnot, P., et al., 2007a: Results of PMIP2 coupled simulations of the Mid-Holocene and Last Glacial Maximum–Part 1: experiments and large-scale features. *Climate of the Past*, **3 (2)**, 261–277.

Braconnot, P., et al., 2007b: Results of PMIP2 coupled simulations of the Mid-Holocene and Last Glacial Maximum–Part 2: feedbacks with emphasis on the location of the ITCZ and mid-and high latitudes heat budget. *Climate of the Past*, **3 (2)**, 279–296.

Carmichael, M. J., et al., 2016: A model–model and data–model comparison for the early Eocene hydrological cycle. *Climate of the Past*, **12 (2)**, 455–481.

Chamales, K. A., 2014: The effects of orbital precession on tropical precipitation. M.S. thesis, University of Miami.

Clement, A., A. Hall, and A. Broccoli, 2004: The importance of precessional signals in the tropical climate. *Climate Dynamics*, **22 (4)**, 327–341.

Collins, J. A., et al., 2011a: Interhemispheric symmetry of the tropical African rainbelt over the past 23,000 years. *Nature Geoscience*, **4 (1)**, 42–45.

Collins, W., et al., 2011b: Development and evaluation of an Earth-system model–HadGEM2. *Geoscientific Model Development*, **4 (4)**, 1051–1075.

Del Genio, A. D. and R. J. Suozzo, 1987: A comparative study of rapidly and slowly rotating dynamical regimes in a terrestrial general circulation model. *Journal of the Atmospheric Sciences*, **44 (6)**, 973–986.

Dima, I. M. and J. M. Wallace, 2003: On the seasonality of the Hadley cell. *Journal of the atmospheric sciences*, **60 (12)**, 1522–1527.

Donohoe, A. and D. S. Battisti, 2012: What determines meridional heat transport in climate models? *Journal of Climate*, **25 (11)**, 3832–3850.

Donohoe, A., J. Marshall, D. Ferreira, and D. Mcgee, 2013: The relationship between ITCZ location and cross-equatorial atmospheric heat transport: From the seasonal cycle to the Last Glacial Maximum. *Journal of Climate*, **26 (11)**, 3597–3618.

Fasullo, J. T. and K. E. Trenberth, 2008: The annual cycle of the energy budget. Part II: Meridional structures and poleward transports. *Journal of Climate*, **21 (10)**, 2313–2325.

Flannery, B. P., 1984: Energy balance models incorporating transport of thermal and latent energy. *Journal of the Atmospheric Sciences*, **41 (3)**, 414–421.

Frierson, D. M., I. M. Held, and P. Zurita-Gotor, 2006: A gray-radiation aquaplanet moist GCM. Part I: Static stability and eddy scale. *Journal of the atmospheric sciences*, **63 (10)**, 2548–2566.

Frierson, D. M., I. M. Held, and P. Zurita-Gotor, 2007: A gray-radiation aquaplanet moist GCM. Part II: Energy transports in altered climates. *Journal of the atmospheric sciences*, **64 (5)**, 1680–1693.

Frierson, D. M. and Y.-T. Hwang, 2012: Extratropical influence on ITCZ shifts in slab ocean simulations of global warming. *Journal of Climate*, **25 (2)**, 720–733.

Frierson, D. M., et al., 2013: Contribution of ocean overturning circulation to tropical rainfall peak in the Northern Hemisphere. *Nature Geoscience*, **6 (11)**, 940–944.

Garreaud, R. and J. M. Wallace, 1998: Summertime incursions of midlatitude air into subtropical and tropical South America. *Monthly Weather Review*, **126 (10)**, 2713–2733.

Garreaud, R. D., M. Vuille, R. Compagnucci, and J. Marengo, 2009: Present-day South American climate. *Palaeogeography, Palaeoclimatology, Palaeoecology*, **281 (3)**, 180–195.

Geisler, J. E., E. J. Pitcher, and R. C. Malone, 1983: Rotating-fluid experiments with an atmospheric general circulation model. *Journal of Geophysical Research: Oceans*, **88 (C14)**, 9706–9716.

Gent, P. R., et al., 2011: The community climate system model version 4. *Journal of Climate*, **24 (19)**, 4973–4991.

Haffer, J., 1969: Speciation in Amazonian forest birds. *Science*, **165 (3889)**, 131–137.

Hall, M. M. and H. L. Bryden, 1982: Direct estimates and mechanisms of ocean heat transport. *Deep Sea Research Part A. Oceanographic Research Papers*, **29 (3)**, 339–359.

Hartmann, D. L., 2015: Pacific sea surface temperature and the winter of 2014. *Geophysical Research Letters*, **42 (6)**, 1894–1902.

Haug, G. H., K. A. Hughen, D. M. Sigman, L. C. Peterson, and U. Röhl, 2001: Southward migration of the intertropical convergence zone through the Holocene. *Science*, **293 (5533)**, 1304–1308.

Heinemann, M., J. Jungclaus, and J. Marotzke, 2009: Warm Paleocene/Eocene climate as simulated in ECHAM5/MPI-OM. *Climate of the Past*, **5**, 785–802.

Held, I. M., 2000: The general circulation of the atmosphere. URL `http://www.whoi.edu/page.do?pid=13076`, Paper presented at 2000 Woods Hole Oceanographic Institute Geophysical Fluid Dynamics Program, Woods Hole Oceanographic Institute, Woods Hole, MA.

Held, I. M. and A. Y. Hou, 1980: Nonlinear axially symmetric circulations in a nearly inviscid atmosphere. *Journal of the Atmospheric Sciences*, **37 (3)**, 515–533.

Hess, P. G., D. S. Battisti, and P. J. Rasch, 1993: Maintenance of the intertropical convergence zones and the large-scale tropical circulation on a water-covered earth. *Journal of the atmospheric sciences*, **50 (5)**, 691–713.

Hollis, C. J., et al., 2012: Early Paleogene temperature history of the Southwest Pacific Ocean: Reconciling proxies and models. *Earth and Planetary Science Letters*, **349**, 53–66.

Hsu, Y.-H., C. Chou, and K.-Y. Wei, 2010: Land-ocean asymmetry of tropical precipitation changes in the mid-Holocene. *Journal of Climate*, **23 (15)**, 4133–4151.

Huber, M., H. Brinkhuis, C. E. Stickley, K. Döös, A. Sluijs, J. Warnaar, S. A. Schellenberg, and G. L. Williams, 2004: Eocene circulation of the Southern Ocean: Was Antarctica kept warm by subtropical waters? *Paleoceanography*, **19 (4)**.

Huber, M. and R. Caballero, 2011: The early Eocene equable climate problem revisited. *Climate of the Past*, **7 (2)**, 603.

Huber, M. and L. C. Sloan, 2001: Heat transport, deep waters, and thermal gradients: Coupled simulation of an Eocene greenhouse climate. *Geophysical Research Letters*, **28 (18)**, 3481–3484.

Hwang, Y.-T. and D. M. Frierson, 2010: Increasing atmospheric poleward energy transport with global warming. *Geophysical Research Letters*, **37 (24)**.

Jansen, M. and R. Ferrari, 2015: Diagnosing the vertical structure of the eddy diffusivity in real and idealized atmospheres. *Quarterly Journal of the Royal Meteorological Society*, **141 (687)**, 631–641.

Jaramillo, C., M. J. Rueda, and G. Mora, 2006: Cenozoic plant diversity in the Neotropics. *Science*, **311 (5769)**, 1893–1896.

Jenkins, G., H. G. Marshall, W. Kuhn, et al., 1993: Precambrian climate: The effects of land area and Earth's rotation rate. *Journal of Geophysical Research: Atmospheres*, **98 (D5)**, 8785–8791.

Jenkins, G. S., 1996: A sensitivity study of changes in Earth's rotation rate with an atmospheric general circulation model. *Global and Planetary Change*, **11 (4)**, 141–154.

Jolly, D., S. Harrison, B. Damnati, and R. Bonnefille, 1998: Simulated climate and biomes of Africa during the Late Quaternary: Comparison with pollen and lake status data. *Quaternary Science Reviews*, **17 (6)**, 629–657.

Jones, C., et al., 2011: The HadGEM2-ES implementation of CMIP5 centennial simulations. *Geoscientific Model Development*, **4 (3)**, 543–570.

Joussaume, S., et al., 1999: Monsoon changes for 6000 years ago: results of 18 simulations from the Paleoclimate Modeling Intercomparison Project (PMIP). *Geophysical Research Letters*, **26 (7)**, 859–862.

Kodama, Y.-M., 1993: Large-scale common features of subtropical convergence zones (the Baiu frontal zone, the SPCZ and the SACZ) Part II: Conditions of the circulations for generating the STCZs. *J. Meteor. Soc. Japan*, **71**, 581–610.

Kutzbach, J. E. and P. J. Guetter, 1986: The influence of changing orbital parameters and surface boundary conditions on climate simulations for the past 18 000 years. *Journal of the Atmospheric Sciences*, **43 (16)**, 1726–1759.

Lapeyre, G. and I. Held, 2003: Diffusivity, kinetic energy dissipation, and closure theories for the poleward eddy heat flux. *Journal of the atmospheric sciences*, **60 (23)**, 2907–2916.

LeGrande, A. N. and G. A. Schmidt, 2009: Sources of Holocene variability of oxygen isotopes in paleoclimate archives. *Climate of the Past*, **5 (3)**, 441–455, doi:10.5194/cp-5-441-2009, URL `http://www.clim-past.net/5/441/2009/`.

Lenters, J. D. and K. Cook, 1995: Simulation and diagnosis of the regional summertime precipitation climatology of South America. *Journal of Climate*, **8 (12)**, 2988–3005.

Li, L., et al., 2013: The flexible global ocean-atmosphere-land system model, Grid-point Version 2: FGOALS-g2. *Advances in Atmospheric Sciences*, **30**, 543–560.

Liu, X. and D. S. Battisti, 2015: The Influence of orbital forcing of tropical insolation on the climate and isotopic composition of precipitation in South America. *Journal of Climate*, **28 (2015)**, 4841–4862.

Liu, X., D. S. Battisti, and A. Donohoe, 2017a: Tropical precipitation and cross-equatorial ocean heat transport during the Mid-Holocene. *Journal of Climate*, **30 (10)**, 3529–3547.

Liu, X., D. S. Battisti, and G. H. Roe, 2017b: The effect of cloud cover on the meridional heat transport: lessons from variable rotation experiments. *Journal of Climate*, **30 (18)**, 7465–7479.

Lucarini, V. and F. Ragone, 2011: Energetics of climate models: Net energy balance and meridional enthalpy transport. *Reviews of Geophysics*, **49 (1)**.

Lunt, D. J., P. J. Valdes, T. D. Jones, A. Ridgwell, A. M. Haywood, D. N. Schmidt, R. Marsh, and M. Maslin, 2010: CO_2-driven ocean circulation changes as an amplifier of Paleocene-Eocene thermal maximum hydrate destabilization. *Geology*, **38 (10)**, 875–878.

Magnusdottir, G. and R. Saravanan, 1999: The response of atmospheric heat transport to zonally averaged SST trends. *Tellus A*, **51 (5)**, 815–832.

Manabe, S. and K. Bryan, 1985: CO_2-induced change in a coupled ocean-atmosphere model and its paleoclimatic implications. *Journal of Geophysical Research: Oceans*, **90 (C6)**, 11 689–11 707.

Mantsis, D. F., A. C. Clement, A. J. Broccoli, and M. P. Erb, 2011: Climate feedbacks in response to changes in obliquity. *Journal of Climate*, **24 (11)**, 2830–2845.

Marsland, S. J., H. Haak, J. H. Jungclaus, M. Latif, and F. Röske, 2003: The Max-Planck-Institute global ocean/sea ice model with orthogonal curvilinear coordinates. *Ocean modelling*, **5 (2)**, 91–127.

McGee, D., A. Donohoe, J. Marshall, and D. Ferreira, 2014: Changes in ITCZ location and cross-equatorial heat transport at the Last Glacial Maximum, Heinrich Stadial 1, and the mid-Holocene. *Earth and Planetary Science Letters*, **390**, 69–79.

Navarra, A. and G. Boccaletti, 2002: Numerical general circulation experiments of sensitivity to Earth rotation rate. *Climate Dynamics*, **19 (5-6)**, 467–483.

Nogués-Paegle, J. and K. C. Mo, 1997: Alternating wet and dry conditions over South America during summer. *Monthly Weather Review*, **125 (2)**, 279–291.

Paillard, D., 2010: Climate and the orbital parameters of the Earth. *Comptes Rendus Geoscience*, **342 (4)**, 273–285.

Phipps, S., L. Rotstayn, H. Gordon, J. Roberts, A. Hirst, and W. Budd, 2011: The CSIRO Mk3L climate system model version 1.0–Part 1: Description and evaluation. *Geoscientific Model Development*, **4 (2)**, 483–509.

Prado, L. F., I. Wainer, and C. M. Chiessi, 2013: Mid-Holocene PMIP3/CMIP5 model results: Intercomparison for the South American monsoon system. *The Holocene*, **23 (12)**, 1915–1920.

Prive, N. C. and R. A. Plumb, 2007a: Monsoon dynamics with interactive forcing. Part I: Axisymmetric studies. *Journal of Atmospheric Sciences*, **64 (5)**, 1417–1430, doi:{10.1175/JAS3916.1}.

Prive, N. C. and R. A. Plumb, 2007b: Monsoon dynamics with interactive forcing. Part II: Impact of eddies and asymmetric geometries. *Journal of Atmospheric Sciences*, **64 (5)**, 1431–1442, doi:{10.1175/JAS3917.1}.

Raddatz, T., et al., 2007: Will the tropical land biosphere dominate the climate–carbon cycle feedback during the twenty-first century? *Climate Dynamics*, **29 (6)**, 565–574.

Roe, G. H., N. Feldl, K. C. Armour, Y.-T. Hwang, and D. M. Frierson, 2015: The remote impacts of climate feedbacks on regional climate predictability. *Nature Geoscience*, **8 (2)**, 135–139.

Roeckner, E., 1996: Coauthors, 1996: The atmospheric general circulation model ECHAM-4: Model description and simulation of present-day climate. *Max-Planck-Institut für Meteorologie Rep*, **218**, 90.

Rose, B. E., K. C. Armour, D. S. Battisti, N. Feldl, and D. D. Koll, 2014: The dependence of transient climate sensitivity and radiative feedbacks on the spatial pattern of ocean heat uptake. *Geophysical Research Letters*, **41 (3)**, 1071–1078.

Rose, B. E. and D. Ferreira, 2012: Ocean heat transport and water vapor greenhouse in a warm equable climate: A new look at the low gradient paradox. *Journal of Climate*, **26 (6)**, 2117–2136.

Rotstayn, L. D., 1997: A physically based scheme for the treatment of stratiform clouds and precipitation in large-scale models. I: Description and evaluation of the microphysical processes. *Quarterly Journal of the Royal Meteorological Society*, **123 (541)**, 1227–1282.

Rotstayn, L. D., M. A. Collier, M. R. Dix, Y. Feng, H. B. Gordon, S. P. O'Farrell, I. N. Smith, and J. Syktus, 2010: Improved simulation of Australian climate and ENSO-related rainfall variability in a global climate model with an interactive aerosol treatment. *International Journal of Climatology*, **30 (7)**, 1067–1088.

Salameh, J., M. Popp, and J. Marotzke, 2017: The role of sea-ice albedo in the climate of slowly rotating aquaplanets. *Climate Dynamics*, 1–16.

Schmidt, G. A., et al., 2006: Present-day atmospheric simulations using GISS ModelE: Comparison to in situ, satellite, and reanalysis data. *Journal of Climate*, **19 (2)**, 153–192.

Schneider, E. K., 1984: Response of the annual and zonal mean winds and temperatures to variations in the heat and momentum sources. *Journal of the Atmospheric Sciences*, **41 (7)**, 1093–1115.

Schneider, T., T. Bischoff, and G. H. Haug, 2014: Migrations and dynamics of the intertropical convergence zone. *Nature*, **513 (7516)**, 45–53, doi:10.1038/nature13636, URL `http://www.nature.com/doifinder/10.1038/nature13636`.

Seager, R., N. Naik, and G. A. Vecchi, 2010: Thermodynamic and dynamic mechanisms for large-scale changes in the hydrological cycle in response to global warming. *Journal of Climate*, **23 (17)**, 4651–4668.

Seton, M., et al., 2012: Global continental and ocean basin reconstructions since 200Ma. *Earth-Science Reviews*, **113 (3)**, 212–270.

Sijp, W. P. and M. H. England, 2004: Effect of the Drake Passage throughflow on global climate. *Journal of Physical Oceanography*, **34 (5)**, 1254–1266.

Stocker, T., 2014: *Climate change 2013: the physical science basis: Working Group I contribution to the Fifth assessment report of the Intergovernmental Panel on Climate Change*. Cambridge University Press.

Stone, P. H., 1978: Constraints on dynamical transports of energy on a spherical planet. *Dynamics of Atmospheres and Oceans*, **2 (2)**, 123–139.

Street, F. A. and A. Grove, 1976: Environmental and climatic implications of late Quaternary lake-level fluctuations in Africa. *Nature*, **261**, 385–390.

Taylor, K. E., R. J. Stouffer, and G. A. Meehl, 2012: An overview of CMIP5 and the experiment design. *Bulletin of the American Meteorological Society*, **93 (4)**, 485–498.

Tiedtke, M., 1993: Representation of clouds in large-scale models. *Monthly Weather Review*, **121 (11)**, 3040–3061.

Toggweiler, J. and H. Bjornsson, 2000: Drake Passage and palaeoclimate. *Journal of Quaternary Science*, **15 (4)**, 319–328.

Toggweiler, J. and B. Samuels, 1995: Effect of Drake Passage on the global thermohaline circulation. *Deep Sea Research Part I: Oceanographic Research Papers*, **42 (4)**, 477–500.

Trenberth, K. E. and J. M. Caron, 2001: Estimates of meridional atmosphere and ocean heat transports. *Journal of Climate*, **14 (16)**, 3433–3443.

Trenberth, K. E., J. T. Fasullo, and J. Kiehl, 2009: Earth's global energy budget. *Bulletin of the American Meteorological Society*, **90 (3)**, 311–323.

Vallis, G. K., 2006: *Atmospheric and oceanic fluid dynamics: fundamentals and large-scale circulation*. Cambridge University Press.

Vallis, G. K. and R. Farneti, 2009: Meridional energy transport in the coupled atmosphere–ocean system: scaling and numerical experiments. *Quarterly Journal of the Royal Meteorological Society*, **135 (644)**, 1643–1660.

Vera, C., et al., 2006: Toward a unified view of the American monsoon systems. *Journal of Climate*, **19 (20)**, 4977–5000.

Vimont, D. J., D. S. Battisti, and R. L. Naylor, 2010: Downscaling Indonesian precipitation using large-scale meteorological fields. *International Journal of Climatology*, **30 (11)**, 1706–1722, doi:10.1002/joc.2010, URL `http://dx.doi.org/10.1002/joc.2010`.

Voldoire, A., et al., 2013: The CNRM-CM5. 1 global climate model: description and basic evaluation. *Climate Dynamics*, **40 (9-10)**, 2091–2121.

Walker, C. C. and T. Schneider, 2006: Eddy influences on Hadley circulations: Simulations with an idealized GCM. *Journal of the Atmospheric Sciences*, **63 (12)**, 3333–3350.

Watanabe, S., et al., 2011: MIROC-ESM: model description and basic results of CMIP5-20c3m experiments. *Geosci Model Dev Discuss*, **4 (2)**, 1063–1128.

Wilf, P., K. R. Johnson, N. R. Cúneo, M. E. Smith, B. S. Singer, and M. A. Gandolfo, 2005: Eocene plant diversity at Laguna del Hunco and Río Pichileufú, Patagonia, Argentina. *The American Naturalist*, **165 (6)**, 634–650.

Williams, G. P., 1988: The dynamical range of global circulations II. *Climate Dynamics*, **3 (2)**, 45–84.

Williams, G. P. and J. Holloway, 1982: The range and unity of planetary circulations. *Nature*, **297 (5864)**, 295–299.

Winguth, A., C. Shellito, C. Shields, and C. Winguth, 2010: Climate response at the Paleocene–Eocene thermal maximum to greenhouse gas forcing—a model study with CCSM3. *Journal of Climate*, **23 (10)**, 2562–2584.

Xin, X., W. Tong-Wen, and Z. Jie, 2013: Introduction of CMIP5 experiments carried out with the climate system models of Beijing Climate Center. *Advances in Climate Change Research*, **4 (1)**, 41–49.

Yang, J., G. Boué, D. C. Fabrycky, and D. S. Abbot, 2014: Strong dependence of the inner edge of the habitable zone on planetary rotation rate. *The Astrophysical Journal Letters*, **787 (1)**, L2.

Yukimoto, S., et al., 2012: A New Global Climate Model of the Meteorological Research Institute: MRI-CGCM3: Model Description and Basic Performance. *Journal of the Meteorological Society of Japan*, **90**, 23–64.

Zachos, J., M. Pagani, L. Sloan, E. Thomas, and K. Billups, 2001: Trends, Rhythms, and Aberrations in Global Climate 65 Ma to Present. *Science*, **292 (5517)**, 686, URL `http://science.sciencemag.org/content/292/5517/686.abstract`.

Zhou, J. and K. Lau, 1998: Does a monsoon climate exist over South America? *Journal of Climate*, **11 (5)**, 1020–1040.